Patient-based color Doppler echocardiographic simulation

Yunyun Sun

N°d'ordre NNT : 2022LYSEI003

THESE de DOCTORAT DE L'UNIVERSITE DE LYON
opérée au sein de
L'INSA de Lyon

Ecole Doctorale N° 160
Electronique, Electrotechnique, Automatique (EEA)

Spécialité de doctorat :
Traitement du Signal et de l'Image

Soutenue publiquement le 24/01/2022, par:
Yunyun SUN

Patient-based color Doppler echocardiographic simulation

Simulation d'images échocardiographiques Doppler couleur à partir de patients

---

Devant le jury composé de :

Bernard, Olivier	Professeur	INSA de Lyon	Directeur de thèse
Bosch.G, Johan	Associated Professor	Erasmus University	Rapporteur
Franceschini, Emilie	Chargé de Recherche	CNRS	Rapporteure
Friboulet, Denis	Professeur	INSA de Lyon	Examinateur
Garcia, Damien	Chargé de Recherche	INSERM	Co-Directeur de thèse
Thiran, Jean-Philippe	Professeur	EPFL	Examinateur

Département FEDORA – INSA Lyon - Ecoles Doctorales

SIGLE	ECOLE DOCTORALE	NOM ET COORDONNEES DU RESPONSABLE
CHIMIE	**CHIMIE DE LYON** **https://www.edchimie-lyon.fr** Sec. : Renée EL MELHEM Bât. Blaise PASCAL, 3e étage secretariat@edchimie-lyon.fr	**M. Stéphane DANIELE** C2P2-CPE LYON-UMR 5265 Bâtiment F308, BP 2077 43 Boulevard du 11 novembre 1918 69616 Villeurbanne **directeur@edchimie-lyon.fr**
E.E.A.	**ÉLECTRONIQUE, ÉLECTROTECHNIQUE, AUTOMATIQUE** **https://edeea.universite-lyon.fr** Sec. : Stéphanie CAUVIN Bâtiment Direction INSA Lyon Tél : 04.72.43.71.70 secretariat.edeea@insa-lyon.fr	**M. Philippe DELACHARTRE** INSA LYON Laboratoire CREATIS Bâtiment Blaise Pascal, 7 avenue Jean Capelle 69621 Villeurbanne CEDEX Tél : 04.72.43.88.63 **philippe.delachartre@insa-lyon.fr**
E2M2	**ÉVOLUTION, ÉCOSYSTÈME, MICROBIOLOGIE, MODÉLISATION** **http://e2m2.universite-lyon.fr** Sec. : Sylvie ROBERJOT Bât. Atrium, UCB Lyon 1 Tél : 04.72.44.83.62 secretariat.e2m2@univ-lyon1.fr	**M. Philippe NORMAND** Université Claude Bernard Lyon 1 UMR 5557 Lab. d'Ecologie Microbienne Bâtiment Mendel 43, boulevard du 11 Novembre 1918 69 622 Villeurbanne CEDEX **philippe.normand@univ-lyon1.fr**
EDISS	**INTERDISCIPLINAIRE SCIENCES-SANTÉ** **http://ediss.universite-lyon.fr** Sec. : Sylvie ROBERJOT Bât. Atrium, UCB Lyon 1 Tél : 04.72.44.83.62 secretariat.ediss@univ-lyon1.fr	**Mme Sylvie RICARD-BLUM** Institut de Chimie et Biochimie Moléculaires et Supramoléculaires (ICBMS) - UMR 5246 CNRS - Université Lyon 1 Bâtiment Raulin - 2ème étage Nord 43 Boulevard du 11 novembre 1918 69622 Villeurbanne Cedex Tél : +33(0)4 72 44 82 32 **sylvie.ricard-blum@univ-lyon1.fr**
INFOMATHS	**INFORMATIQUE ET MATHÉMATIQUES** **http://edinfomaths.universite-lyon.fr** Sec. : Renée EL MELHEM Bât. Blaise PASCAL, 3e étage Tél : 04.72.43.80.46 infomaths@univ-lyon1.fr	**M. Hamamache KHEDDOUCI** Université Claude Bernard Lyon 1 Bât. Nautibus 43, Boulevard du 11 novembre 1918 69 622 Villeurbanne Cedex France Tél : 04.72.44.83.69 **hamamache.kheddouci@univ-lyon1.fr**
Matériaux	**MATÉRIAUX DE LYON** **http://ed34.universite-lyon.fr** Sec. : Yann DE ORDENANA Tél : 04.72.18.62.44 yann.de-ordenana@ec-lyon.fr	**M. Stéphane BENAYOUN** Ecole Centrale de Lyon Laboratoire LTDS 36 avenue Guy de Collongue 69134 Ecully CEDEX Tél : 04.72.18.64.37 **stephane.benayoun@ec-lyon.fr**
MEGA	**MÉCANIQUE, ÉNERGÉTIQUE, GÉNIE CIVIL, ACOUSTIQUE** **http://edmega.universite-lyon.fr** Sec. : Stéphanie CAUVIN Tél : 04.72.43.71.70 Bâtiment Direction INSA Lyon mega@insa-lyon.fr	**M. Jocelyn BONJOUR** INSA Lyon Laboratoire CETHIL Bâtiment Sadi-Carnot 9, rue de la Physique 69621 Villeurbanne CEDEX **jocelyn.bonjour@insa-lyon.fr**
ScSo	**ScSo*** **https://edsciencessociales.universite-lyon.fr** Sec. : Mélina FAVETON INSA : J.Y. TOUSSAINT Tél : 04.78.69.77.79 melina.faveton@univ-lyon2.fr	**M. Christian MONTES** Université Lumière Lyon 2 86 Rue Pasteur 69365 Lyon CEDEX 07 **christian.montes@univ-lyon2.fr**

*ScSo : Histoire, Géographie, Aménagement, Urbanisme, Archéologie, Science politique, Sociologie, Anthropologie

"History repeats, but science reverberates."

Siddhartha Mukherjee

Patient-based color Doppler echocardiographic simulation

Université de Lyon
Ecole EEA de Lyon: thématique Traitement du signal et de limage

Yunyun SUN

Abstract

Cardiovascular diseases are one of the major causes of death in the world. The investigation of cardiac pathologies with the help of medical imaging plays a crucial part. In this context, intraventricular blood flow is an important source of information for cardiac diagnoses. In particular, color Doppler imaging is a modality of choice for simultaneous visualization of myocardium and blood flow over a wide scan area. However, this visualization modality is subject to several sources of error, the main ones being aliasing and clutter. Mitigation of these artifacts is an important concern for better analysis of intracardiac flow.

In order to solve this issue, deep learning is a promising avenue that has been explored increasingly by the ultrasound community. This data-driven technique requires large databases with artifact-free ground-truths. This thesis presents a numerical framework for the generation of large scale clinical-like color Doppler sequences. Synthetic blood vector fields were computed from a computational fluid dynamics model and an intraventricular flow estimation technique. Realistic texture and clutter artifacts were simulated from real clinical ultrasound cine loops. We have simulated several scenarios highlighting the effects of *i)* flow acceleration, *ii)* wall clutter, *iii)* transmit wavefronts on Doppler velocities.

A first synthetic dataset composed of 20 virtual patients is publicly available and can be used to evaluate the quality of Doppler estimation techniques. Besides, the framework I developed during my thesis can be seen as a first step towards the generation of comprehensive datasets for training neural networks to improve the quality of Doppler imaging.

Acknowledgements

Contents

List of Figures

List of Tables

List of Abbreviations

PRF Pulse Repetition Frequency. 28

ALE Arbitrary Lagrangian-Eulerian. 51

CDI Color Doppler Imaging. 2, 46

CFD Computational Fluid Dynamics. 38, 47

CMRI Cardiac Magnetic Res-onance Imaging. 9

CWD Continuous-wave Doppler. 46

DL Deep Learning. 2, 46

DW Diverging Wave. 19, 23

E/M electromechanical. 47

ECG electrocardiogram. 7

ED End of Diastole. 48

EVD Eigen Value Decomposition. 31

FIR Finite Impulse Filter. 29

FW Focused Wave. 19

IIR Infinite Impulse Filter. 29

IQ In-phase and Quadrature. 24

iVFM Intraventricular Vector Flow Mapping. 38

LV Left Ventricle. 20

MLT Multi-Line Transmission. 20

MUST Matlab ultrasound toolbox. 52

PSF Point Spread Function. 22

PWD Pulsed-wave Doppler. 46

RF Radio Frequency. 23

SA Synthetic Aperture. 20

SNR Signal to Noise Ratio. 20, 23

SVD Singular Value Decomposition. 31

Chapter 1

Introduction

Contents

This chapter first presents the context around this thesis and then introduces the proposed methodology. A concise outline of the thesis organization will end this chapter.

1.1 Context

1.1.1 Clinical context

Cardiovascular diseases are the leading cause of death in the world, accounting for approximately 17.9 million deaths per year, or 32% of all deaths [7]. Intermediate risks factors can be measured in primary care facilities and indicate an increased risk of heart attack, heart failure and other complications. To this end, various researches have been carried out with different emphases. Among them, blood flow estimation and analysis are an important topic, considering it contains rich information to establish a diagnosis. In particular, the intraventricular flow might be an indicator for evaluating the filling function of patients with heart failure.

In this context, in order to image and analyze the blood flow in the entire cardiac cavities, Color Doppler Imaging (CDI) is the modality of choice in clinical routine. It provides general visualization of intraventricular flow but without accurate quantitative measurement. Although other Doppler techniques (*i.e.*, continuous and pulsed Doppler [8]) allow quantitative velocity measurements, these methods rely on the estimation of a 1D projection of the actual velocity along the ultrasound lines, limiting their applications.

1.1.2 Algorithmic context

Several methods have been proposed to estimate 2D or 3D intraventricular flow motion using ultrasound acquisitions [5,9–12]. All of these methods need expert interaction (e.g., segmentation of cardiac cavities) or expert correction (e.g., aliasing removal, clutter filtering), limiting their applicability in clinical routines.

Deep Learning (DL) methods have revolutionized several applications in ultrasound imaging that have been under investigation for several decades, the main ones relating to classification (*e.g.*, automatic view recognition [13]) and segmentation (*e.g.*, automatic extraction of clinical indices [14]). Mainly, supervised methods produce the most satisfying results. These methods rely on a large-scale annotated dataset. Moreover, it is interesting to note that very few DL studies investigate to improve intraventricular blood flow estimation. One of the main reasons is probably the difficulty in accessing referenced datasets, *i.e.*, data whose intraventricular flows are known and can serve as reference for DL algorithms. In this context, realistic ultrasound simulation pipelines can play a crucial role. Indeed, such tools would allow the generation of large-scale benchmarked datasets and thus will enable the investigation of the potential of DL to solve this problem. One of the current difficulties of conventional methods concerns the presence of complex artifacts, such as aliasing and clutter noise. The capacity of the simulation pipeline to reproduce those artifacts will thus be the key to make DL solutions robust with these sources of noise.

1.2 Challenges

To be able to apply DL techniques to estimate blood flow in the whole cavity accurately, this thesis addresses the following three challenges:

1. The first challenge concerns the development of a simulation pipeline to generate an adequate referenced synthetic dataset. This simulated dataset must be realistic, close to clinical data, and containing validated reference flow. The generated dataset will be publicly accessible to be thoroughly validated and beneficial to the community.

2. The ultrasound simulations need to contain the typical artifacts like clutter noise and aliasing, to make the simulations even more realistic and propitious for DL. The second challenge of my thesis will then be the capacity to synthesize such artifacts.

3. The desired database is supposed to achieve variety and diversity in the patient anatomy and intraventricular flow dynamic. The third challenge will be the personalization of the pipeline to obtain adequate large-scale simulation.

1.3 Methodology

This thesis focuses on generating realistic synthetic ultrasound duplex sequences, which allows the simultaneous visualization of anatomical (B-mode) and functional (color Doppler) images. Such a dataset will be used soon in my team to feed DL solutions, but this is not the scope of this thesis work. I developed a novel simulation pipeline to construct this referenced database that combines state-of-the-art solutions for generating numeric intraventricular flow with an ultrasound physical simulator. The flow model determines the reference value of the blood flow in our simulation. In conjunction with scatterer strategies, the ultrasound simulator generates realistic ultrasound images with Doppler information. Because of the use of a physical simulator, we show that our pipeline intrinsically generates typical artifacts, *i.e.*, aliasing and clutter from tissue motion.

1.4 Thesis organization

The organization of the manuscript is as follows:

1. Presentation

    - Introduction: This chapter presents the context, methodological strategy, and detail of the organization of the manuscript.

2. Background

    - Chapter 2: This chapter presents a dedicated description of the context of this thesis. In particular, I will develop the following aspects: the heart physiology, the popular modalities used in clinical practice, and the physical principles of ultrasound.

- Chapter 3: This chapter presents a review of the state-of-the-art methods for ultrasound simulations and intraventricular flow estimation.

3. Contributions

   - Chapter 4: This chapter provides a detailed description of the pipeline I developed to generate realistic echocardiographic Doppler sequences.
   - Chapter 5: This chapter presents an extension of the pipeline to facilitate the simulation of Color Doppler images for large-scale datasets.

4. Conclusion

   - Chapter 6: This chapter provides the conclusion of this thesis. In particular, the key achievements and perspectives of this thesis work are presented.

5. Thesis summary

- Thesis summary in French, as requested by the doctoral school EEA, which covers every discussion of the manuscript, focusing on key points;

1.5 Related publications

Here is a list of the different publications related to my PhD work:

- International conferences
  - Y. Sun, K. Faraz, T. Grenier, P. Clarysse, D. Garcia, O. Bernard, "A duplex pipeline for the generation of realistic echocardiographic sequences with doppler imaging", in *IEEE IUS conference*, 2020.
  - Y. Sun, D. Garcia, O. Bernard, "An acoustic model for the simulation of patient-specific echocardiographic images", in *VPH2020 conference*, 2020.
- International journals
  - Y. Sun, F. Vixège, K. Faraz, S. Mendez, F. Nicoud, D. Garcia, and O. Bernard, "A pipeline for the generation of realistic synthetic echocardiographic duplex sequences", *IEEE Transacions on Ultrasonics, Ferroelectrics, and Frequency*, under 2nd review.
  - E. Evain, Y. Sun, K. Faraz, D. Garcia, E. Saloux, M. De Craene, O. Bernard, "Motion estimation by deep learning in 2D echocardiography: synthetic dataset and validation", *IEEE Transacions on Medical Imaging*, under 2nd review.
  - F. Vixège, A. Berod, Y. Sun, S. Mendez, O. Bernard, N. Ducros, P.Y. Courand, F. Nicoud, and D. Garcia, "Physics-constrained intraventricular vector flow mapping by color Doppler", *Physics in Medicine & Biology*, under 2nd review.

Chapter 2

Background

Contents

2.1 Clinical background

This chapter introduces the clinical context and briefly describes the different use of ultrasound modalities to assess heart function and anatomy in clinical practice.

2.1.1 Cardiac physiology

In this section, I will develop the basics of cardiac anatomy and functioning to allow an easy understanding of the intraventricular blood flow.

2.1.1.1 Cardiac anatomy

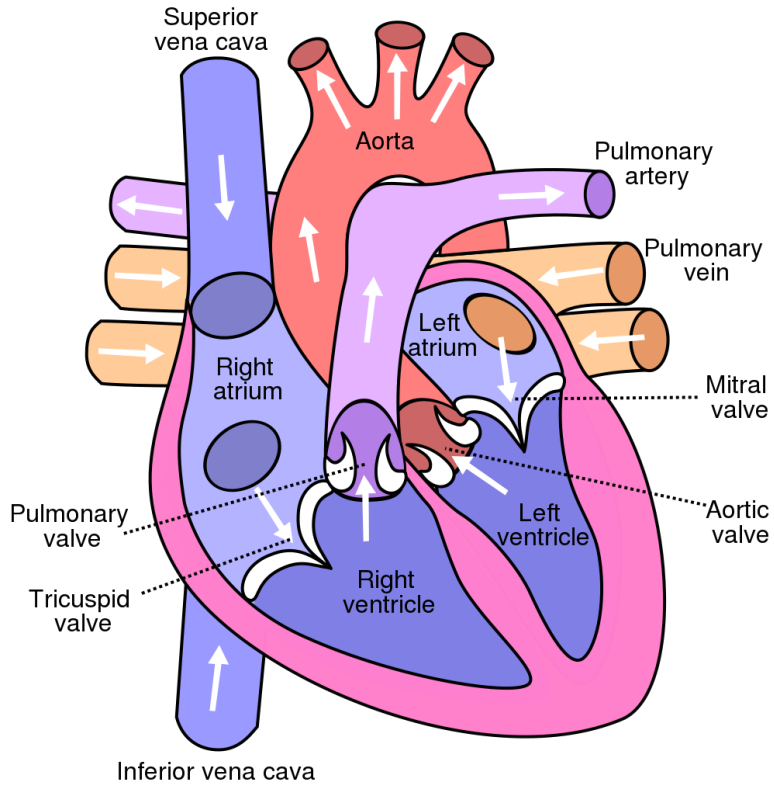

Figure 2.1: Illustration of the anatomical cardiac structures. This figure is reprinted from [1].

In order for blood to circulate all over the human body, the heart repetitively undergoes the phases of contraction and relaxation, which, in turn, transport oxygen and essential nutrients to the body's cells. It consists of muscle tissues controlled by the nervous system and is therefore involuntary.

The heart can be divided into its right and left side by a wall (ventricular septum), as illustrated in Figure 2.1. The heart consists of four main chambers: the right and left ventricles, and the right and left atria. Each side of the heart comprises a ventricle-atrium

system, communicating through the atrioventricular valve (the mitral valve for the left and tricuspid valve for the right) between the atrium and the ventricle. Their walls consist of three layers: the epicardium (the outer layer), the myocardium (the intermediate layer, the muscle), and the endocardium (the inner layer).

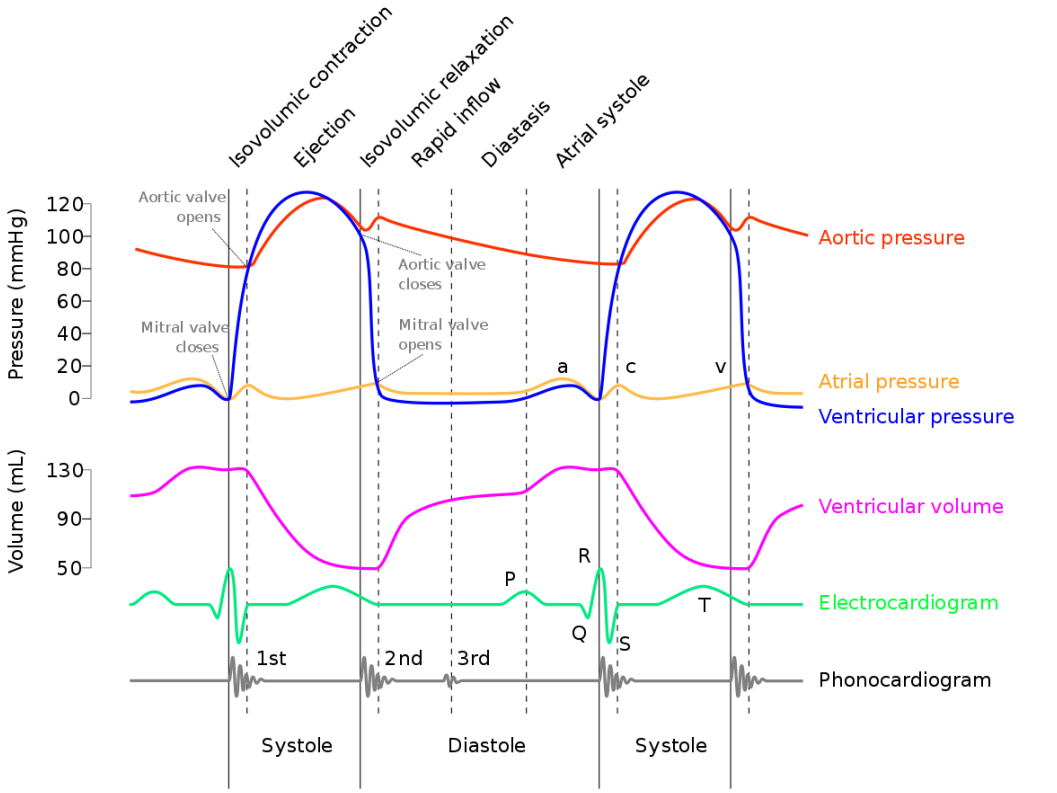

Figure 2.2: Wiggers diagram of a cardiac cycle. Different signals (ECG and phonocardiogram) variations are associated to cardiac events. This figure is reprinted from [2].

The periodical alternation between wall contraction and relaxation originates from the depolarization and repolarization of the muscle membrane, with changes in membrane potential. They initiated at the level of the sinus node, which is a group of cells capable of spontaneously producing an electrical impulse. The process thus begins with the depolarization of the sinus node, which locates at the right atrium. Since the cardiac cells are all connected, the stimulation of one cell will then lead to the stimulation of all the cardiac cells. Therefore, the contraction begins in the atria first and is immediately followed by the ventricles. Meanwhile, the ventricles contract, the atria begin to relax and follow the ventricular relaxations. The electrocardiogram (ECG) measures these electrical activities and shows the differences in potential.

2.1.1.2 Cardiac cycle

Since cardiac motion is composed of regular contraction and relaxation induced by the heart muscle, it is periodic. A cardiac cycle refers to the process that the cardiovascular

system undertakes from the start of one heartbeat to the start of the next. It can be divided into two phases: systole and diastole. As shown in Figure 2.2, systole corresponds to the contraction of left ventricle (blood ejection phase), and the diastole corresponds to the relaxation of the left ventricle (filling phase).

The human heart beats at a rate of 75 bpm (beats per minute) on average. The ventricular systole is approximately 0.3 seconds in duration, and the diastole lasts 0.5 seconds. The atrial systole lasts approximately 0.1 seconds, and the diastole lasts 0.7 seconds [15]. The cycle is approximately the same for the left and right ventricle-atrium systems. I will, therefore, only describe the left ventricle cycle in the following paragraphs.

Ventricular diastole

Diastole corresponds to 60% of the cardiac cycle on average. It consists of 4 phases: the isovolumetric relaxation, the rapid inflow, the diastasis, and the atrial systole (Figure 2.2).

1. The ventricle begins to release during the isovolumetric relaxation, but as the valves (i.e., the mitral and aortic valves) are closed, there is no change in blood volume. The wall relaxation associated with a constant volume consequently leads to a pressure decrease in the ventricle. At the same time, atrial pressure increases due to the blood flow from the pulmonary veins. When the ventricular pressure becomes smaller than the one in the atrium, the mitral valve opens.

2. It then enters the rapid filling (rapid inflow) phase, when most of the ventricle becomes filled (about 75% of the volume). The filling process slows down until a balance is reached between the aortic and ventricular pressures.

3. When the ventricular pressure becomes almost equal to the atrial pressure, there is almost no blood movement during this phase. It is called diastasis or slow filling.

4. Finally, the final filling occurs during the atrial systole (P wave). The contraction of the atrium breaks the pressure balance. The remaining 25% of the ventricle is filled.

The volume of blood in the ventricle at the end of the diastole is called the telediastolic volume.

Ventricular systole

The systole, which is faster (on average 40% of the cardiac cycle), is divided into 2 phases: the isovolumetric contraction and the ejection (Figure 2.2).

1. The systole begins with the ventricular contraction (QRS wave), which causes an increase in ventricular pressure and immediately closes the mitral valve. Because the aortic valve is still closed, the pressure increases rapidly. This phase is named the isovolumetric contraction.

2. The aortic valve opens when the ventricular pressure exceeds the aortic pressure. This phase is the ejection phase.

The small amount of blood that remains in the ventricle at the end of the systole is referred as end-systolic volume.

2.1.2 Ultrasound modality

Clinically speaking, the wildly used non-invasive modalities are Cardiac Magnetic Resonance Imaging (CMRI) and ultrasound imaging [16] [17]. CMRI is known to have high image quality, but the acquisition time is relatively high (20-30 minutes). CMRI can be used to assess the anatomy of the heart but also to investigate blood flow dynamics. However, the time needed to perform such acquisitions limits its use in the clinical routine. Because of its real-time nature, relatively low cost, and bedside portability, ultrasound is the modality of choice to assess the heart anatomy and flow estimation in daily clinical practice.

2.1.2.1 Echocardiography

The application of ultrasound to assess the heart anatomy is called echocardiography. This imaging technique can be used to visualize the anatomical structures dynamically. In this case, the displayed image is named B-mode and is obtained by integrating the amplitudes of the returned echoes. Two types of view are classically performed in clinical routine:

1. The apical views. It allows visualizing the heart in its length. Depending on the angle of the probe, one can then observe the 2-chamber view (left ventricle and atrium), the 3-chamber view (left ventricle and atrium, aorta), the 4-chamber view (right and left ventricles and atria), and the 5-chamber view (4-chamber view with the aorta).

2. The parasternal views. It allows visualizing the heart in its width (short axis) or length (long axis).

These views are transthoracic due to their acquisition at the chest level. Transesophageal ultrasound can also be performed by passing the probe through the esophageal tube, which involves local anesthesia.

2.1.2.2 Doppler echography

Ultrasound can also be used to assess blood flow in clinical routines. In this case, the imaging modality is referred to as Doppler echocardiography. The corresponding technique relies on the Doppler effect (see section 2.2.5). There exist three different types of Doppler acquisitions: continuous Doppler, pulsed Doppler, and color Doppler.

1. Continuous Doppler :
   This technique simultaneously emits and receives continuous transmissions with separate apertures. It uses a relatively constant sinusoidal signal with a narrow bandwidth, allowing the visualization of the velocity spectrum corresponding to the complete set of velocities belonging to the region where the transmitted waves propagated. Since the ultrasound is emitted and analyzed continuously, high-velocity amplitudes can be measured. However, it is not possible to locate the position of the measured velocities along the transmitted waves.

2. Pulsed Doppler :
   This technique uses ultrasound pulses instead of continuous ultrasound transmissions. The user defines a small area where the Doppler shift will be recorded, allowing a precise localization of the measured velocities. This technique recovers the spatial information but at the cost of a lower range of velocities that can be measured. The pulsed Doppler technique is further described in section 2.2.5.

3. Color Doppler :
   The continuous and pulsed Doppler are categorized as spectral Doppler, which is dedicated to velocity measurements. Color Doppler is dedicated to flow visualization. Indeed, this technique is generally used in combination with grayscale (B-mode) images to display blood motion in its anatomical environments. The velocities are color-coded (conventionally red for displacement towards the probe and blue for displacement away from the probe). The principle of color Doppler is detailed in section 2.2.5.

These Doppler techniques share an identical drawback: the recovered velocities correspond to the projection of the actual velocity along the ultrasound beam, thus producing incomplete one-dimensional information of the velocity field.

2.1.2.3 Current limitation

One of the main advantages of echocardiography is its capacity to provide anatomical and functioning information of the heart in real-time. Echocardiography devices are then wildly used in clinics for visualizing the heart. This imaging modality can also measure both anatomical volumes and blood flow velocities directly from the image. The measurements extracted from the B-mode images have been controversial because of poor reproducibility and accuracy. However, recent advancements in DL have shown that it is possible to attain segmentation and classification performances within the inter-observer variability and close to the intra-observer variability [14]. This advancement opens the door to accurate anatomical measurements through echocardiography in the near future.

Concerning the blood flow, continuous and pulsed Doppler techniques allow the measurement of velocities in a limited region, either along the direction of the focused beam or inside a small region of interest (*e.g.* near the mitral valve). Color Doppler allows visual assessment of the blood flow through the entire cardiac cavity. Unfortunately, because of the presence of typical artifacts (*e.g.* aliasing) and noise (*e.g.* clutter), this imaging technique is mainly used for visual inspection of the intraventricular flow. The measurement of 2D or 3D blood velocities through the cardiac cavity is an exciting topic, with the potential to assess different heart pathologies. For instance, a recent study has shown that the characterization of a vortex during the diastolic phase has the potential to detect patients having hypertension but with a preserved ejection fraction [9]. I thus propose in this thesis to generate virtual datasets with motion reference of the blood to feed soon DL algorithms dedicated to the estimation of intraventricular velocity field to compute quantitative measurements. Since my contribution concerns the design of an ultrasound simulation pipeline to generate realistic duplex sequences, I present in the next section a detailed description of the ultrasound image formation, whose fundamental concepts are reproduced in the physical ultrasound simulation pipeline.

2.2 Theoretical background

This part aims to provide a clear understanding of the basics of ultrasound imaging. It is divided into five subsections: acoustic wave, array principles, ultrasound wave transmission, ultrasound image formation, and Doppler echography.

2.2.1 Acoustic wave

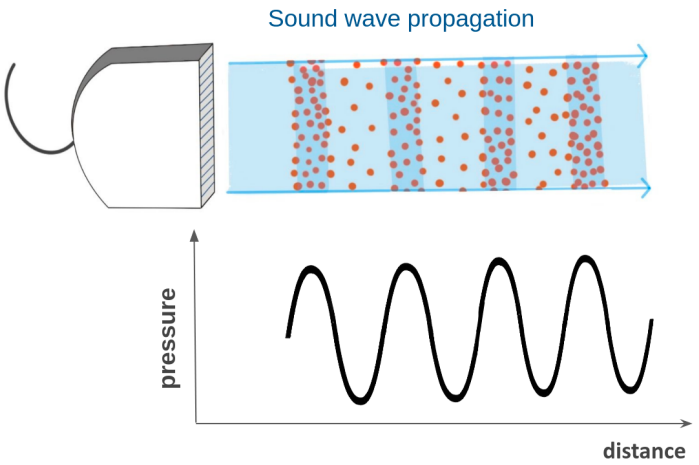

Figure 2.3: An illustration of sound wave propagation. The local particles are moved by the generated acoustic pressure field, which in turn causes the global movement of the sound wave.

The sound wave is defined as a propagating longitudinal wave. Once emitted into the tissue medium, the acoustic wave propagation creates successive compression and rarefaction of the tissue particles parallel to the wave direction, which corresponds to the peaks and troughs of the pressure wave (Figure 2.3). The local displacement of particles, therefore, causes a global displacement of the wave. The sound wave can then be visualized as a sinusoidal movement defined by its amplitude and frequency [18].

The sound waves that humans can hear are within the frequency range of 2KHz to 20KHz. Once above 20 kHz, it is considered to be ultrasound. In the medical field, the frequencies used are in the MHz range. In general, cardiac ultrasound imaging uses ultrasound waves from 1 to 15 MHz.

2.2.1.1 Speed of sound

The propagation speed of the acoustic wave (referred to as c) is defined by the nature of the medium (i.e., density, compressibility, etc.), the temperature, and the pressure. In

particular, the speed of sound can be defined as [19]:

$$c = \sqrt{\frac{\kappa}{\rho}} \quad , \tag{2.1}$$

where ρ is the density of the medium and κ represents the compressibility. In the case of human soft tissue, the sound speed is considered equal to 1540 m/s.

2.2.1.2 Impedance

During the acoustic wave propagation, the pressure wave encounters resistance, and the propagation velocity changes due to the density of the medium. This phenomenon is called impedance, which describes how much resistance an acoustic wave encounters as it passes through a tissue. At the interface of two distinct media, the difference in impedance will directly impact the proportion of the transmitted or reflected wave. The more significant the difference in impedance, the more the wave will be reflected. In order to know what percentage of the acoustic wave will reach the desired depth and how fast the wave will travel through the medium, the impedance of the different tissues of the human body is required. Impedance is defined as [18]:

$$Z = \rho c, \tag{2.2}$$

with ρ the density of the medium in kg/m^3, c the sound velocity in m/s and Z the acoustic impedance.

2.2.1.3 Scattering

The trajectory of an acoustic wave can be slightly or significantly modified when passing through an interface of two different media. At the level of the interface (where the dimension of the objects is much larger than the wavelength.), this phenomenon can be the specular reflection, the diffuse reflection, the refraction, or their combinations (illustrated in Figure 2.4).

In ultrasound, scattering situations happen where the dimensions of the scatterer are lower than the wavelength of the insonified wave. There are different categories of scattering. If the incident wavelength is greater than the size of the scatterer at least ten times as most of the cases in human tissue, then we are in a Rayleigh regime (Rayleigh scattering). The incident wave is scattered randomly in all directions with maximum intensity in the backscattering direction. The intensity of backscattered wave is proportional to the fourth of the incident wave frequency. In this thesis, only Rayleigh scattering is considered. In this context, the insonified medium can be seen as a scattering medium where each individual point source will back-scatter the wave to the transducer. This information will then be used to form both the B-mode and color Doppler images. The speckles (the granular texture found on ultrasound images [20]) appear during the reconstruction of the ultrasound image, which results from the summation of the interference of the back-scattered waves.

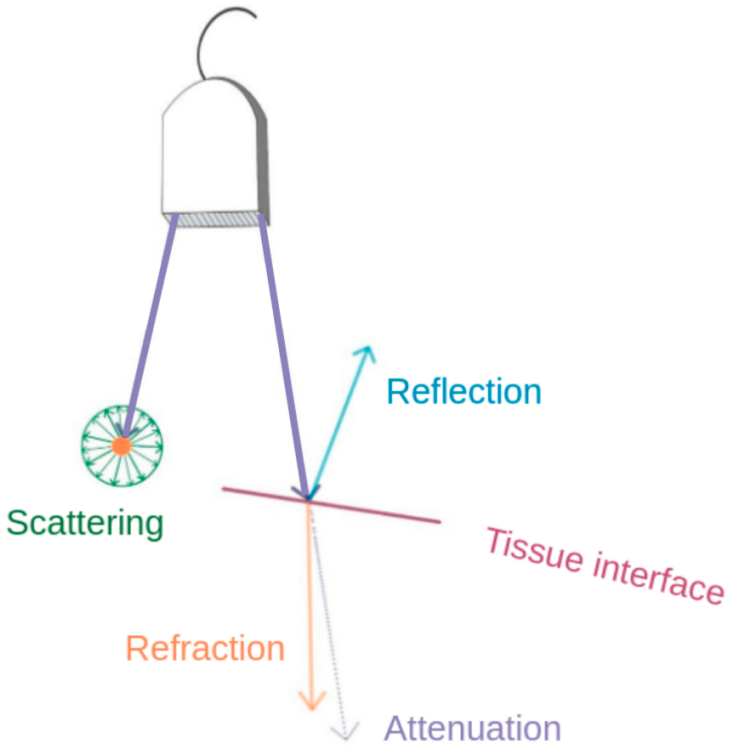

Figure 2.4: Illustration of the different phenomena when an incident wave reaches an interface with different impedance properties.

2.2.1.4 Transmission and reception

During its transmission, the wave faces the phenomenon of attenuation due to absorption. The attenuation can be seen as the conversion of the energy from kinetic energy into thermal energy. Moreover, the attenuation depends on the frequency: higher frequencies are more attenuated than lower frequencies. Attenuation (A) is measured in decibels as [21] :

$$A = \alpha \times 2 \times d \times f, \tag{2.3}$$

with α the attenuation coefficient, d the depth and f the frequency.

2.2.2 Array principles

In the clinical ultrasound acquisitions, the ultrasound wave is emitted and later received by an ultrasound array (also called a probe or a transducer).

2.2.2.1 Probe

In ultrasound devices, a probe generates the pressure waves which are transmitted into the targeted tissue. The same probe then receives the echoes returned from the structures encountered by the transmitted waves. The transducer consists of piezoelectric elements which can convert an electrical signal into a compression wave and vice versa [18] [22] [23].

The probe emits a signal which is band-limited and centers on a central frequency. This bandwidth plays a key role in the image resolution (see section 2.2.2.4).

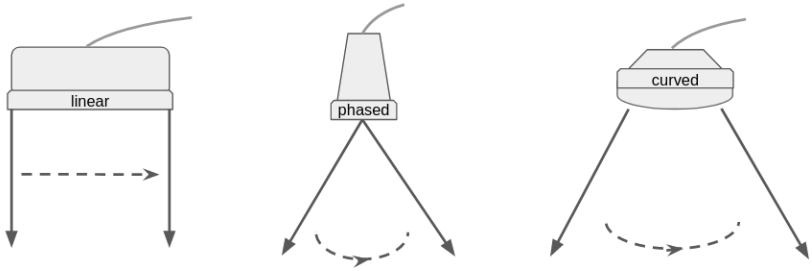

Figure 2.5: Most common types of ultrasound probes.

The most common ultrasound transducers are the linear probe, the phased probe, and the convex probe (Figure 2.5).

- Linear probe:
  This type of probe involves aligned piezoelectric elements (typically 64-256 elements). Usually, part of the elements (sub-opening) is used to transmit and receive a wave. The use of these probes covers vascular, breast, and healthcare (muscle, fat) applications.

- Phased probe:
  In contrast to linear arrays, phased arrays are smaller (typically 32-128 elements) but maintain the same linear arrangement of elements. In echocardiography, a phased array transducer is generally used because of its small footprint, allowing imaging of less accessible locations (such as the heart, using a small space between the ribs). Due to its smaller aperture, all elements are used to transmit and receive a single wave.

- Curved probe:
  For this type, the alignment of the elements follows a curve. It has a wide footprint for imaging a large area (typically 64-192 elements). It is generally used in abdominal or prostate applications.

Since this thesis focused on echocardiography, only the phased array will be considered. Figure 2.6 provides some practical terms used in the description of the probe. In particular, the spacing between the probe elements is called "kerf", and the distance between the center of two elements is called "pitch".

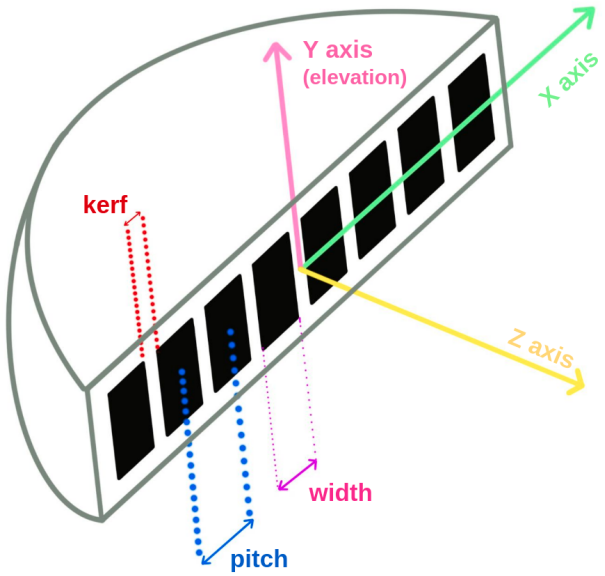

Figure 2.6: Schematic representation of a phased array.

2.2.2.2 Grating lobe

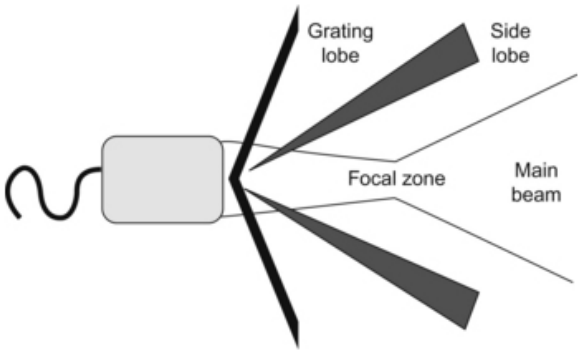

Figure 2.7: Illustration of a focal wave with corresponding side lobes and grating lobes.

When an ultrasonic wave is transmitted towards a particular location, part of the energy is transmitted out of this area, creating side lobes and grating lobes (Figure 2.7). Side lobe beams surround the central beam with low amplitudes, whereas grating lobes occur at more steered angles. The side lobes and grating lobes are created due to the discretization of the probe. In fact, ultrasound probes do not consist of a single element but an alignment of individual small elements (Figure 2.6). The distance between the elements is at the origin of constructive interferences that lead to lobes of amplitude similar

to the main lobe. During the reception, the echoes of these secondary transmissions are processed as the echoes coming from the main lobe, resulting in reconstruction artifacts (Figure 2.8).

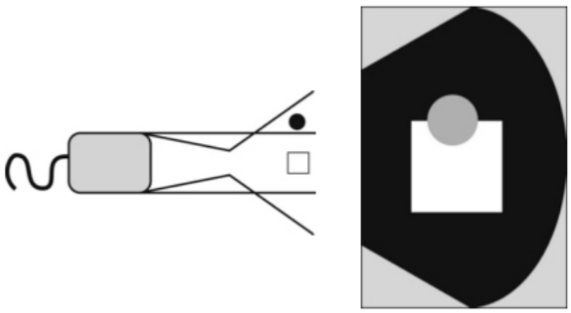

Figure 2.8: The artifacts due to side lobes and grating lobes. This figure is adapted from [3].

2.2.2.3 Directivity

The directivity measures the amount of energy emitted in a specific direction. For a single element, the directivity in the far-field is defined under the form of a *sinc* function as [24]:

$$D_{element}(\theta) = \frac{sin(\pi \frac{b}{\lambda} sin\theta)}{\pi \frac{b}{\lambda} sin\theta}, \tag{2.4}$$

where b is half of the size of the element, θ is the angle corresponding to the width of the beam and λ is the wavelength. From this equation, one can see that the size of the probe elements directly influences the directivity. As illustrated in Figure 2.9, the larger the element is, the greater the energy is concentrated in a narrow region (thus considered directional). However, if the element is large enough, side lobes are also observed with a narrow pressure field. In addition, the steering will be more difficult with large elements.

2.2.2.4 Resolution

The image resolution determines the minimum distance for which adjacent objects can be separated. For an ultrasound sequence, resolution can be characterized in four types: the three spatial resolutions: axial (depth), lateral (width) and elevation (thickness), and the temporal resolution. They depend on different parameters [21] and have a direct impact on the image quality. The representation of the coordinate system used clinically in ultrasound is shown in Figure 2.10.

1. Axial resolution:
   Axial resolution is the resolution parallel to the ultrasound beam. It is the minimum distance between two objects (scatterers) that can be imaged as separate and

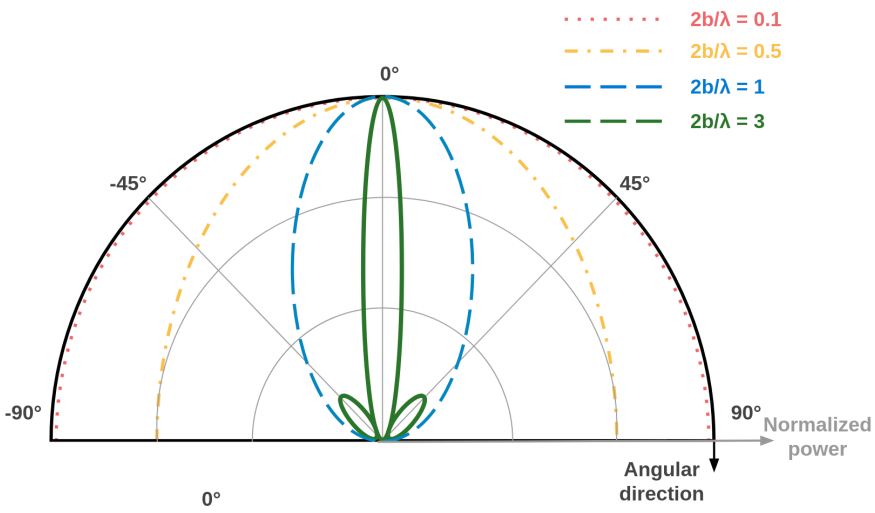

Figure 2.9: Illustration of the relation between the element size with respect to the wavelength and the directivity.

distinct. This minimum distance is half of the pulse length for the axial resolution [18]. Pulse length corresponds to the size of the pulse emitted in the insonified medium, as illustrated in Figure 2.11. The pulse length is defined by the wavelength multiplied by the number of wave cycles per pulse. Therefore, the resolution depends on the frequency of the probe and the number of cycles. In terms of the probe frequency, the higher the frequency is raised (i.e. λ is lowered), the better the axial resolution is. However, the high frequency results in a significant attenuation, which in turn deteriorates the maximum depth the ultrasound beam can attain. A compromise between the axial resolution and maximum depth must be addressed. In terms of the number of cycles, it usually depends on the type of image to acquire. For B-mode images, shorter pulses are used compared to Doppler images.

In echocardiography, ultrasound waves within the range of 4-7MHz are generally used for the examination of adults. For example, if a central frequency of 2.5 MHz is chosen to image the human tissue (with c = 1540 m/s), a wavelength of λ = 0.62 mm. If each pulse contains 3 cycles, then the pulse length L_{pulse} = 3 × 0.62 = 1.86 mm. In this scenario, the axial resolution is, therefore R_{axial} = 1.86/2 = 0.93 mm. In ultrasound, depending on the applications, probes with a central frequency between 2 and 30 MHz are used (intravascular ultrasound uses frequencies up to 30 MHz), which means a wavelength in the range of 0.05 to 0.77 mm for human tissue and an axial resolution varying from 0.08 mm to 1.16 mm. In echography, the most accurate resolution is the axial one.

2. Lateral resolution:
The lateral resolution refers to the ability to recognize separate objects localized at the same depth but with a different lateral position. It is about four times worse than the axial resolution. It primarily depends on the width of the main lobe of the

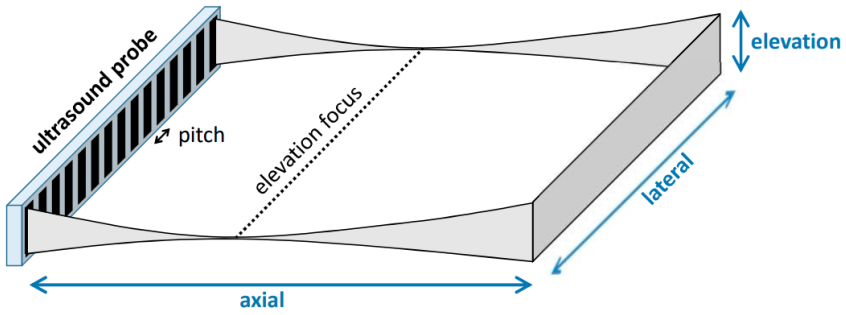

Figure 2.10: Schematic representation of axial, lateral and elevation axis of an ultrasound probe. This figure is reprinted from [4].

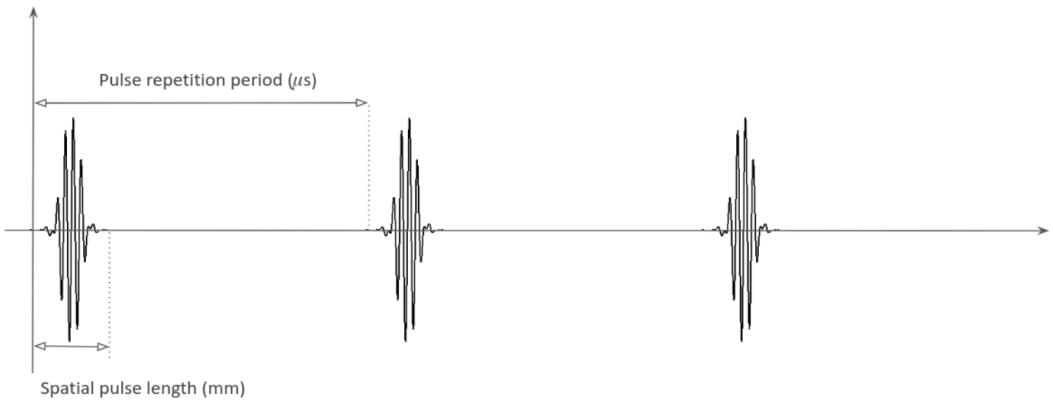

Figure 2.11: Schematic representation of ultrasound pulses.

transmitted wave. It also depends on the size of the elements and the aperture of the probe.

Since the beam width varies from different transmission schemes, the lateral resolution depends on the type of transmission used. Its expression is developed in section 2.2.3.1 for focused wave and in section 2.2.3.2 for diverging waves and plane waves.

3. Elevation resolution:
   The elevation corresponds to the thickness of the beam (which is perpendicular to the image plane). The elevation resolution depends on the height of the probe elements [18] and the azimuthal focus of the probe's acoustic lens. In echography, it is the lowest resolution and is about several millimeters.

4. Temporal resolution:

The temporal resolution depends on the time between two frames in an ultrasound sequence. It is generally defined as the number of frames per second (in hertz), which corresponds to the frame rate. Its value mainly depends on the depth and sectorial width of the acquisition. In echocardiography, the frame rate used in clinical routine remains between 30 to 60 fps (frame per second).

2.2.3 Echocardiography transmission schemes

In order to simulate echocardiographic images that are realistic enough, it is necessary to understand the clinical acquisition protocol and then reproduce the essential procedures to generate the desired ultrasound sequences. The following section presents different transmission (*i.e.* Diverging Wave (DW), Focused Wave (FW)) schemes that can be used in ultrasound imaging.

2.2.3.1 Focused wave

The conventional ultrasound techniques use focused beams to reconstruct an image. For each piezoelectric element, a different time delay is applied to its firing so that the focused waves from different elements can simultaneously arrive at the focal point. In this way, either the entire aperture of the probe or a part of the elements of the probe are used to focus the energy at a particular point in the medium. By adapting the delays, the area of interest is then swept by different ultrasound beams, which creates scanlines. These scanlines reconstruct the complete image of the scan region. In general, focused beams in the range of 64 to 128 are used to reconstruct an image, varying according to the desired lateral dimension and lateral resolution. Consequently, the greater the number of scanlines is used, the lower the frame rate is.

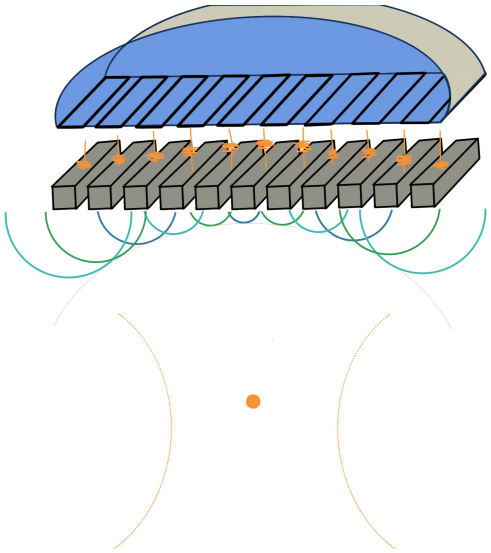

Figure 2.12: Illustration of the focused transmission scheme used in conventional ultrasound imaging.

Resolution with focused wave

1. Lateral resolution:
   The lateral resolution at the focal point is defined as [19]:

$$R_{lat} = \frac{F}{D} \times \lambda, \tag{2.5}$$

   with λ the wavelength, F the distance to the focal point and D the aperture (the fraction F/D is also known as f-number $f = F/D$). Therefore, the lateral resolution can be improved by increasing the aperture, increasing the frequency or decreasing the distance to the focal point. The size of the aperture is limited by the directivity (see section 2.2.2.3). It also influences the Signal to Noise Ratio (SNR) of the ultrasound image. Indeed, large apertures result in more data being beamformed to reconstruct one point, which increases the SNR. So, the choice of the f-number is essential in terms of the SNR and the directivity. Finally, the lateral resolution is optimal at the focal point and deteriorates as it moves further away (towards the probe or towards infinity).

2. Temporal resolution:
   The frame rate F_r can be calculated as follows:

$$F_r = \frac{c}{N_t \times 2d} \quad , \tag{2.6}$$

   with c being the speed of sound in the medium, d the maximum depth and N_t the number of transmissions. From this equation, one can see that the increase of the temporal resolution can be reached through:

   - a decrease of the depth of the reconstructed image
   - a reduction of the number of scanlines (thus the width of the sector)
   - an increase of the width of the reconstructed region from the transmission of a single ultrasound beam (at the expense of lateral resolution).

2.2.3.2 Diverging wave

One of the issues with conventional ultrasound resides in its relatively limited frame rate. For instance, this problem occurs when imaging /quantifying the rapid movement of the flow or wall over a large area (*e.g.*, the entire LV). Other transmissions have been proposed to speed up the image acquisition process, such as ultra-fast imaging [25]. The general idea behind the technique is to image a larger part of the image in a single transmission. Different transmission strategies are possible, such as plane wave, diverging wave, Multi-Line Transmission (MLT), or Synthetic Aperture (SA) [26] [27]. In this thesis, I only used diverging wave to estimate color Doppler images. I thus present the corresponding formalism in the following.

Instead of focusing the beam on one point of the image, the main idea is to insonify the entire sector into one transmission with diverging waves [28]. Indeed, with its diverging nature, it is possible to image a wide area, which is interesting in the case of phased array probes.

In order to create a diverging wavefront, a virtual source is defined behind the probe. To calculate the location of the virtual source (and thereby calculate the delays associated with each element), one needs the aperture and the width of the intended sector (*i.e.* angle β). For a firing without angulation (illustrated in Figure 2.13), the coordinates of the virtual source ($X_{VirtualSource}$, $Z_{VirtualSource}$) can be defined as [29]:

$$Z_{VirtualSource} = \frac{\frac{\alpha}{2}}{tan\frac{\beta}{2}} \quad , \tag{2.7}$$

$$X_{VirtualSource} = \frac{\alpha}{2} \quad . \tag{2.8}$$

Where α corresponds to the size of the aperture, and angle β corresponds to the width of the intended sector.

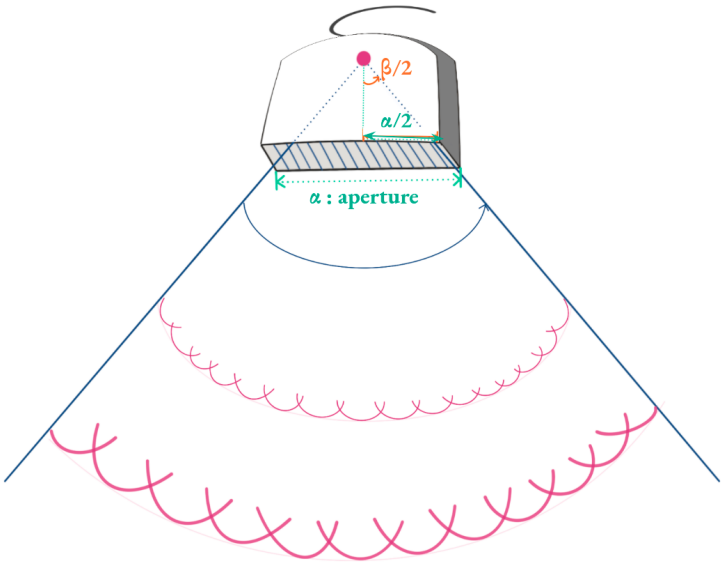

Figure 2.13: Divergent wave virtual source.

In order to add an angulation θ to the beam orientation (see Figure 2.14), the coordinates of the virtual source (X_{source}, Z_{source}) are then defined as follows:

$$Z_{source} = \frac{\alpha}{\tan(\theta - \frac{\beta}{2}) - \tan(\theta + \frac{\beta}{2})}, \tag{2.9}$$

$$X_{source} = Z_{source} \ \tan(\frac{\beta}{2} - \theta) + \frac{\alpha}{2}, \tag{2.10}$$

with β the angle that represents the width of the sector, θ the angulation of the beam, and α the aperture.

Once the coordinates of the virtual source have been obtained, we can obtain the distances between each element and the virtual source, and find the minimum distance:

$$dist_{min} = \min_{n \in N} \sqrt{(X_n - X_{source})^2 + Z_{source}^2}, \tag{2.11}$$

where X_n corresponds to the x coordinates of the n^{th} element. This shortest distance between the virtual source and the nearest probe element guarantees the minimum delay is 0. we can thus calculate the delays for each element of the probe as follows:

$$\tau_n = \frac{\sqrt{(X_n - X_{source})^2 + Z_{source}^2} - dist_{min}}{c}. \tag{2.12}$$

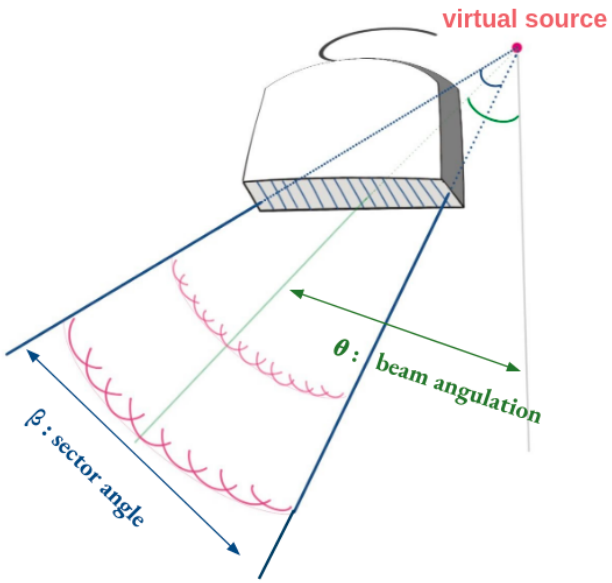

Figure 2.14: steered wave virtual source .

Resolution with diverging wave

1. Lateral resolution:
   In the lateral resolution expression given in equation 2.5, the distance to the focal point is used, but there is no focal point in ultrafast imaging. The lateral resolution can be measured experimentally by estimating the Point Spread Function (PSF) [30]. Recent work [31] has examined the factors that influence lateral resolution. It was observed that :

   - the lateral resolution increases with the size of the aperture (for a fixed pitch value).

- the lateral resolution decreases with the depth.
- the increase of the central frequency of the probe results in a better resolution.
- the bandwidth mainly affects axial resolution and not lateral resolution.
- the number of elements (without changing the aperture) enhances the resolution up to a certain threshold. Changing the number of elements while keeping the same aperture means changing the pitch. However, it was shown in section 2.2.2.2 that the pitch must be lower than $\lambda/2$ to avoid grating lobes. The study found that once this threshold is crossed, the resolution is no longer affected. Therefore, the number of elements does not seem to play a role in the lateral resolution.

This leads to the definition of an empirical expression of lateral resolution for plane wave imaging [31]:

$$R_{lat} = C \times \frac{\lambda z}{D}, \tag{2.13}$$

with λ the wavelength, z the depth, D the aperture and C a constant which depends on the system used.

2. Temporal resolution:
As each transmission covers the whole region of interest, one transmission can generate one entire image. Therefore, the frame rate is defined by the travel time of transmissions, which depends only on the depth and the propagation of the speed of sound in the medium. The frame rate is defined as:

$$Fr_{max} = \frac{c}{2d} \quad , \tag{2.14}$$

where Fr_{max} the maximum rate, c is the speed sound in the medium and d is the depth to be imaged.

The use of diverging wave allows a significant increase in temporal resolution but at the expense of the lateral resolution. In addition to the limited image quality, these transmissions produce low sound pressure as the energy is dispersed throughout the image area. This results in a lower SNR and a higher attenuation at depth [27]. Compounding solutions (use of several DW to reconstruct one image) are classically used to improve the SNR but at the cost of the final frame rate.

2.2.4 US image formation

The following paragraphs introduce the post-processing applied to the received ultrasound signals to reconstruct an image and to estimate Doppler information. All the elements of the probe receive echoes resulting from the scattering of the transmitted waves by tissue structures. Scatterers with a high reflector coefficient (significant difference in acoustic impedance) produce signals with higher amplitudes. The echoes received by the piezoelectric elements of the probe are transformed into Radio Frequency (RF) signals. From these RF signals, demodulation and beamforming operation are performed to either reconstruct the B-mode images or estimate the Doppler information.

2.2.4.1 Demodulation

Since the RF signals are band-pass real signals, all the information is contained around the center frequency. Its spectrum is therefore symmetrical (Hermitian symmetry). In terms of computational time, it is thus preferable to use a modified version of the original RF signals to work on fewer samples, but with the same information content. RF signals are thus converted into In-phase and Quadrature (IQ) components by shifting the spectrum with respect to the central frequency of the probe [32]. This conversion is called demodulation and consists of three steps:

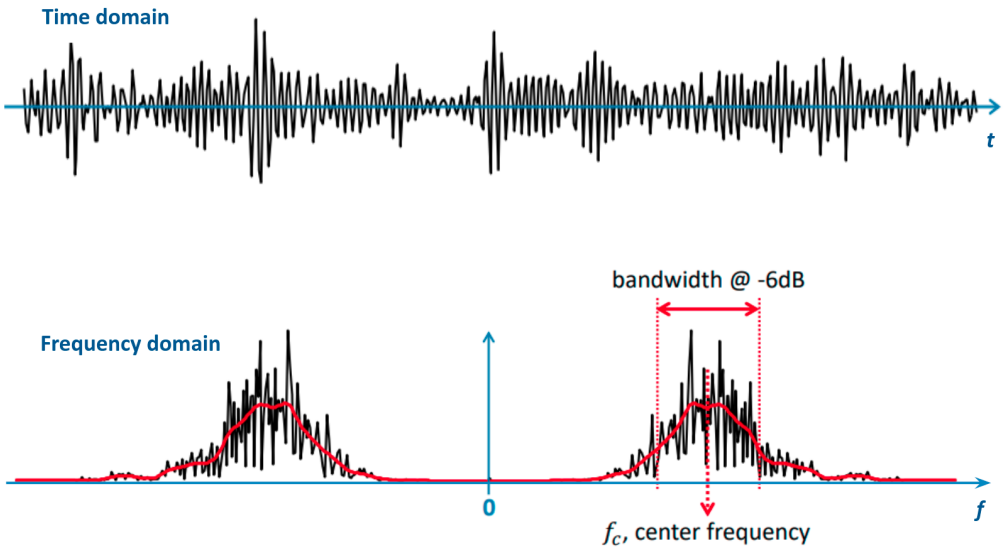

Figure 2.15: Illustration of a RF signal in the time domain and frequency domain. This figure is reprinted from [4].

1. the "down mixing" procedure relocates the central frequency of the signal spectrum on 0. This is done in the following way:

$$RF_{shift}(t) = RF(t) \times e^{-i2\pi f_c t}, \tag{2.15}$$

2. low-pass filtering aims to keep only the spectrum around the central frequency (which is now around 0) and remove the symmetrical part in the original spectrum.

3. decimation procedure reduces the number of signal samples. Indeed, Nyquist–Shannon sampling theorem states that the filtered signal can be preserved with a sampling frequency of twice the cut-off frequency (*i.e.*, the maximum frequency of the previous low pass filter) without loss of information.

We therefore have :

$$IQ(t) = LP(\underbrace{RF(t) \times \cos(2\pi f_c t)}_{I} + \underbrace{i \times RF(t) \times -\sin(2\pi f_c t)}_{Q}), \tag{2.16}$$

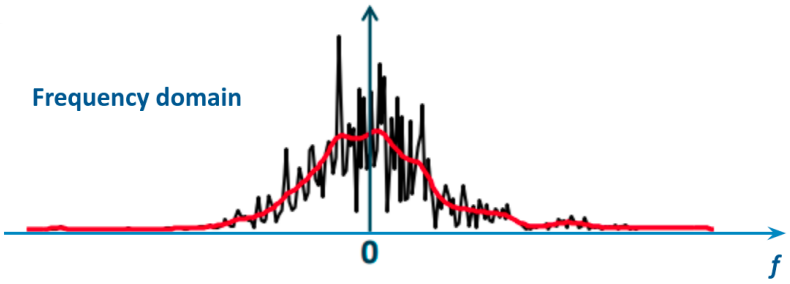

Figure 2.16: Illustration of RF signal after demodulation in the frequency domain. The displayed spectrum is reconstructed with the IQ signals. This figure is reprinted from [4].

where f_c indicates the central frequency and LP denotes a low-pass filter function. I represents the real part of the signal and Q the imaginary part. The result is an asymmetrical spectrum, *i.e.*, a complex signal.

The IQ demodulation procedure integrally preserves the information content in the band-pass signal, and the reconstruction of the original RF signal from the IQ signal is possible. IQ signals are directly used to reconstruct B-mode images and compute Doppler information (which will be detailed in section 2.2.5).

2.2.4.2 Beamforming

The scatterers present in the insonified medium return the signal in all directions after being hit by the ultrasound wave (see section 2.2.1.3). The backscattered wave has a circular wavefront. Because the human tissues can be seen as media with strong scattering effects, the backscattered wave will form interface patterns. Beamforming aims to control the interference pattern to reform the echoes spatially, correct the distortion, and have the proper image. One of the earliest and most widely used methods in ultrasound imaging is the delay-and-sum technique, which is firstly used in seismology as "diffraction-summation" [33]. By using the time of flight τ (i.e., the time of round-trip element-reflector-element), we can find the position of the source :

$$\tau = 2 \times \frac{d}{c} \quad , \tag{2.17}$$

where d is the distance between the element and the reflector, and c is the speed of sound in the medium. We can compute the distance, and therefore the delay, between that reflector and each element. The arrival time of echoes can be determined at each element and then be located in the IQ signals generated by the element. The signals recorded on each element are then added together with the corresponding delays (Figure 2.17) to reconstruct an image of the insonified medium.

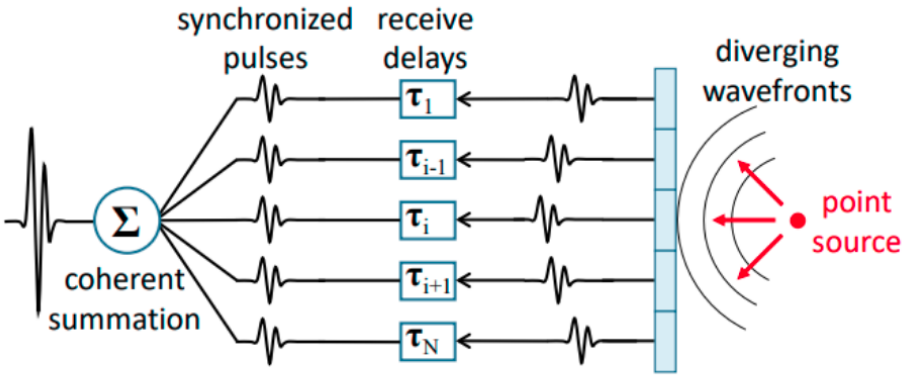

Figure 2.17: Illustration of delay-and-sum beamforming technique. This figure is reprinted from [4].

Transmission delays can be used to obtain a generic expression of τ_{go} [30] :

$$\tau_{go}(x,z,x_n) = T_n + \frac{\sqrt{z^2+(x-x_n)^2}}{c}, \tag{2.18}$$

where T_n is the transmission delay for element n at $(x_n,0)$. The return time to the element is :

$$\tau_{return}(x,z,x_n) = \frac{\sqrt{z^2+(x-x_n)^2}}{c}. \tag{2.19}$$

Other beamforming methods exist based on Fourier transform [34] or neural networks [35], but these techniques are beyond the scope of this thesis.

2.2.5 Doppler echocardiography

The B-mode image can be reconstructed from IQ signals after beamforming. During the acquisition of duplex sequences, the Doppler velocities are computed from the phase information of IQ signals with additional steps (clutter-filter, Doppler velocity estimation). Besides, a de-aliasing step is often performed as post-processing. A general presentation of the used of Doppler effects in echocardiography is presented in the following.

2.2.5.1 Doppler effect in Ultrasound

Doppler effect

First described by Christian Doppler, the Doppler effect is the change of wave frequency observed when a wave source is in relative motion with respect to an observer. In the context of Doppler echocardiography, the change of frequency is observed when red blood cells are in relative motion to the probe. It provides a way to measure blood motion for a more thorough diagnosis. The Doppler frequency f_d is written as:

$$f_d = f_t - f_r = \frac{2 f_t v \cos\theta}{c} \quad , \tag{2.20}$$

where f_t is the transmitted frequency, f_r is the received frequency, v is the relative speed of movement between the transmitter and the receiver, θ is the angle representing the direction of movement according to the probe coordinate system, and c is the speed of sound in the medium.

Therefore, it can be determined whether there is an approaching or distancing movement between the blood and the probe. The speed of movement v can be computed as:

$$v = \frac{c f_d}{2 f_t \cos\theta} \quad . \tag{2.21}$$

In Doppler echography, f_t corresponds to the central frequency of the transmitter. Since θ is not known in cardiac imaging generally, we can only calculate the velocity in the probe-reflector axis, which is called Doppler velocity. The Doppler velocity is defined by $v_D = v\,cos\theta$. The Doppler velocity differs from the actual velocity with respect to θ. In the extreme case where the motion is perpendicular to the axis of the Doppler velocity, the Doppler velocity will be zero. As the human body consists of multiple reflectors moving at different speeds, the returned signal does not contain a single frequency but a spectrum of frequencies.

Resolution

In order to image the motion with an adequate temporal resolution, it is essential to acquire signals at a high frame rate. Since the motion of blood can reach high speeds, it is necessary to have a high frame rate to track the blood motion. In conventional cardiac imaging, each Doppler image is reconstructed line by line, and each line is obtained from several transmitted pulses (usually between 8 and 16). The number of pulses transmitted per line is defined as the packet size. The sweeping procedure and packet size are a constraint for high frame rate in conventional imaging. To solve this issue, research studies on Doppler are focusing on the use of plane waves or diverging waves, which allow a higher frame rate [36]. Indeed, by using a single transmission to insonify the entire sector, the maximum rate can then be defined by:

$$Fr_{max} = \frac{c}{2 d N_e} \quad , \tag{2.22}$$

with c being the speed of sound in the medium, d the maximum depth, and N_e the number of Doppler transmissions used to reconstruct the velocity field. By doing so, it is

possible to increase the packet size (*e.g.*, from 16 to 32 in duplex mode), but at the cost of a lower SNR and resolution compared to conventional Doppler techniques.

The axial resolution will be lower in Doppler compared to the conventional echocardiography. Indeed, to evaluate frequency changes between the transmission and reception, Doppler acquisitions require longer pulses than B-mode imaging. Since the axial resolution relies on the pulse length (see section 2.2.2.4), the axial resolution of Doppler imaging decreases compared to the B-mode images. Despite the increased interest in using plane waves or diverging waves, these techniques are not yet used in clinical routine. We thus decided to concentrate on conventional Doppler techniques in the remaining of this chapter.

Aliasing

In Doppler ultrasound, spectral aliasing is a common artifact, which refers to a phenomenon of inability to record direction and velocity accurately due to an insufficient sampling rate. Aliasing can occur in pulsed and color Doppler. In these cases, aliasing of the velocity spectrum is observed. The result of aliasing is an abrupt direction change of high-velocity blood flow at high velocity, making flow backwards in the visualization. Nyquist–Shannon sampling theorem assumes that the discrete representation of a signal requires a sampling frequency greater than twice the maximum frequency present in that signal. Aliasing occurs when the maximum frequency of the Doppler signal exceeds half the sampling rate. In ultrasound imaging, the temporal sampling rate corresponds to the Pulse Repetition Frequency (PRF). The maximum speed that can be detected is the Nyquist speed v_N. It is determined as follows:

$$v_N = \frac{c \times PRF}{4 f_c} \quad . \tag{2.23}$$

The PRF also influences the propagated depth ($PRF = c/2d$, d being the depth), a high PRF limits the maximum depth. The value of PRF is therefore a compromise between Nyquist speed and depth. For a higher Nyquist speed, it is possible to reduce the central frequency at the expense of spatial resolution.

2.2.5.2 Clutter filter

The phase information of IQ signals can be used to retrieve travel speeds. Nevertheless, there are unwanted echoes contained in these signals, known as clutter noise. The clutter noise is a major part of the IQ signals in echocardiography since it is produced by the high-amplitude, slow-movement myocardial tissues. In order to recover the tissue motion, a low-pass filter can then be applied to the IQ signals as their contents correspond to the low frequencies. To estimate blood velocities from the Doppler signals, it is then necessary to recover the clutter noise corresponding to the tissue information. To this purpose, a wall filter can be used to separate blood from tissue information [23, 37]. A high-pass filter can be used to separate the spectra of blood and tissue by cutting at a given frequency (Figure 2.19 a). However, the two spectra are rarely easily separated, and the overlap of the spectrum makes it difficult to choose the cut-off frequency (Figure 2.19 b).

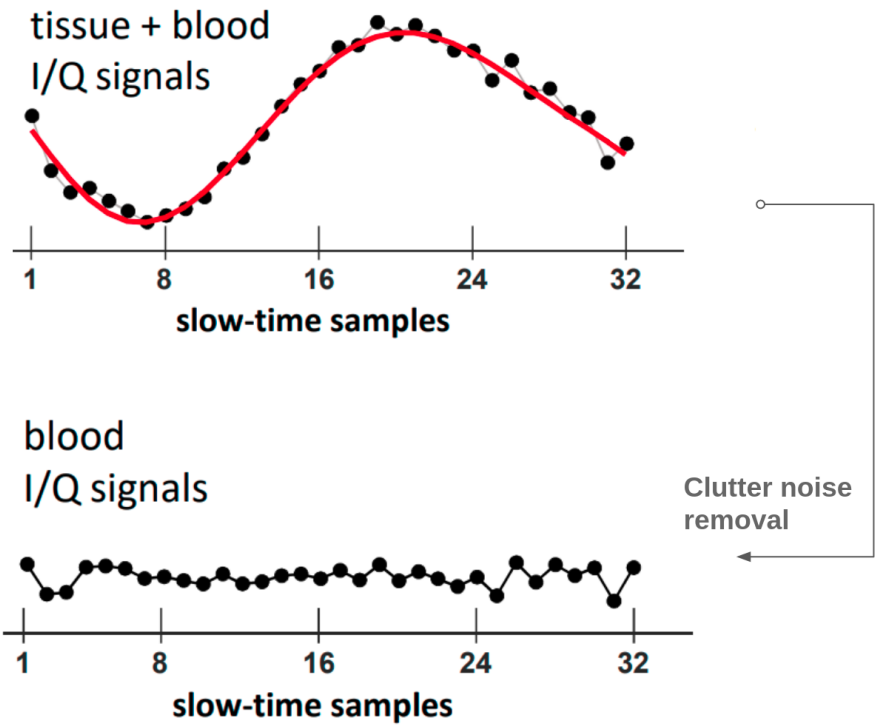

Figure 2.18: Illustration of clutter filter method. The red curve corresponds to clutter noise, resulting principally from the surrounding tissues, which is detected by a high-pass filter and then removed for the estimation of blood information. This figure is adapted from [4].

Several types of filters exist, the main ones being the FIR, IIR, polynomial, and SVD filters.

1. FIR high-pass filters:
   The Finite Impulse Filter (FIR) has an impulse response of finite duration (*i.e.*, input values are of finite length), therefore making the filter stable. It is defined as:

$$y_n = \sum_{k=0}^{N} a(k)\, x(n-k) \quad , \tag{2.24}$$

   where x is the input data and a is the filter impulse response. The order of the filter defines the sharpness of the cut-off region. A higher order is appropriate for a fine cut. However, the number of samples in the signal may limit the use of a higher order. Furthermore, it has been shown that the FIR associated with an auto-correlator to calculate Doppler velocity tends to introduce a bias in velocity estimation [38].

2. IIR high-pass filters:
   The Infinite Impulse Filter (IIR) is a recursive filter. The IIR filter takes the current

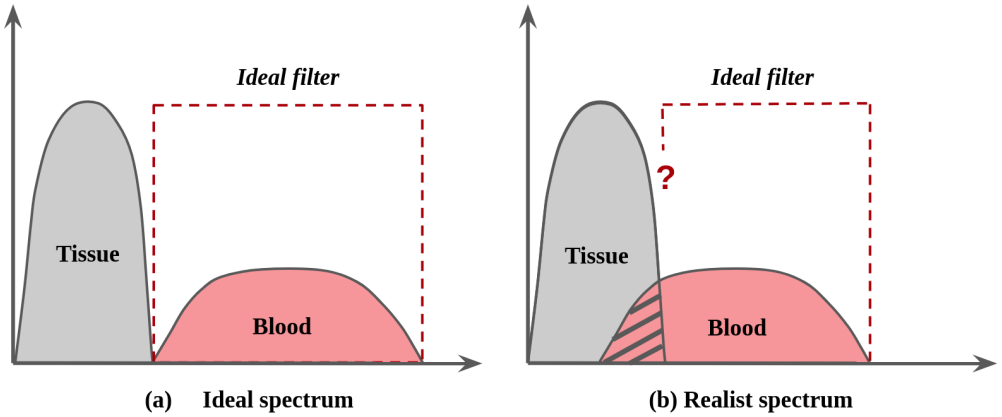

Figure 2.19: (a) Doppler frequency spectrum in the ideal case with separation of blood and tissue; (b) Doppler frequency spectrum with overlap between the frequencies of blood and tissue

and previous inputs together with the previous outputs to compute the current output. It is defined by:

$$y_n = \sum_{k=0}^{N} a(k)\, x(n-k) + \sum_{j=0}^{P} b(j)\, y(n-j) \quad , \tag{2.25}$$

where x is the input data, y is the output data, and a and b is the filter coefficients. Similar to FIR filters, the filter performance for noise reduction is limited by the number of samples in the input signals, causing a coarse removal of high frequencies from blood signals.

3. Polynomial filters:
The polynomial filters seek to find a polynomial function that can approach the clutter signal with respect to the chosen order of the polynomial. The estimated clutter noise is then subtracted from the original signal to recover the desired signal [39]. In this way, the high frequencies contained in the blood signal are retrieved. It can be written in the form [37] [40] :

$$A^f = (I - \sum_{k=1}^{K} b_k b_k^{*T})\, A \quad , \tag{2.26}$$

where A is a vector containing the values of the signal, A^f the filtered signal, and b_k a set of vectors of an orthonormal base. For example, Legendre polynomials can be used. The higher the order, the more low-frequency components are removed.

4. The SVD and EVD filters:
   The SVD and EVD filters deduce the blood signal respectively through Singular Value Decomposition (SVD) or Eigen Value Decomposition (EVD). With their mathematical natures, the eigenvalues and singular values can be transformed (via $\Lambda = \Sigma^2$, where Λ corresponds to the eigen values and Σ corresponds to singular values), resulting in identical signal decomposition. In the SVD case, a matrix A of size $m \times n$ is decomposed as follows:

   $$A = U\Sigma V^* \quad , \tag{2.27}$$

   where U is a unitary matrix of size $m \times m$, V is a unitary matrix of size $n \times n$ and Σ is a diagonal matrix of size $m \times n$. The values of the diagonal of Σ are real positive or zero and are called the singular values.

   This decomposition can be used to extract the different information from the signal. The first range usually contains the main energy of the signal. In our case, the main information contained in the signals corresponds to the tissue. It can therefore be deduced that the blood signal is mainly contained in the last ranges. In order to filter the tissue, it is sufficient to subtract the first ranges during the reconstruction of the signal such as :

   $$A^f = \sum_{n=t}^{N} u_n \sigma_n v_n^* \quad , \tag{2.28}$$

   where t designates the range from which the signal is reconstructed.

2.2.5.3 Doppler velocity estimation

The Doppler velocity of intraventricular flow can be deduced from the IQ signals after the clutter filter. For this purpose, several methods exist depending on the type of velocities that we want to obtain. The pulsed Doppler and color Doppler will be presented in the following parts.

1. Pulsed wave Doppler:
   In pulsed wave Doppler, a small area within a B-mode frame, from which we want to estimate the motion, is first defined by an expert (the two horizontal short lines in Figure 2.20). The transmitted waves are focused in this area and the returned signals are then used to estimate the corresponding velocities [8]. As shown in Figure 2.20, the velocity spectrum (the bottom) depicts all the present velocities in this chosen area along the time axis, while the color Doppler (the top) remains as a technique dedicated for visualization.

2. Color Doppler:
   Color Doppler provides a visual assessment of motion information on a large area. In clinical routine, it is often used in duplex mode with B-mode image transmissions, displaying the surrounding tissue and the location of the observed motion. However, the transmissions for both B-mode images and Doppler information limit the packet size. By convention, the colors used are red for motion towards the probe and blue for motion away from the probe (Figure 2.21).

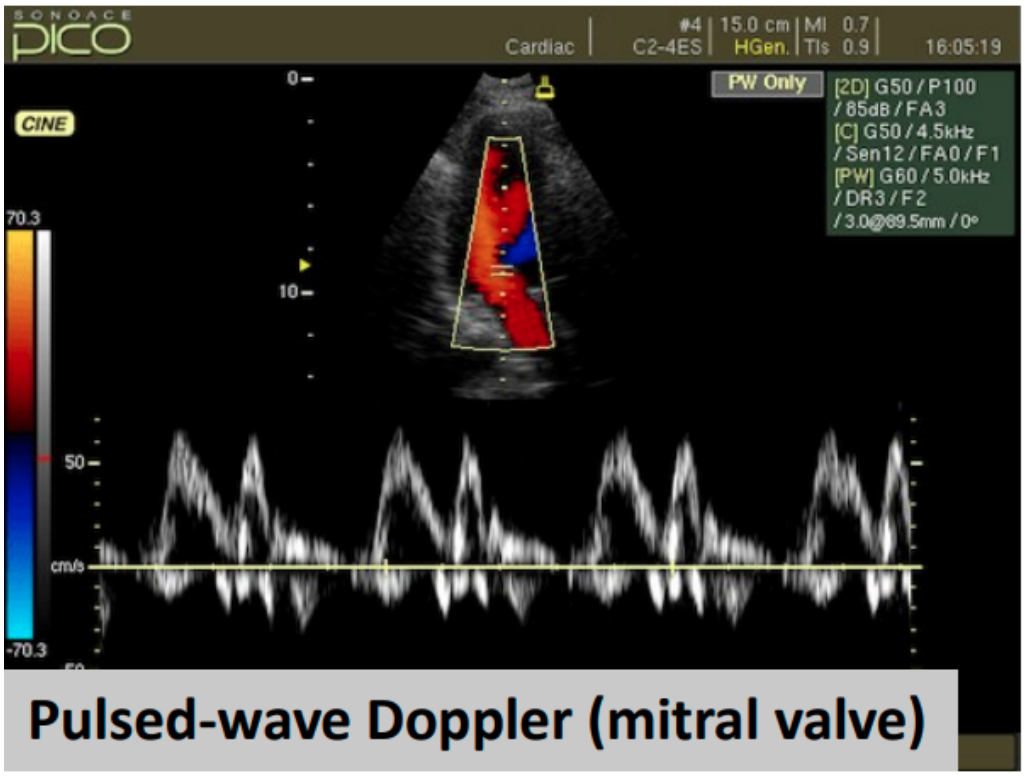

Figure 2.20: Illustration of a pulsed wave Doppler used to assess velocities around the mitral valve. This figure is reprinted from [4].

In order to compute Doppler velocities, a technique based on the auto-correlation of IQ signals is commonly used [41]. The Doppler velocity is computed as follows:

$$V_D = \frac{c\,PRF}{4\pi f_c} \tan^{-1}\left\{\frac{\sum_{i=1}^{N} Q(i)I(i-1) - I(i)Q(i-1)}{\sum_{i=1}^{N} I(i)I(i-1) + Q(i)Q(i-1)}\right\} \quad , \tag{2.29}$$

where c is the speed of sound, PRF is the pulse repetition frequency, f_c is the central frequency of the transmitter, I is the real part of the IQ signal and Q is the imaginary part. In 1995, Loupas et al. introduced a technique based on 2D auto-correlation [42]. The 1D auto-correlator uses an estimation of the mean Doppler frequency. In 2D, it uses, in addition, the estimation of the mean RF frequency. In this way, both slow-time ("temporal") and fast-time ("depth") information are used. Since the average RF frequency can vary greatly, a more accurate estimate of the velocities is thus possible. The 2D auto-correlator is defined by [42] :

$$V_{2D} = \frac{c}{2} \times \frac{\frac{1}{2\pi T_s}\tan^{-1}\left[\frac{Im(R(0,1))}{Re(R(0,1))}\right]}{\frac{1}{2\pi t_s}\tan^{-1}\left[\frac{Im(R(0,1))}{Re(R(0,1))}\right]} \tag{2.30}$$

where T_s is the pulse repetition period ($T_s = 1/PRF$) and t_s is the interval between

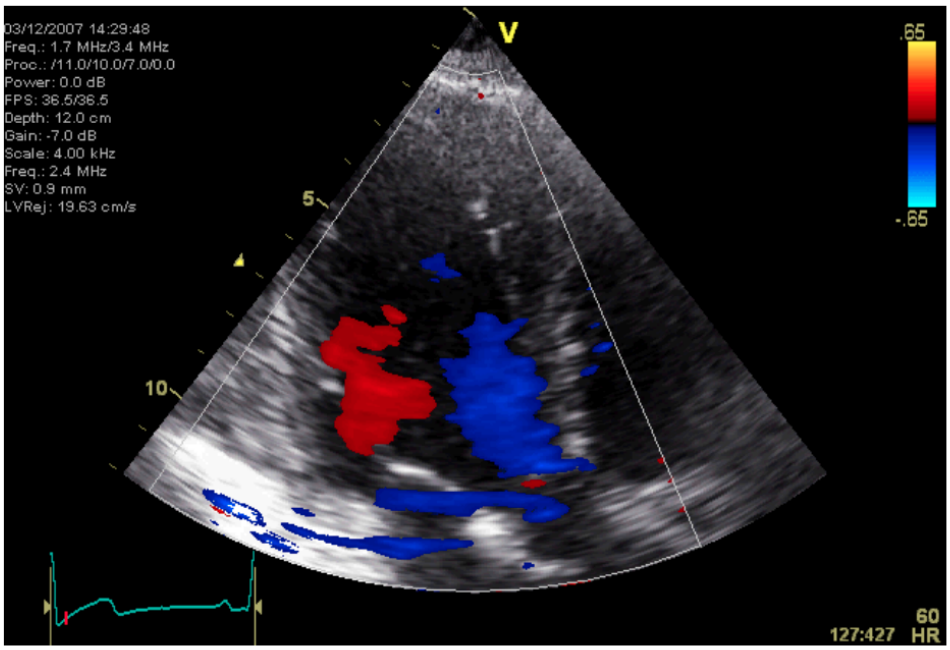

Figure 2.21: Illustration of a clinical 3-chamber duplex ultrasound (B-mode and color Doppler) acquisition. This figure is reprinted from [4].

samples in depth (fast-time). Equation (2.30) can thus be transformed as [42] :

$$V_{2D} = \frac{c \times PRF}{4\pi f_c} \tan^{-1} \frac{\sum_{m=0}^{M-1} \sum_{n=0}^{N-2} [Q(m,n)I(m,n+1) - I(m,n)Q(m,n+1)]}{\sum_{m=0}^{M-1} \sum_{n=0}^{N-2} [I(m,n)I(m,n+1) + Q(m,n)Q(m,n+1)]}. \tag{2.31}$$

Pulsed Doppler and color Doppler are not interchangeable for estimating speed peaks. Pulsed Doppler is more accurate in terms of speed estimation, while color Doppler remains more suitable for visualization. However, both can be used in a complementary way to evaluate the velocity profile or the sequence of events [43].

Chapter 3

State-of-the-art methods

Contents

In this chapter, I present the state-of-the-art methods around the key topics of my thesis, *i.e.*, the estimation of intraventricular flow, the ultrasound simulators, and the ultrasound simulation pipelines

3.1 Intraventricular flow motion estimation

The targeted goal beyond my PhD is the automatic estimation of intraventricular flow on the entire left ventricle cavity. Indeed, color Doppler imaging is a widely used imaging technique to assess blood flow visually in clinical routines. However, this technique estimates the projection of the actual velocity vectors along the ultrasound beams, thus providing incomplete one-dimensional information of the actual blood velocity field. In order to address this issue, several methods have been recently proposed to estimate blood vector fields either by developing a new acquisition technique or by combining Doppler estimation with hemodynamic constraints. In my thesis, I will only consider the second group of methods since the underlying approaches allow to derive 2D blood flows directly from conventional Doppler acquisitions. Garcia *et al.* proposed a series of methods for the estimation of 2D intraventricular flows among the most successful. Each model proposes an axis of improvement in order to obtain an increasingly accurate flow estimator, the last developed method being the one we have chosen in the final version of our simulation pipeline given in chapter 5. I will therefore present in the following paragraphs these state-of-the-art methods and discuss their respective limitations.

3.1.1 2D intraventricular flow mapping with physical restriction

In [9], Garcia *et al.* first proposed a two-dimensional intraventricular flow mapping by digital processing of conventional color-doppler echocardiography images. The main idea concerns the computation of the angular velocity components from the radial (Doppler) velocities under the restriction of a 2D continuity equation across the scanlines. The continuity property of fluids implies the following relation:

$$\frac{\partial \rho}{\partial t} + \nabla \cdot (\rho \vec{v}) = 0 \quad . \tag{3.1}$$

In this expression, ρ is the fluid density, t is the time, $\vec{v}$ is the flow velocity vector field.

In particular, intraventricular blood flow can be considered as incompressible during the cardiac cycle, the fluid density ρ is therefore a constant, spatially and temporally. The continuity property of fluids then implies the following relation:

$$\nabla \cdot \vec{v} = 0. \tag{3.2}$$

This expression indicates that the divergence of the flow is null over the full left ventricle cavity. In order to explicitly expressed the measured Doppler velocities, the authors proposed to formulate equation 3.2 into the polar coordinate system (r, θ), leading to the following equation:

$$\frac{1}{r} \cdot \left(\frac{\partial (r \rho v_r)}{\partial r} + \frac{\partial (\rho v_\theta)}{\partial \theta}\right) = 0. \tag{3.3}$$

This expression can be further expanded as:

$$\partial_\theta V_\theta(r,\theta) = -r \cdot \partial_r V_r(r,\theta) - V_r(r,\theta). \tag{3.4}$$

Equation 3.4 therefore provides a relation between the radial and angular velocities of the blood flow under the incompressibility hypothesis. The integration of equation 3.4 along each isoradial line (*i.e.*, for a given r and over the interval $[\theta_{start},\theta_{end}]$) allows the computation of the angular velocities inside the LV cavity. However, this step requires knowledge of the boundary conditions, *i.e.* the location and velocities at the borders of the left ventricle. The final algorithm of this method can be summarized as follows:

1. Acquisition and de-aliasing of Doppler signals;
2. Computation of boundary conditions (*i.e.*, positions and velocities of the left ventricle borders);
3. Computation of radial velocities from the color Doppler images;
4. Computation of the angular component from equation 3.4;
5. Expression of the obtained blood flow into the cartesian coordinate system for display purposes.

The main weakness of this method concerns the discontinuities along the radial direction, which originates from the separate resolution of the continuity equation (3.4) from each isoradial line. To solve this issue, a smoothing procedure was proposed as post-processing. However, the independent processing of each isoradial line can be considered as a methodological limit, motivating the authors to proposed an improved version of their approach.

3.1.2 Intraventricular flow mapping with regularization

To overcome the issue mentioned above, the authors revisited their formalism through a regularized least-squares method with automatic computation of regularization parameters [10]. The vector flow reconstruction problem is now expressed through a quadratic optimization problem. The targeted velocity field is formulated as the minimum of a cost function, containing a Doppler-based objective function and three regularization terms with physical constraints. The corresponding expression is:

$$\begin{aligned} J(\vec{v}) =& J_0(\vec{v}) + \lambda_1 J_1(\vec{v}) + \lambda_2 J_2(\vec{v}) + \lambda_3 J_3(\vec{v}) \\ =& \underbrace{\int_\Omega (v_r - v_D)^2}_{1)\ fit\ to\ the\ Doppler\ data} + \underbrace{\lambda_1 \int_\Omega (r\partial_r v_r + v_r + \partial_\theta v_\theta)^2}_{2)\ null-divergence\ constraint} + \underbrace{\lambda_2 \int_{\partial\Omega} (\vec{v}\cdot\vec{d}_{wall})^2}_{3)\ boundary\ conditions} + \\ & \underbrace{\lambda_3 \sum_{m\in\{r,\theta\}} \int_\Omega (r^2\partial_r^2 v_m)^2 + 2(r\partial_{r\theta}^2 v_m)^2 + (\partial_\theta^2 v_m)^2}_{4)\ smoothness\ constraint}. \end{aligned} \tag{3.5}$$

Here, $\vec{v}$ is the flow velocity vector, r and θ are the polar coordinates, v_r and v_θ are the polar component of flow velocity, v_D is the acquired Doppler velocity, and $\vec{d}_{wall}$ is a unit normal vector perpendicular to the boundary of the left ventricle. In this formulation, each term is based on a specific assumption:

1. $J_0(\vec{v})$ assumes that the Doppler velocity corresponds to the radial velocity;
2. $J_1(\vec{v})$ expresses the incompressibility constraint discussed in section 3.1.1;
3. $J_2(\vec{v})$ supposes that the blood flows along the interface of the LV (*i.e.* in the normal direction of myocardial wall);
4. $J_3(\vec{v})$ assumes that the spatial change of the velocities is smooth, corresponding to the general physiological hemodynamic properties. A second-order partial derivative with cross terms was used to limit the abrupt changes of the expected velocity field.

This method was named Intraventricular Vector Flow Mapping (iVFM) and was validated on simulations including a patient-specific CFD (Computational Fluid Dynamics) model. The results illustrated the ability of iVFM to estimate adequate intraventricular flows. However, this method is based on the minimization of a cost function which involves a set of parameters whose relative weights influence the quality of the final results. This aspect motivated the authors to revisit their formalism in order to make their method more robust to these intrinsic parameters.

3.1.3 Physics-constrained intraventricular vector flow mapping

Vixège *et al.* proposed an improved version of iVFM [5], in which I analyzed the patients to generate different flow dynamics (some examples of the generated flow will be presented in chapter 5). In order to obtain more accurate velocities and simplify the numerical implementation, the iVFM is now derived from an optimization problem based on two physical constraints with a single regularization parameter. In particular, a new cost function was proposed, consisting in a data attachment term based on the Doppler measurements with two constraints based on fluid dynamics. The minimization problem was formulated as follows:

$$\{\hat{v}_r, \hat{v}_\theta\} = \arg\min_{(v_r, v_\theta)} \underbrace{\left\{ \int_\Omega \omega \left(v_r - v_\mathrm{D}\right)^2 \, \mathrm{d}\Omega \right\}}_{\substack{\text{closely match the} \\ \text{Doppler data}}} \tag{3.6}$$

subjects to the following constraints:

1. $r\,\mathrm{div}(\widehat{\boldsymbol{v}}) = r\frac{\partial \hat{v}_r}{\partial r} + \hat{v}_r + \frac{\partial \hat{v}_\theta}{\partial \theta} = 0 \quad$ on Ω,
2. $(\widehat{\boldsymbol{v}} - \boldsymbol{v}_W) \cdot \boldsymbol{n}_W = (\hat{v}_r - v_{Wr})\, n_{Wr} + (\hat{v}_\theta - v_{W\theta})\, n_{W\theta} = 0 \quad$ on $\partial\Omega$.

The first constraint assumes that the divergence is free (planar mass conservation) while the second constraint supposes that, the normal components of blood velocity and the

myocardial deformation are identical at the left ventricle border (free-slip boundary conditions).

The Lagrange multiplier method was used to solve the minimization problem. Finally, to reinforce the spatial smoothing of the estimated velocity, the problem was formulated through the following regularized least square expression:

$$\widehat{\boldsymbol{x}} = \arg\min_{\boldsymbol{x}} \left\{ \|\boldsymbol{A}\boldsymbol{x} - \boldsymbol{b}\|^2 + \alpha \|\mathcal{S}(\boldsymbol{x})\|^2 \right\} \quad , \tag{3.7}$$

where $\mathcal{S}$ corresponds to a regularization term and α is the unique hyper-parameter term. The optimal solution of equation 3.7 is obtained through the L-curve method, as illustrated in Figure 3.1 From a set of regularization parameter values (α), the method first computes the corresponding $x(\alpha)$ solutions that minimize equation 3.7. These values are then used to compute the evolution of the residual term $\|\boldsymbol{A}\boldsymbol{x}_\alpha - \boldsymbol{b}\|$ as a function of the regularization term $\|\mathcal{S}(\boldsymbol{x}_\alpha)\|$. The regularization parameter that corresponds to the minimum is this function is finally chosen.

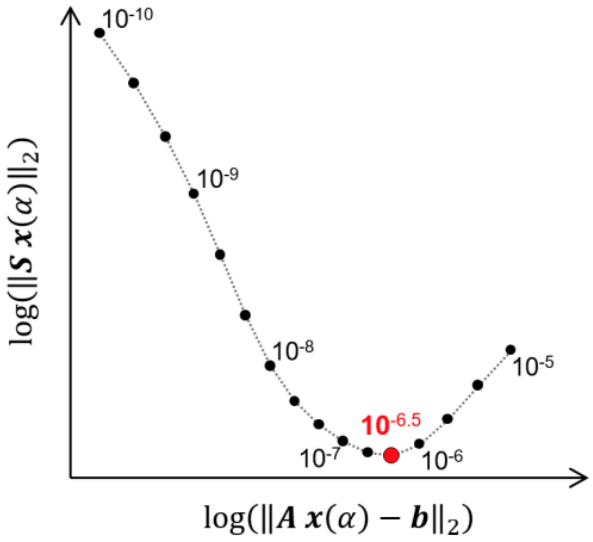

Figure 3.1: Unsupervised selection of the regularization parameter – After fitting the L-curve from a set of regularization parameters (black dots), the regularization parameter that achieves the global minimum (here $10^{-6.5}$) is chosen [5].

Figure 3.2 displays an example of flow estimated using the iVFM method from a simulation based on a CFD model. Results illustrate the capacity of the method to retrieve accurate flow. However, because of the spatial and temporal resolution of the input color Doppler images, the turbulent fluctuation cannot be captured by the method. Moreover, manual segmentation and de-aliasing are still required to automatically apply the iVFM method on clinical data.

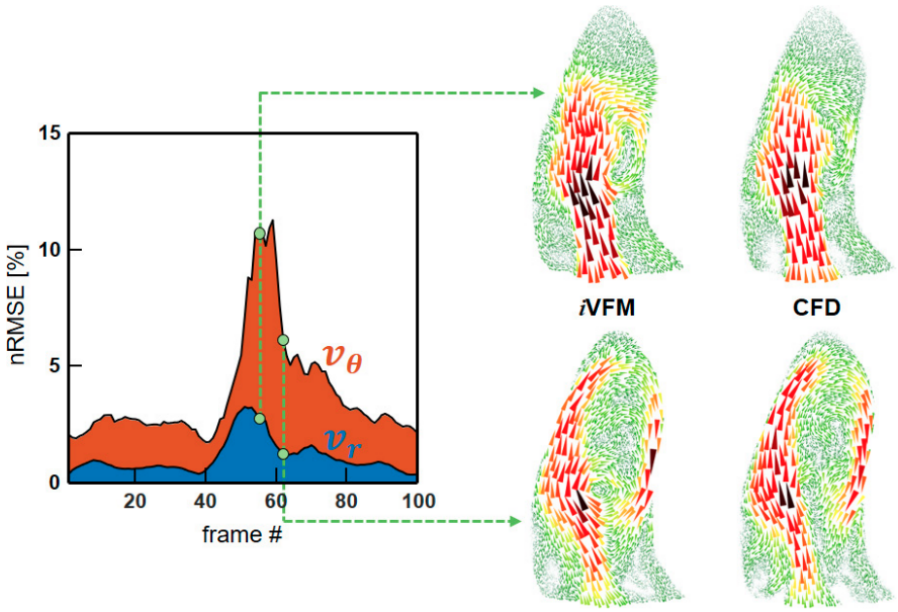

Figure 3.2: This figure is taken from [5]. Normalized root mean square errors between the iVFM-derived and CFD velocity vectors.

3.2 Ultrasound simulators

In the simulation pipeline we developed in chapter 4, we used an ultrasound simulator called SIMUS [44, 45]. Since the quality of our simulation intrinsically relies on the chosen simulator, a brief presentation of SIMUS and the comparison with other popular simulators are provided in the next paragraphs.

3.2.1 SIMUS

The main idea behind SIMUS is to: *i)* model the acoustic pressure field in the Fourier domain based on the assumption of linearity; *ii)* express the backscattered echoes into RF signals. The scatterers are modeled as monopole sources and do not acoustically interact with each other (single scattering assumption). The following description of SIMUS is a simplified outline of the original framework presented in [44].

3.2.1.1 Acoustic wave equation

Under the linearity assumption, the 2D acoustic wave equation is defined as:

$$\frac{\partial^2 p}{\partial x^2} + \frac{\partial^2 p}{\partial y^2} + \frac{\partial^2 p}{\partial z^2} = \frac{1}{c^2}\frac{\partial^2 p}{\partial t^2} \quad , \tag{3.8}$$

where c is the wave propagation speed inside the medium and p is the acoustic pressure at position (x, y, z) and time t.

3.2.1.2 Pressure field

The pressure field is modeled as the one emitted from a piston vibrating with a uniform velocity along the z-axis within a baffle. In this context, the pressure field in the far-field generated by each element can be expressed as:

$$P(\boldsymbol{x},\omega,t) \approx \underbrace{\left\{\frac{kb}{i\pi}\rho c v_0(\omega)\right\}}_{P_{\mathrm{Tx}}(\omega)} \frac{e^{ikr}}{r} e^{-i\omega t} \underbrace{\mathrm{sinc}(kb\sin\theta)}_{D(\theta,k)} \delta(y,r,k) \quad , \tag{3.9}$$

where ω is the angular frequency, $k = \omega/c$ is the wave number, b is half of the size of the element, ρ is the medium density, c is the speed of sound, and r is the distance to the element. In this expression, the first term in brackets represents the spectrum of the transmit pressure pulse at a given frequency, noted by $P_{Tx}(\omega)$. The terms $\frac{e^{ikr}}{r}e^{-i\omega t}$ corresponds to the propagation of a spherical wave at a frequency $\frac{\omega}{2\pi}$. The sine cardinal term (sinc) represents the directivity of the element, noted by $D(\theta,k)$. The last term $\delta(y,r,k)$ is related to the elevation focus of the probe, which is homogeneous in distance.

For a 1-D probe, the final acoustic field corresponds to the sum of the respective acoustic fields generated by a single sub-element, which can be written as:

$$P(X,\omega,t) = P_{\mathrm{Tx}}(\omega) e^{-i\omega t} \sum_{n=1}^{N} W_n \frac{e^{ikr_n}}{r_n} D(\theta_n,k)\, \delta(Y,r_n,k)\, e^{i\omega\Delta\tau_n} \quad , \tag{3.10}$$

where N is number of elements, W_n is the transmit apodization weight for each element and $e^{i\omega\Delta\tau_n}$ corresponds to the delays applied on each individual element.

3.2.1.3 Backscattered echos

SIMUS makes the assumption that the scatterers in the medium react to the transmitted pressure field as point sources. When meeting an incident wave, these scatterers become individual monopole sources, re-scattering the wave uniformly in all directions. There is no acoustic interaction in the case of single weak scattering. Each scatterer is defined by its reflection coefficient ($\mathcal{R}_s$), which describes how much amplitude of a wave is reflected.

For a medium with S scatterers, the total pressure received by the m^{th} sub-element is computed as:

$$\begin{aligned} P_m^{\mathrm{se}}(\omega,t) \approx & P_{\mathrm{Tx}}(\omega) e^{-i\omega t} \sum_{s=1}^{S} \{\mathcal{R}_s \times \left[\sum_{n=1}^{vN} W_n \frac{e^{ikr_{ns}}}{r_{ns}} D(\theta_{ns},k)\, \delta(Y_s,r_{ns},k)\, e^{i\omega\Delta\tau_n}\right] \\ & \times \frac{e^{ikr_{ms}}}{r_{ms}} D(\theta_{ms},k)\, \delta(Y_s,r_{ms},k)\Big\} \end{aligned} \tag{3.11}$$

3.2.1.4 RF signals

The spectrum of the radiofrequency signal (RF) of the m^{th} sub-element depends on the PSF of the transducer and the received acoustic pressure. Its expression can be roughly determined by the following relation:

$$\mathrm{RF}_m^{\mathrm{se}}(\omega,t) \propto \sqrt{\mathcal{S}_{\mathrm{T}}(\omega)} P_m^{\mathrm{se}}(\omega,t) \quad , \tag{3.12}$$

where $\sqrt{\mathcal{S}_{\mathrm{T}}(\omega)}$ corresponds to the one-way transducer response.

3.2.2 Comparison with other simulators

SIMUS is based on the assumption of linear wave propagation. Its latest version includes the 3D acoustic equation that allows the integration of the elevation focus in the synthetic RF signals. There exists several other Matlab software packages dedicated to ultrasound imaging, among which Field II ([46] [47]) and k-Wave ([48]) are likely the most popular.

J.A. Jensen introduced the Matlab simulator Field II in 1996 [46]. Field II models the acoustic wave propagation in the time domain with homogeneous medium. It is also based on the assumptions of: linearity; scatterers acting as monopole sources and weak scattering.

B.E. Treeby and B.T. Cox introduced the Matlab toolbox k-Wave in 2010 [48]. k-Wave works in the k-space (wavenumber domain). The medium is heterogeneous and is modeled with mesh grid. The acoustic field is calculated at the mesh nodes. For this reason, k-Wave can simulate non-linear propagations in heterogeneous media [49]. Because of high computational time induced by the grid strategy, k-Wave is generally used to model the transmitted waves only.

	SIMUS	Field II	k-Wave
Authors	D. Garcia	J.A. Jensen	B.E. Treeby, B.T. Cox
Language	Matlab	Matlab	Matlab
Domain	frequency domain	time domain	wave-number domain
Linearity	linear	linear	non-linear
Medium	homogeneous	homogeneous	heterogeneous
Numerical method	scatterers	scatterers	mesh grid
Scattering	weak single	weak single	X

Table 3.1: Summary of the different properties of the main ultrasound simulators.

3.3 Ultrasound simulation pipelines

Several works have been proposed in the literature to perform realistic simulations of B-mode sequences in echocardiography. Among the most advanced studies, one can cite the work of Alessandrini *et al.* Their simulation pipeline is divided into two parts: *i)* modeling of the myocardial structure and its motion; *ii)* simulation of realistic B-mode sequences based on the use of real recordings (also called template) and an ultrasound simulator. Since this simulation framework is currently the most advanced in echocardiography, we decided to use it as a starting point to develop our own pipeline to simulate synthetic duplex sequences, as described in chapter 4. To better understand the innovation we brought, I detail in the following the pipeline developed by Alessandrini *et al.* [50, 51].

3.3.1 A pipeline for the generation of realistic 3D synthetic echocardiography sequences

Alessandrini *et al.* proposed in [50] a synthetic 3D cardiac simulation pipeline which is based on an electromechanical model of the myocardium and an ultrasound simulator named COLE [52]. This simulator is based on an efficient implementation of 3D convolution with a spatially varying PSF. The PSF that they used in their simulation was generated from FIELD II [46].

A 3D ultrasound clinical sequence (referred to as template sequence in the following) was used to provide the speckle information and define the ventricular geometries. The myocardium was first segmented on the full template sequence to compute a sequence of volumetric tetrahedral meshes. An electromechanical model generated synthetic myocardial motions of healthy/pathological cases with different configurations [50]. A spatio-temporal alignment was then performed to fit the simulated motion with the template recordings. Temporal synchronization was achieved by linearly stretching/shrinking the time axis of the template to match the selected temporal landmarks. Spatial alignment was achieved by matching the myocardium position of simulated motion and template frame at the corresponding time. A 3D cloud of scatterers was defined to reproduce the tissue echogenicity. Each scatterer belonging to the myocardium moved according to the electromechanical model, with a scattering amplitude sampled from the template. By doing so, the simulation framework can generate realistic cardiac motion and speckle texture. COLE was finally used to efficiently convolve the 3D scatter maps with a simulated PSF of an ultrasound system to simulate realistic 3D B-mode volumes. The image quality was investigated by visual assessment of experts during a blind test. Quantitatively speaking, the realism of the synthetic sequence was validated by the measurement of classical features of ultrasound images, such as the intensity distribution, the first order speckle statistics, and the speckle decorrelation over time.

3.3.2 A pipeline for the generation of realistic 2D synthetic echocardiography sequences

Even if 3D speckle tracking seems naturally more appreciated for estimating functional indices, 2D speckle tracking is currently preferred in the clinical routine because of better image quality of 2D acquisitions compared to 3D ones. Based on this finding, the same authors proposed to adapt their simulation pipeline to the generation of realistic 2D sequences. In particular, 2D ultrasound template sequences with different views were acquired from seven vendors to provide speckle information and heart geometry. For motion estimation, additional 3D ultrasound sequences were acquired to provide a 3D ventricular shape to personalize the EM model. Tetrahedral mesh sequences of healthy and pathological motions were simulated by adjusting the contractility and stiffness of the model. In order to register the simulated 3D motion into the 2D template sequences, a 2D plan was sliced at the corresponding apical view on the 3D template. Segmentation of the myocardium was then performed on both the 3D and 2D template sequences to align them by a spatio-temporal registration applied for each frame of the sequence. Thanks to this strategy, the tetrahedral mesh sequence of the EM model can be registered to the

2D template sequence to move scatterers in the myocardial region with a realistic reflection coefficient sampled from real recordings. 3D scatterers were defined in a volume centered on the 2D apical view plan with a thickness along the elevation direction. As in their previous work, COLE was used to simulate 2D+t ultrasound sequences from the set of scatterers efficiently. A different PSF was generated for each vendor in relation to the corresponding probe properties (*e.g.*, beam density, central frequency, sampling frequency, etc.). Thanks to this pipeline, the authors generated an open-access dataset composed of 2D apical two-three-four chamber view sequences for seven vendors and five different motion patterns, including one healthy and four pathologies. That resulted in a dataset of 105 B-mode sequences with corresponding myocardial displacement fields. However, this approach relies on a personalization procedure which remains tedious and currently limits the deployment of such scheme to small datasets. For instance, concerning the datasets where the number of patients is lower than 10 with the same kind of heart motion, the synthetic myocardial deformation remains relatively insufficient compared to the reported normality ranges (*e.g.*, the simulated peak systolic longitudinal strain is lower than 10% for this kind of datasets, instead of 20% in real cases).

Chapter 4

Contribution 1: A duplex simulation pipeline

Contents

4.1 Introduction

4.1.1 Clinical background

Doppler echocardiography is the clinical imaging modality of choice for flow analysis in the cardiac chambers. As detailed in chapter 2, several Doppler techniques can be used to assess velocities in ultrasound imaging: *i)* Continuous-wave Doppler (CWD) to estimate a wide range of velocities along a predefined ultrasound line; *ii)* Pulsed-wave Doppler (PWD) to estimate velocities within a small spatial volume; *iii)* Color Doppler Imaging (CDI) to estimate velocities over a large scan area. Spectral Doppler (CWD and PWD) is used to locally estimate blood velocity in specific situations, such as in the assessment of aortic stenosis severity [53]. In contrast, CDI is generally used as a visualization modality to display simultaneously the myocardium and intracavitary flow, although at a relatively low frame rate.

CDI is subject to several sources of errors, the main ones being aliasing artifacts and clutter noise. Aliasing occurs when the velocities to be measured exceed the Nyquist limit, the value of which is determined by the pulse repetition frequency and the maximum depth [54]. In the classic red-blue Doppler color map, when aliased, color-encoded velocities wrap around such that color information turns from red to blue or vice versa [55]. Clutter corresponds to different sources of noise that mainly affect the low-frequency content of the slow-time signals. In echocardiography, clutter is mostly due to the motion of high reflective tissues that surround the blood cavity. Therefore, blood signals must be separated from clutter before flow estimation.

4.1.2 Motivation

For this purpose, many approaches have been proposed to remove aliasing [6, 56] and reduce clutter noise [57, 58]. Those techniques are mostly based on standard signal and image processing, which may lead to inherent difficulties in ambiguous and non trivial situations [59]. A recent study reports a DL solution to address the problem of aliasing removal [59]. The proposed method involved a conventional U-Net architecture [60] to localize aliased and double-aliased regions based on information derived from I/Q signals (*i.e.*Doppler frequency, power, and bandwidth, speckle flow angle, and speckle flow speed). Once detected, the aliased regions were corrected using a phase unwrapping algorithm [6]. Since the input of the U-Net method uses physical information, it was necessary to apply a clutter filter at the beginning of the workflow. These results illustrate DL's capacity to segment regions with single and even double aliasing. Combined with classical signal processing tools, the proposed pipeline demonstrated its ability to improve the quality of flow visualization by CDI.

Besides the application to eliminate the clutter noise, DL methods have revolutionized several fields of application in ultrasound imaging, the main ones being related to classification (*e.g.* automatic view recognition [13]) and segmentation (*e.g.* automatic extraction of clinical indices [14]). In light of these successes, one may wonder why no additional work has been done so far to improve CDI. One of the main reasons is probably the difficulty to access referenced datasets, *i.e.* data whose flows are known and which can be used as a reference for learning algorithms. In this context, realistic ultrasound

simulations can play a key role in building such datasets. In this regard, a recent pilot study has shown that DL techniques can learn from synthetic ultrasound sequences to improve a targeted task, in this case, the estimation of rotational movements on *in-vitro* data [61].

Computational ultrasound imaging has been applied for the analysis of the myocardial motion from B-mode sequences [50, 62–65]. Most of the studies involved an electromechanical (E/M) model to generate ground-truth myocardial deformation fields. The E/M model has the advantage of relating cardiac contraction to its biophysical causes, allowing a realistic incorporation of physiological and pathological conditions [66]. Prakosa *et al.* first proposed a warping-based method where a real B-mode sequence was registered to the E/M simulations [62]. Although the resulting images showed realistic textures, warping artifacts degraded the quality of the synthetic images. To reduce warping artifacts, De Craene *et al.* [63] used the ultrasound simulator FieldII to generate ultrasound images [67]. However, the scatterers were too simplistic, yielding unrealistic binary-like synthetic ultrasound images. To solve this issue, Alessandrini *et al.* combined the E/M model, the COLE ultrasound simulator and the B-mode template images into a unified pipeline [50] (more details are provided in section 3.3.1). Their simulation pipeline combined the advantages of both [62] and [50] and was able to produce realistic synthetic images. However, the backscattering transition between the myocardium and the surrounding environment was not sufficiently controlled, reducing the degree of realism of the simulated sequences. To solve this issue, the authors of two recent studies ([64] and [51]) introduced different strategies to ensure a smoother transition between the myocardium and the blood pool, leading to very realistic B-mode echocardiographic imaging simulations (both 2D and 3D). The use of the E/M model remains, however, the Achilles heel if a wide spectrum of simulations is required.

4.1.3 Main contributions

In comparison with the literature, the main novelties introduced in this work are:

- the development of the first simulation pipeline for the generation of realistic duplex ultrasound sequences, *i.e.* the simulation of both B-mode and Doppler images.
- the integration into our simulation of a patient-specific CFD model to generate ground-truth blood vector fields.
- the introduction of controlled clutter noise thanks to simple modeling of myocardial movement.
- the assessment of the validity of our pipeline through the simulation of different synthetic duplex sequences.

4.2 Methodology

Figure 4.1 provides the flowchart of the color Doppler simulation pipeline. The following sections describe the content of each block. Clinical apical long-axis 3-chamber B-mode

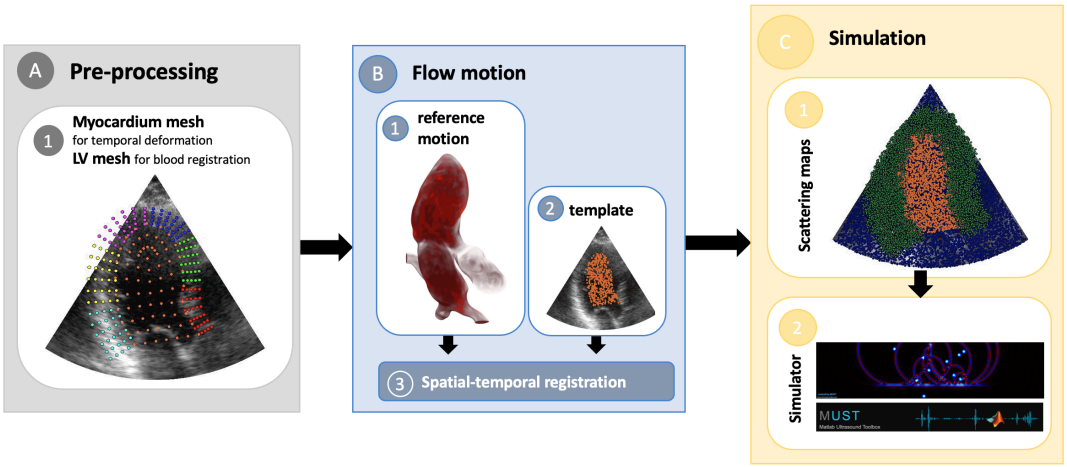

Figure 4.1: Proposed pipeline for the simulation of realistic duplex ultrasound sequences. (A) A clinical recording works as a template for speckle texture, anatomy definition, and myocardial motion estimation; (B) A CFD model controls the synthetic blood flow motion; (C) An ultrasound simulation environment merging information from the template image sequence and the CFD model accounts for the image formation process. In the simulated sequence, the blood flow is fully controlled by the CFD model while the visual appearance is very similar to the one of a real acquisition. Each block specifies the section number where the description is detailed.

recordings (called "template" in the following) are used to simulate sequences with realistic tissue texture. The first step of the simulation pipeline is to segment the endocardium on the template cineloop. Two regions of interest (ROIs) are obtained: the intraventricular cavity, and the left ventricular myocardium. Time-varying surface meshes are generated for each of these ROIs (block A in Figure 4.1). Using these echo-derived meshes, a CFD intracardiac flow is anchored to the intracavity ROI of the template cineloop by registration. It provides us a ground-truth sequence of intracardiac blood motion (block B). This reference motion is then used to displace blood point-scatterers, inside the left ventricle, from one simulated frame to the next (block C). The myocardial meshes are used to move the myocardial scatterers to produce realistic B-mode images and clutter in the Doppler signals. An ultrasound open-source simulator is finally run on the blood+myocardium scatterer maps to generate synthetic ultrasound signals. These signals are post-processed with conventional beamforming algorithms to construct duplex ultrasound cineloops.

4.2.1 Pre-processing

4.2.1.1 Template image sequences

A clinical 2-D ultrasound acquisition was used as a template sequence to define the geometry and provide the texture of the simulated ultrasound images. In this work, 2-D sequences (one complete cardiac cycle between two end-diastoles ED1 and ED2) were

acquired from an apical three-chamber view using a GE Vivid e9 ultrasound scanner (GE Healthcare) and a 2.5 MHz phased array. All sequences were acquired in duplex mode to obtain both B-mode and Doppler images over a cardiac cycle. The ultrasound machine settings were adjusted to scan the entire left ventricular cavity and myocardium, from the apex to the base. It returned a pulse repetition frequency of ∼7000, and a frame rate of 16 fps. All the subjects were scanned with nearly identical conditions.

4.2.1.2 Manual segmentation

The template sequences were segmented manually to get contours over the cardiac cycle. In order to ensure temporal coherency, the protocol illustrated in Figure 4.2 was followed. In particular, eight time instants equally divided between ED1/ES and ES/ED2 were first selected. Endocardial and epicardial borders were delineated manually at each instant. Each boundary was then resampled to ensure an even distribution of points along the contours. These points were finally interpolated in time using periodic spline to obtain myocardial and intracavity ROIs over the entire cardiac cycle.

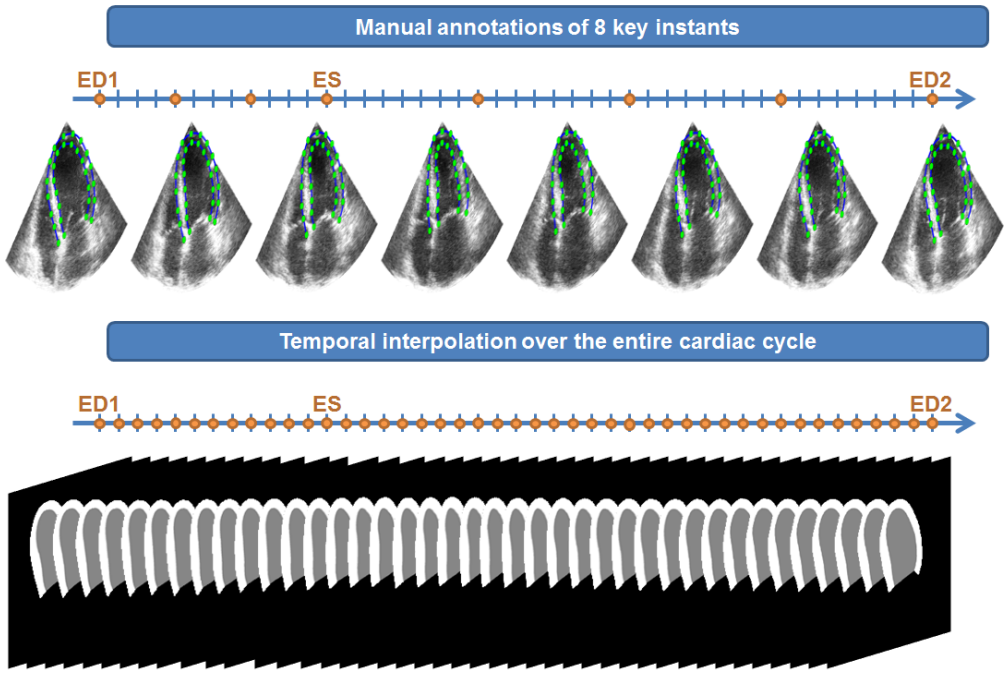

Figure 4.2: Protocol used for manual segmentation of the myocardium over the entire cardiac cycle

4.2.1.3 Myocardial meshes

The left side of Figure 4.3 illustrates the resampling scheme for the myocardial meshes. For each myocardial ROI, the base of the left ventricle was defined by the line linking point #1 (pt1) to point #2 (pt2). We defined the apex as the point of the epicardial contour whose distance from the base was greatest. 36 points were then evenly distributed over

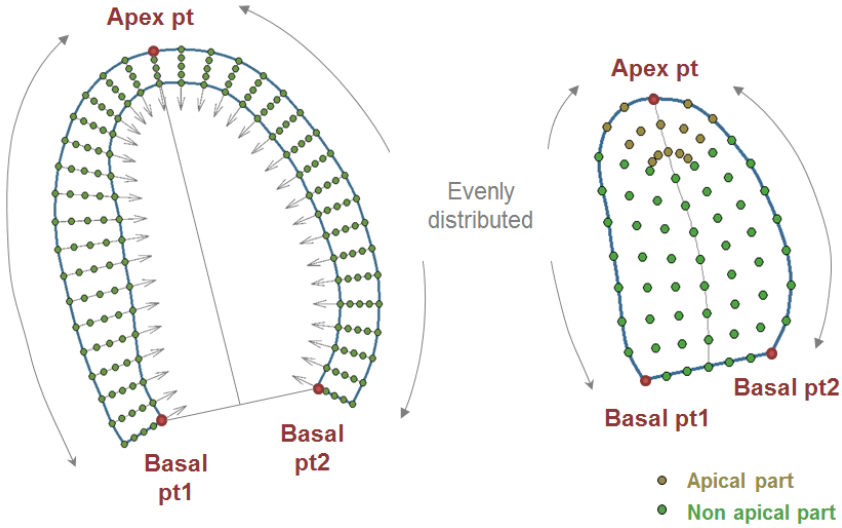

Figure 4.3: Meshing of the segmentation masks for the myocardium (left) and left ventricular cavity (right). The proposed schemes allowed myocardial meshing with 180 points (36 longitudinal x 5 radial) and 280 triangle cells, and intracavitary meshing with 71 points (15 apical + 56 basal) and 114 triangle cells.

the epicardial contour: 18 on the lateral wall, and 18 on the anterior wall. Intramyocardial segments perpendicular to the epicardial contour and passing through the 36 epicardial points were then automatically drawn to join the epicardial and endocardial contours. Each intramyocardial segment contained 5 evenly distributed points. This resampling scheme allowed myocardial meshing with 180 points (36 longitudinal $\times$ 5 radial) and 280 triangle cells. These myocardial meshes were used in section 4.2.3 to compute the myocardial displacements.

4.2.1.4 Left ventricle meshes

The right side of Figure 4.3 illustrates the resampling scheme for the intracavity meshes. As with the myocardial meshes, the basal and apical points were computed automatically from the intracavity ROIs. 21 points were then evenly distributed over the endocardial contour. The basal and apical points were used to define the median axis of the LV intracavitary ROI (see Figure 4.3, right panel, gray curve). Two-thirds of the median axis were sampled uniformly, and the corresponding points (green points along the median axis) were associated with their endocardial counterpart to define linear 4-point segments. The apical region was sampled spherically. This resampling scheme allowed intracavitary meshing with 71 points (15 apical + 56 basal) and 114 triangle cells. These LV intracavitary meshes were used in section 4.2.2 to register a ground-truth blood flow motion on the template sequences.

4.2.2 Blood flow motion

4.2.2.1 CFD model

To incorporate a reference blood-motion field into our simulations, we used a patient-specific heart flow CFD model developed by Chnafa *et al.* [68]. In this CFD model, the cardiac cavities and the wall dynamics were extracted from 4D images acquired by computed tomography. The CFD computation was based on an Arbitrary Lagrangian-Eulerian (ALE) method. The ALE method is a way to couple Eulerian and Lagrangian formulations to solve fluid-structure coupling problems. This realistic CFD model provided complex 3-D flow motion in a complete left heart including the left ventricle, the left atrium, and the aorta inlet. More details on the CFD model can be found in [68–70]. From this model, an apical three-chamber view was reproduced by locating the probe at the apex, with the sector enclosing the mitral inlet and the left ventricular outflow tract (left part in Figure 4.4). In this study, we limited ourselves to planar simulations. Out-of-plane blood motions (in the elevation direction) of the insonified scan-area were not considered since the ultrasound simulations were two-dimensional (see section 4.2.4).

4.2.2.2 Spatio-temporal alignment

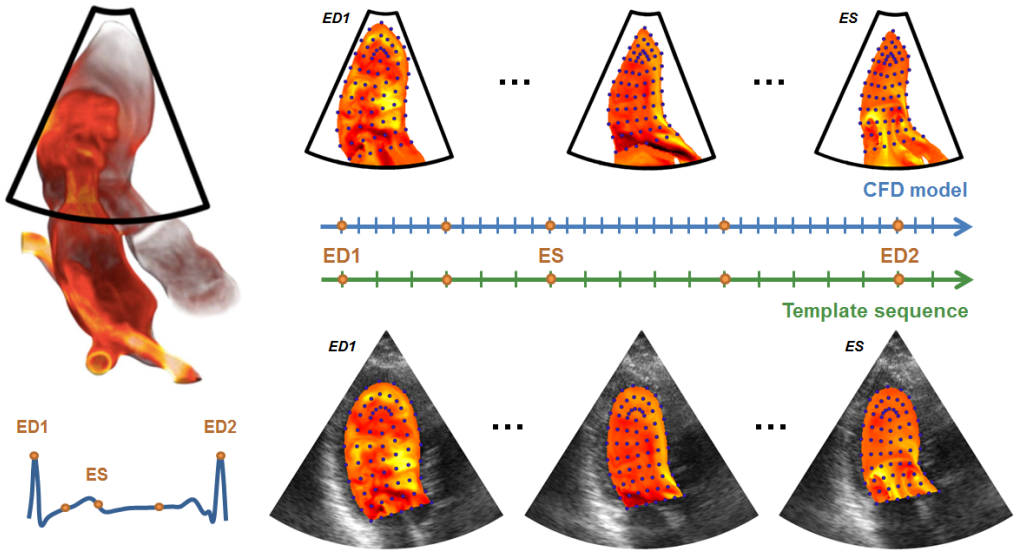

Figure 4.4: Illustration of the spatio-temporal alignment used to register the flow of the CFD model to the template sequence. The color map indicates the amplitude of the velocity along the cross-beam x-direction. The orange markers were used as key instants to perform a piece-wise linear registration between the CFD model and the template sequence. Each point of the CFD meshes was registered to the corresponding template meshes by interpolating the position of the corresponding cell.

Figure 4.4 illustrates the spatio-temporal registration we computed to anchor the CFD intracardiac flow to the template cineloop. We first used a piece-wise linear transformation to match the end-diastole and end-systole times of the CFD model with those of the

template sequence. The orange dots in Figure 4.4 were used as temporal landmarks to perform this temporal registration. Time-varying surface meshes for the intraventricular cavity of the CFD model were then generated using the same procedure as that described in section 4.2.1.4. Each point of the CFD meshes was finally registered to the corresponding template meshes by interpolating the position of the corresponding cell. This procedure was used to spatio-temporally register one blood flow map per emitted beam on the template cineloop. It modified both the amplitudes and directions of the velocity vectors. The mechanical properties of the flow were therefore not totally conserved. For example, the conservation of mass was affected. Our goal here was to obtain realistic Doppler images from an imaging point of view, not from a mechanical point of view.

4.2.3 Myocardial motion

Our simulation pipeline includes the motion of the myocardium to generate synthetic clutter in left ventricular color Doppler. The myocardial motion was not simulated with the electromechanical model that we used in [51]. For each simulation, a set of points was randomly distributed over the myocardial mesh at end-diastole. Each of these points was then propagated over the full sequence by interpolating the displacements of the corresponding cell. This simple procedure allowed us to compute realistic temporal trajectories of any point belonging to the myocardium.

4.2.4 Ultrasound duplex simulation

Our pipeline uses a homemade open-source software called SIMUS from the Matlab ultrasound toolbox (MUST) (www.biomecardio.com/MUST) [71]. SIMUS simulates backscattered ultrasonic signals for linear, phased, and convex arrays, in 2-D or 3-D domain. It allows the simulation of ultrasound images from different transmission schemes (*i.e.* using focused beams, plane waves or diverging waves) by adjusting the transmit delay laws. The latest version of the simulator now integrates 3-D acoustics, which was not the case at the time of this study. Our ultrasound simulations were thus planar. The insonified medium is modeled by monopole point sources that do not interact with each other (weak scattering). From the position and reflection coefficient of each scatterer, SIMUS computes the ultrasound signals that are received back by the probe, as illustrated in block C of Fig.4.1. We used SIMUS to compute the B-mode and Doppler cardiac images (duplex sequences). The same probe settings used to acquire the real B-mode sequence were simulated: a 2.5 MHz 64-element cardiac phased array emitted at a PRF of 7000 Hz. The bandwidths at -6dB were respectively 60% and 20% for the B-mode and Doppler sequences, which corresponded to transmit pulses of 2 and 6 wavelengths. Assuming a heart rate of 60 beats per minute, a focused-beam configuration returned sixteen 11-cm deep B-mode frames interleaved with color Doppler images obtained with packet lengths of 8.

4.2.4.1 Realistic B-mode sequence

The overall strategy for the simulation of the B-mode sequence is illustrated in Fig. 4.5. Each B-mode frame was generated by transmitting 90 focused beams.

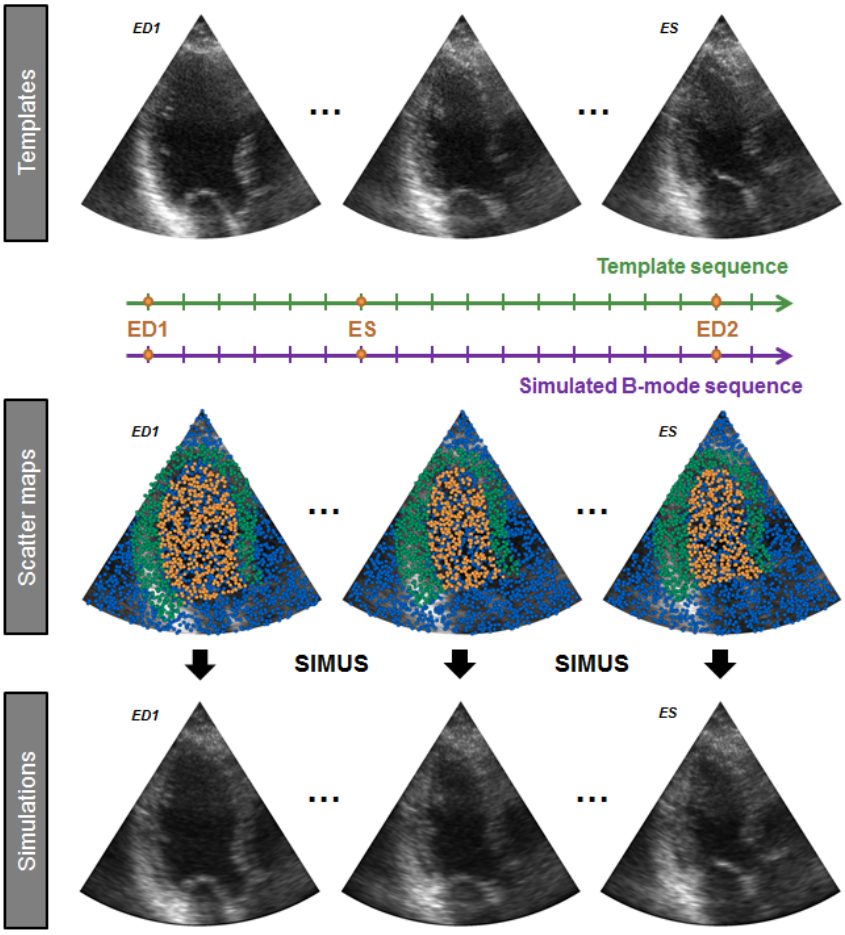

Figure 4.5: Overall strategy for the simulation of B-Mode sequences. Each B-mode frame of the template sequence was used to define a set of scatterers characterized by their positions and reflection coefficients. This information was then provided into the SIMUS ultrasound simulator to generate realistic synthetic images.

Background scatter maps

N_{back} scatterers were randomly distributed in the sector of the first template image. The scatterer density was 10 per square wavelength, which corresponded to $N_{back} \approx 250{,}000$. To avoid flickering effects, the background scatterers were kept motionless. We set the reflection coefficients of the scatterers to generate very realistic images. To mimic the tissue echogenicity of the recorded model, the local intensities I_m of the actual B-mode images were used to calculate the reflection coefficients RC_m of the scatterers, according to the following expression:

$$RC_m = (I_m/255)^{(1/\gamma)} \cdot \mathcal{N}(0,1) \tag{4.1}$$

where $\mathcal{N}(\cdot)$ is the normal distribution, and γ is a constant for gamma compression (set to 0.3).

Myocardial scatter maps

The scatterers of the myocardium were selected on the first simulated frame. The positions of these scatterers were then computed for each B-mode frame of the simulated sequence using the strategy described in section 4.2.3. The reflection coefficients of these scatterers were kept constant to maintain the speckle texture throughout the cardiac cycle.

Blood scatter maps

To simulate realistic Doppler information, additional scatterers dedicated to blood were added in each B-mode frame of the simulated sequence. Thanks to the LV segmentation masks, blood scatterers were randomly positioned inside the left ventricular cavity with a density of 10 scatterers per resolution cell and with RC values following a Gaussian distribution. To mimic the large difference in amplitude between blood and the surrounding tissues, we set a ratio of 70 dB between the RC values of the myocardial scatterers and the blood scatterers RC_m^{blood}. The following expression was used:

$$RC_m^{blood} = \frac{1}{10^{(70/20)}} \cdot \mathcal{N}(0,1) \tag{4.2}$$

Final scatter maps

Inspired by the work proposed in [51], the final scatter maps at each B-mode frame were obtained by combining the background, myocardial and blood scatter maps. All the blood scatterers were kept, while the background and the myocardial scatterers were mixed to ensure smooth transition at the myocardial borders. In particular, smooth version of the myocardial masks were computed to define the probability of keeping/removing a myocardial scatterer and a background scatterer. The probability maps were obtained by decreasing linearly from a value of $p = 0.9$ inside the myocardial masks to a value $p = 0$, with a transition of 7mm. In parallel, each background/myocardial scatterers was assigned a random value ω_m between 0 and 1. Therefore, a myocardial scatterer x_m was removed if $\omega_m > p(x_m)$, while a background scatterer was removed if $\omega_m < p(x_m)$. This

strategy allows the combination of 90% of myocardial scatterers with 10% of background scatterers inside the myocardium regions, with smooth transitions to the surrounding areas.

4.2.4.2 Simulation of the Doppler information

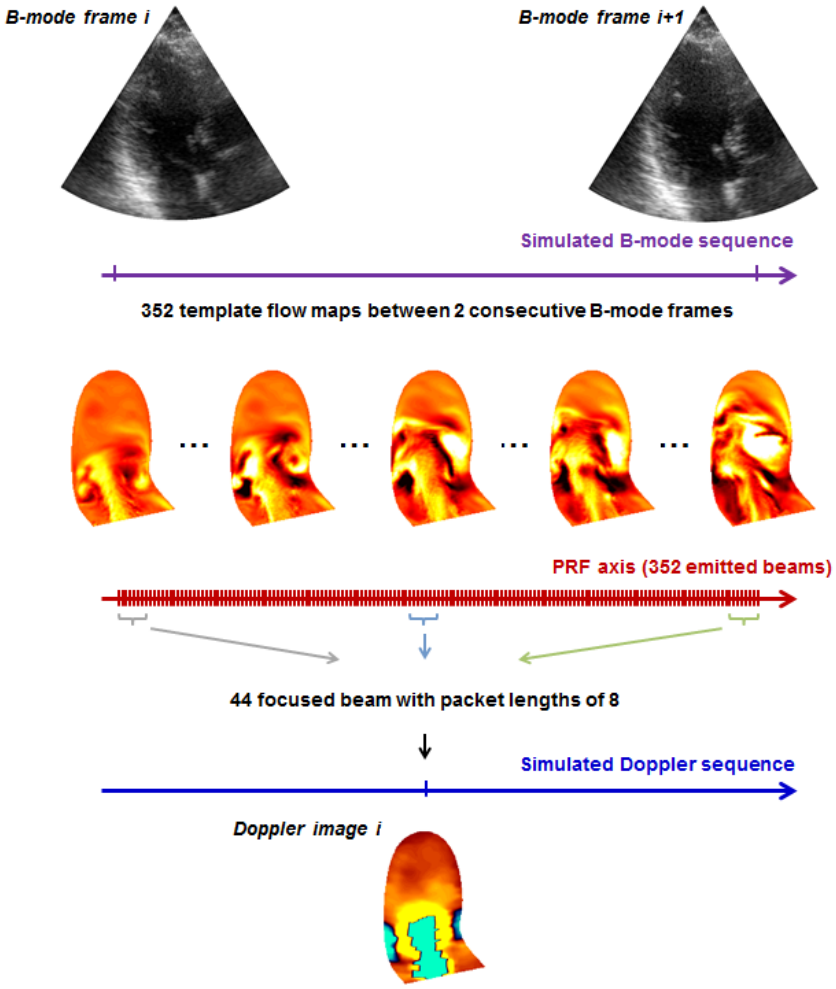

Figure 4.6: Overall strategy for the simulation of Doppler images. 352 registered flow maps were used between each consecutive B-mode frame. This leads to a different map per emitted beam at the PRF frequency. 44 focused beams with a packet length of 8 were used to estimate each color Doppler image.

Figure 4.6 illustrates the scheme we deployed to simulate Doppler images. Blood scatterers were moved between each emitted beam by interpolating their displacements through the template flow maps described in section 4.2.2. Each color Doppler image was generated using 44 focused beams in transmission with packet lengths of 8.

4.2.4.3 Reconstructed synthetic B-mode and Doppler data

The synthetic RF signals generated by SIMUS were demodulated to obtain in-phase/quadrature I/Q signals. The I/Q signals were beamformed using a delay-and-sum to obtain B-mode and color Doppler images [72]. For clutter filtering, we removed the mean of the I/Q signals (= zero-order polynomial-regression filter). The Doppler velocities were deduced by using a lag-1 autocorrelator [73].

4.2.5 Simulated scenarios

Our color Doppler simulation pipeline is flexible enough to generate different types of scenarios. This is interesting in the perspective of generating datasets to feed into DL algorithms to improve the quality of flow visualization and quantification by CDI. To illustrate the relevance of each element of the pipeline, we simulated four scenarios ranging from simplified to realistic situations for five virtual patients. For each simulation, the generated synthetic sequence and the reference motion field are made available to the community, yielding to an open access dataset composed of 20 benchmarked sequences. This synthetic dataset is accessible at the following link: http://humanheart-project.creatis.insa-lyon.fr/duplex.html. The simulation of a full sequence composed by 16 B-mode and color Doppler images took around 4 hours using a C version of the SIMUS code running on an Intel 2 Xeon E5@2.9Ghz with 512GB RAM.

4.2.5.1 Scenario #1: color Doppler "snapshot"

This scenario assumes that one would be able to obtain an instantaneous color Doppler image (color Doppler "snapshot") *1)* in the absence of myocardial motion, and *2)* assuming that the flow is stationary (no temporal acceleration) during the ultrasound emissions generated to obtain this image. The number of emissions to simulate a Doppler image was 352 (44 focused beams with a packet length of 8, as illustrated in Figure 4.6). This prevented *i)* the introduction of clutter noise due to the movement of high-intensity tissues and *ii)* the presence of bias during Doppler estimation caused by blood acceleration. In this snapshot scenario, the estimated Doppler velocities should match the radial velocity components of the CFD-based reference flow.

4.2.5.2 Scenario #2: realistic Doppler simulation of a non-steady-state flow

Blood motion is no longer quasi-stationary: the blood scatterers are relocated between two successive ultrasound transmits. This scenario takes flow acceleration into account, which has side effects on Doppler estimation. The motion of the blood scatterers was computed using the template flow maps described in section 4.2.4.2.

4.2.5.3 Scenario #3: additional synthetic clutter noise

In contrast with the other scenarios, the third scenario aims at simulating color Doppler as obtained in a clinical setting. All the blood and tissue scatterers are relocated between two successive ultrasound transmits. In this context, the information carried by the slow motion of the tissues is mixed with that of the blood flow, which led to wall clutter noise.

4.2.5.4 Scenario #4: focused vs. diverging waves in transmission

Each color Doppler image presented in the previous scenarios was generated using 44 focused beams in transmission with packet lengths of 8. This led to an accurate estimate but at the cost of a small temporal frequency (*e.g.* 16 fps for the simulated sequences). To work at higher imaging rates, recent works proposed to estimate Doppler velocities from diverging waves [74,75]. In these conditions, the whole Doppler sector is insonified with each emitted beam, which drastically increases the frame rate of color flow imaging. However, since this strategy spreads the acoustic energy into a large area, the quality of the Doppler estimate is degraded, especially in situations where high-intensity tissue motion is important. In this context, the goal of this scenario was to investigate the influence of the transmission modes on the quality of estimated velocities. Each sequence was simulated in the "snapshot" conditions with the emission of either focused or diverging beams for the estimation of Doppler information.

4.3 Results

4.3.1 Scenario #1: color Doppler "snapshot"

The second line of Figure 4.7 shows Doppler images simulated in the snapshot scenario for different instants during filling, when blood velocity was the highest. From these results, one can appreciate the reliability of the simulated sequence compared to the corresponding Doppler reference given by the radial velocities. Most of the reference flow patterns were simulated and estimated accurately. The small differences are in large part explained by smoothing effects introduced by the Doppler estimator. The simulated color Doppler images also contained aliasing artifacts when the velocities to be measured exceeded the Nyquist limit (1.1 m/s in our case).

4.3.2 Towards more realistic scenarios

4.3.2.1 Scenario #2: realistic Doppler simulation of an unsteady flow

The third line of Figure 4.7 shows images simulated in such conditions for the same instants as those of the snapshot scenario. The Doppler outputs were slightly different since this scenario does not assume stationary flows. The effect of flow acceleration is more visible during the filling phase.

4.3.2.2 Scenario #3: additional synthetic clutter noise

Because the information conveyed by the motion of the tissues was mixed with that of the blood flow in this scenario, it was necessary to apply a clutter filter on the synthetic I/Q signals (after beamforming) to recover the blood signals. This was realized using a zero-order polynomial-regression filter. The forth line of Figure 4.7 shows images simulated in such conditions. The Doppler outputs were significantly different since this realistic scenario did not provide clutter-free instantaneous maps. The effect of the surrounding

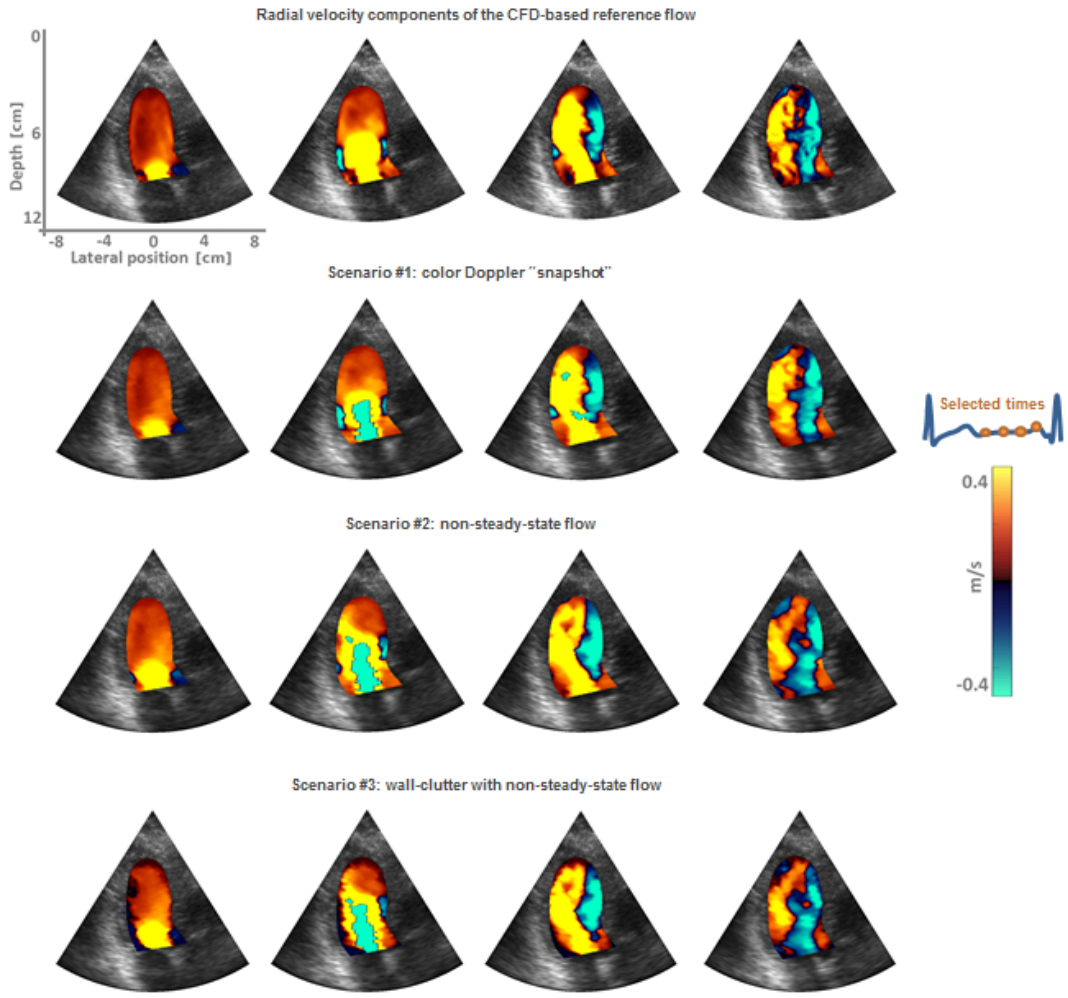

Figure 4.7: Illustration of the ability of our Doppler simulation pipeline to generate three different types of scenarios: 1) a color Doppler "snapshot" situation assuming a stationary flow and the absence of myocardial motion (second row); 2) unsteady flow where the blood scatterers are relocated between two successive ultrasound transmits (third row); 3) wall-clutter with unsteady flow where both the blood and tissue scatterers are relocated between two successive ultrasound transmits (fourth row).

myocardial motion during the filling phase is well visible during filling onset. As tissue velocities decreased during the diastolic phase, clutter noise (along the ventricular wall) reduced until it vanished at the end of filling. This is in line with real observations, which illustrates the realism of the simulation pipeline. In addition, Figure 4.8 shows the Doppler estimates during the systolic phase in the snapshot scenario compared with the wall-clutter scenario. These results further illustrate the impact of tissue motion on Doppler estimation. In this example, Doppler bias appeared along the blood/tissue interface, especially near the septum where tissue motion was most pronounced.

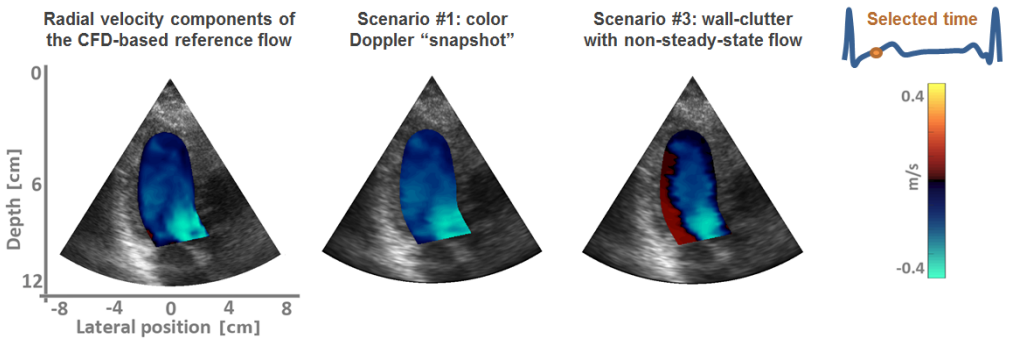

Figure 4.8: Color Doppler snapshot vs. wall-clutter scenarios simulated during systolic phase. Large tissue motions along the septum generate synthetic clutter that degrades the color Doppler image estimated from the synthetic I/Q signals.

4.3.3 Scenario #4: focused vs. diverging waves in transmission

Figure 4.9 displays the results obtained for two instants where the motion of high-intensity tissues was either high (*i.e.* beginning of diastole) or low (*i.e.* diastasis). These results show that the quality of Doppler estimation is related to the amount of tissue motion when diverging waves are used in transmission. Indeed, the clutter phenomenon is more prominent when the motion of high-intensity tissues is important.

4.3.4 Evaluation of a Doppler estimation algorithm

Our simulation pipeline can also be used to provide benchmark datasets to assess the quality of Doppler estimation methods. We evaluated the effect of wall filtering in the presence of myocardium-based clutter by using two different datasets: one generated from scenario #1, and another from the same scenario but with additional wall clutter. Each dataset was composed by 16 Doppler images for 5 virtual patients. In each case, the estimated Doppler velocities were compared with the radial velocity components of the CFD-based reference flow. Figure 4.10 displays the mean correlation plots computed over the five virtual patients. Results show a high agreement between the CFD-based and simulated-derived Doppler velocities for the dataset generated from scenario #1, with a coefficient of determination of 0.92. The small differences can be explained by the smoothing effect of the estimator. The degradation induced by the wall clutter noise can be investigated from the right part of Figure 4.10. In particular, a decrease of 19% of the coefficient of determination can be observed.

4.4 Discussions

4.4.1 On the benefits of training DL methods through simulations

DL techniques have been successfully applied to echocardiography for several years. These methods have allowed major advances in many specific areas such as view classification and segmentation of anatomical structures. Almost all the best performing tech-

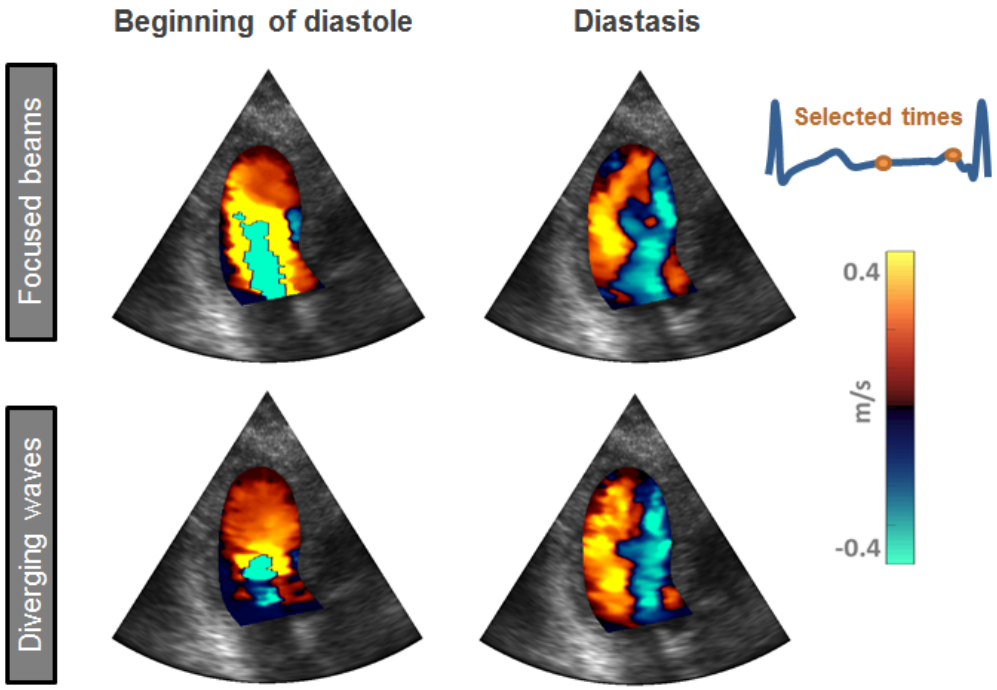

Figure 4.9: Focused vs. diverging beams for the estimation of Doppler velocities. While the diverging wave strategy increases the temporal frequency, the spread of the acoustic energy into a large area degrades the quality of the Doppler estimate, especially in situations where the displacements of high-intensity tissues are significantly large.

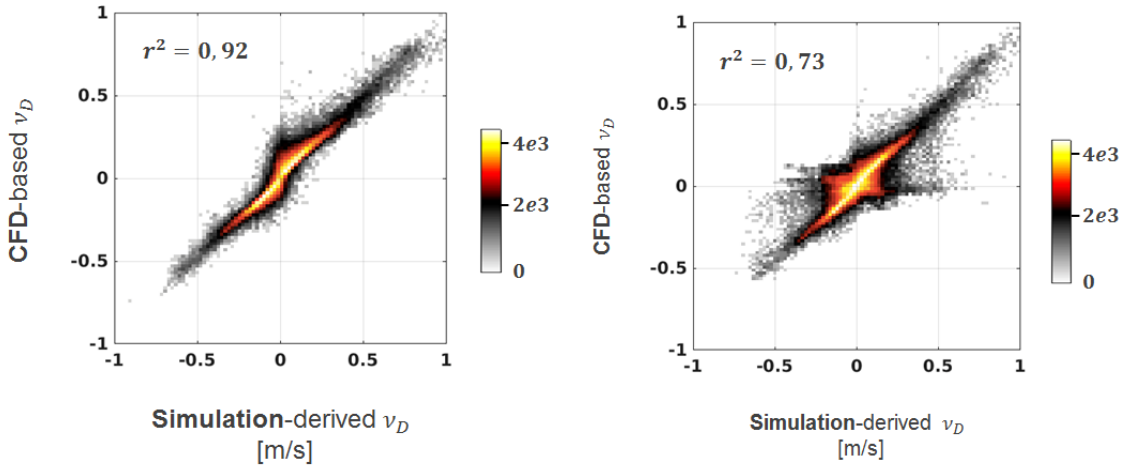

(a) (b)

Figure 4.10: CFD-based vs, simulation-derived Doppler velocities (v_D) for *(a)* the scenario #1 and *(b)* the scenario #1 with additional wall clutter noise. Velocity data from sixteen Doppler images for five different virtual patients.

niques correspond to supervised approaches, requiring the deployment of large-scale datasets with manual annotations. As far as ultrasound motion estimation is concerned, very few referenced data are available, the main one being an open access dataset proposed for myocardial strain benchmarking [51]. A supervised DL network was recently trained on this open-access dataset to automatically estimate myocardial strain [76]. Although the results were very promising, the lack in quantity and diversity of training data did not allow to obtain significantly better scores than the state-of-the-art. Regarding blood flow estimation, there is currently no baseline dataset. Thus creating large-scale synthetic datasets that mimic hundreds or thousands of patients would be the key to train data-driven DL methods for flow estimation. In this context, we proposed the first simulation pipeline that generates realistic duplex ultrasound sequences. Although the size of the derived dataset is not sufficient to train DL models, our framework constitutes the first step toward achieving more complete datasets. A major weakness of our protocol is the need to manually segment the left ventricle and the myocardium throughout the sequence. In the near future, we plan to make this step fully automatic to enhance the scalability of our simulation pipeline, with the goal of creating simulated data that replicates a large number of patients.

4.4.2 An innovative simulation pipeline for duplex sequences

The objective of our study was to simulate realistic B-mode and color Doppler ultrasound images. By "realistic" we mean that these images should resemble those obtained by a cardiologist with a clinical ultrasound machine. As we are interested in studying myocardial and blood motions, this realism must also be reflected in the time scale. It is not just a matter of obtaining a realistic still image, but a realistic cineloop. There is no objective criterion for assessing the degree of realism. Only a visual inspection by an expert eye can judge the realism of the simulations. For the B-mode images, a set of focused waves scanned the cardiac region, and then a standard delay-and-sum technique was used for image construction. Although the transmission/beamforming scheme may differ from those used by clinical ultrasound scanners, the similarity to clinical images is apparent, particularly with respect to speckle patterns. The realism is also found in the color Doppler simulations. Not only is the similarity observed on the Doppler fields, but also on classical artifact phenomena, such as aliasing and wall clutter.

In this study, we focused only on the generation of clutter due to myocardial motion. We neglected other sources of clutter such as those related to rib reverberations, multi-echoes, or twinkling artifacts [77]. Our goal was not to perform a thorough evaluation but rather to show that our pipeline could generate datasets for the evaluation of Doppler estimation techniques. A thorough investigation is beyond the scope of this paper. The evaluation showed that the datasets can lead to accurate estimates of Doppler velocities in the absence of wall-based clutter. In addition, we quantified the decrease in color-Doppler performance when wall clutter was present. This is a direct consequence of the motion of highly reflective tissues that surround the blood cavity. This shows the difficulty in developing techniques that are robust to the clutter phenomenon. We believe that deep learning techniques could help to mitigate wall clutter, based on realistic simulations and appropriately designed references.

4.4.3 Potential improvements

The developed pipeline constitutes a relevant step forward in the field of cardiac ultrasound simulation. Despite a variety of scenarios that can already be provided, it would be interesting to integrate out-of-plane motions into our simulation pipeline. Indeed, the 3D nature of blood flow induces some decorrelation of the slow-time signals which may affect the quality of Doppler estimates. In this study, our goal was to develop the first duplex simulation pipeline by focusing on key properties such as non-steady-state flow and wall clutter. However, the 3D nature of the CFD model we used will allow us in the future to study and quantify the deterioration caused by 3D motion.

Moreover, the ability to perform 3D simulations with the latest version of SIMUS will also allow us to evolve our simulation pipeline in order to preserve the mechanical properties during the registration step described in section 4.2.2.2. To do so, we consider expressing the registration as an optimization problem with a physical constraint that assumes that the divergence is free. As in [5], the corresponding minimization problem can then be solved by the Lagrange multiplier method.

4.4.4 Perspectives

The pipeline was used to generate an open access dataset of 20 synthetic sequences available at the following link: http://humanheart-project.creatis.insa-lyon.fr/duplex.html. Part of these data can already be used to benchmark the quality of Doppler estimation techniques. Our goal is to progressively enrich this dataset with new simulations to cover an exhaustive and diverse range of blood flow dynamics, from healthy to pathological cases. This will provide richer reference datasets that will help improve the quality of flow visualization and quantification by CDI using DL methods. We are targeting three main applications in the near future. Our framework will first be used to estimate alias-free Doppler velocities from the backscattered ultrasonic signals. We have shown that our pipeline can also generate wall clutter noise. Despite a large literature dedicated to this phenomenon, clutter remains one of the main sources of error in intraventricular flow estimation. Our solution therefore offers new perspectives to develop DL-based clutter filters more efficient than the state-of-the-art (such as SVD filters). Finally, it has been shown that it was possible to decipher 2-D velocity vector fields using color Doppler images [9]. This can be used to characterize the vortex that forms in the left heart and investigate the filling capacity of the heart. The underlying method involves several tedious steps, such as segmentation of the left ventricle and aliasing/clutter filtering. We thus plan to investigate the application of DL for the automatic and robust estimation of two-dimensional intraventricular flows.

Chapter 5

Contribution 2 : Improvement of the personalization of our simulation pipeline

Contents

5.1 Introduction

5.1.1 Motivation

In the previous chapter, a patient-specific heart flow CFD model [68] was used and integrated into the proposed duplex simulation pipeline. This CFD model contains complex 3D flow motion in the full cardiac cavity. Unfortunately, there currently exists only one such model simulated from a healthy volunteer. Therefore, we cannot use this model to simulate large-scale datasets. To solve this issue, I propose in this chapter to replace the CFD model with the iVFM algorithm presented in section 3.1.3. This model is based on the incompressibility constraint and allows the derivation of intraventricular flows from standard color Doppler images. By doing so, we make our simulation pipeline easy to be personalized. In this manuscript, the term personalization refers to the adaptation of our simulation pipeline to a given patient, both from a morphological and functional point of view. This modification is thus an essential step for the generation of a large-scale dataset with rich information.

5.1.2 Main contributions

The main contributions proposed in this chapter correspond to:

- the development of a dedicated strategy to allow an efficient personalization of our simulation pipeline.
- the construction of a referenced dataset of ultrasound duplex sequences with a rich variety of intraventricular flow motions and cardiac anatomies.
- the evaluation of the validity and genericity of our pipeline by simulating synthetic duplex sequences with different scenarios.

5.2 Methodology

The key steps of the pipeline remain the same as the ones described in chapter 4. The main difference concerns the computation of the ground truth motion, leading to modifications on the pre-processing and registration steps.

5.2.1 General workflow

The flowchart of the proposed simulation pipeline is provided in Figure 5.1. Based on the pre-processed ultrasound template sequences (block A), the main idea is to use as reference the flow derived from the iVFM method (directly applied on the clinical color Doppler sequence) to compute the motion of the blood flow in the simulation (block C). The difference with the previous chapter is mainly situated in block A and B, which will be detailed in the following sections. The acquisition and pre-processing of the template sequence needed to apply the iVFM technique are first detailed, followed by a description of the computation of the blood flow on the entire cavity thanks to this method.

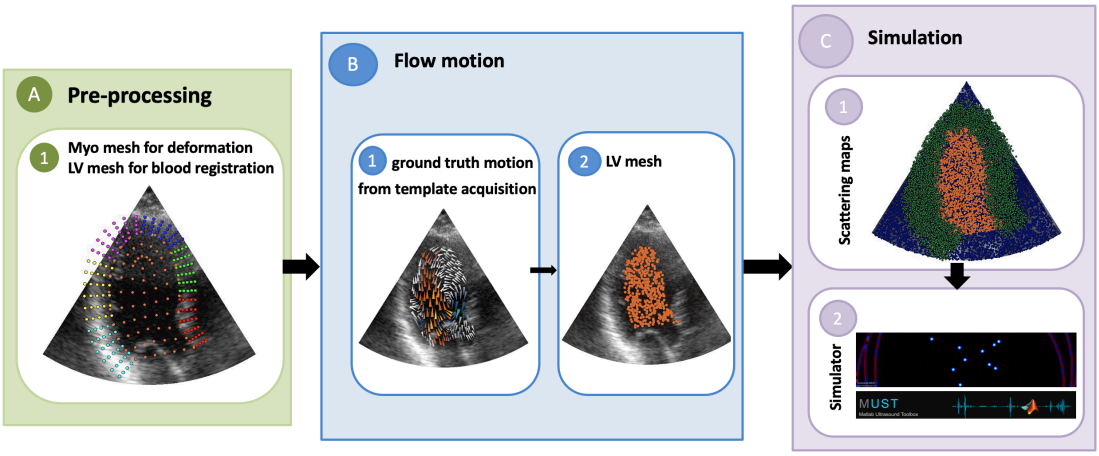

Figure 5.1: Adapted pipeline for the simulation of realistic duplex ultrasound sequences. (A) A clinical recording works as a template for speckle texture, anatomy definition, and myocardial motion estimation; (B) iVFM technique computes the synthetic blood flow motion; (C) An ultrasound simulation environment merging information from the template image sequence and the iVFM-deduced flow reference accounts for the image formation process. In the simulated sequence, the blood flow is controlled by the iVFM technique while the visual appearance is very similar to the one of a real acquisition.

5.2.2 Pre-processing

5.2.2.1 Template acquisitions

We acquired 20 clinical 2-D echocardiography sequences from an apical three-chamber view, using a GE Vivid e55 ultrasound scanner (GE Healthcare) and a 2.5 MHz phased array. All sequences were acquired in duplex mode to obtain both B-mode and Doppler images over a cardiac cycle. The ultrasound machine settings were adjusted to scan the entire left ventricular cavity and myocardium from the apex to the base. All the subjects were examined under nearly identical conditions. In general, each sequence was recorded during more than one cardiac cycle. We only chose one complete cardiac cycle, serving as the template (one entire cardiac cycle between two end-diastole ED1 and ED2 instants). Figure 5.2 provides an example of an ECG corresponding to one of the clinical sequences. In this example, we can observe that the acquisition was performed over five cardiac cycles, and we used the first cycle (green ROI) to perform the pre-processing steps described below. During the acquisition, B-mode images and color Doppler images were taken at the instants marked in blue and red, respectively. In some cases, Doppler information was acquired at a higher frequency than the B-mode images. If so, we selected the color Doppler images that were the closest to the corresponding B-mode instants.

5.2.2.2 Manual annotations

After selecting the cardiac cycle and the corresponding B-mode and Doppler frames, manual annotations (block A.1) of the left ventricle and the myocardium were performed

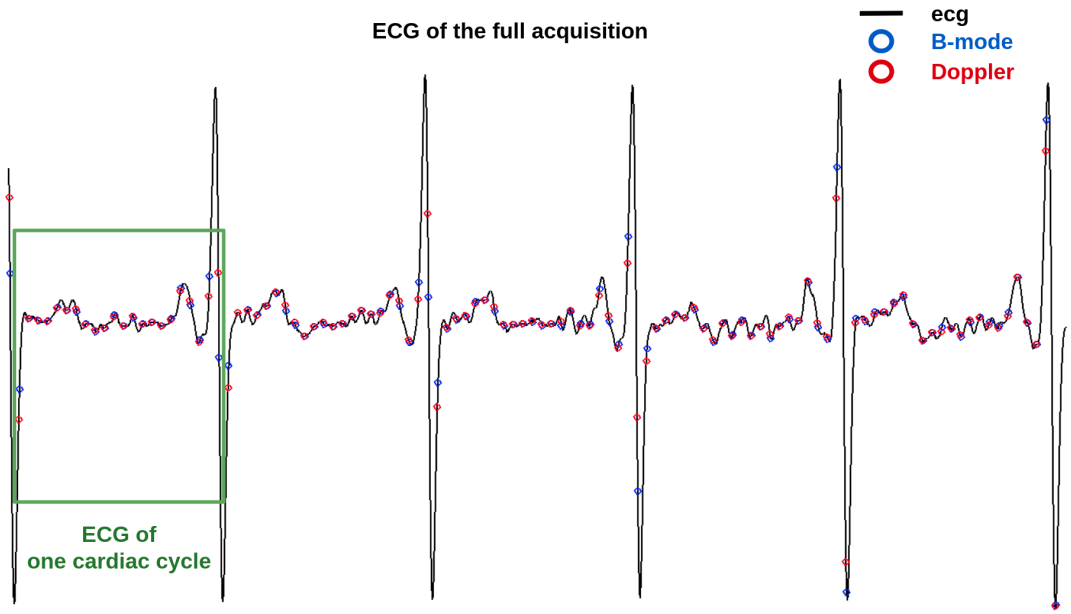

Figure 5.2: Example of the ecg of a specific template sequence from our dataset. The blue dots correspond to the B-mode frames while the red dots correspond to the color Doppler images.

by an expert. 15x2 points were manually drawn to contour both the endocardium and the epicardium, as illustrated in Figure 5.3.a.

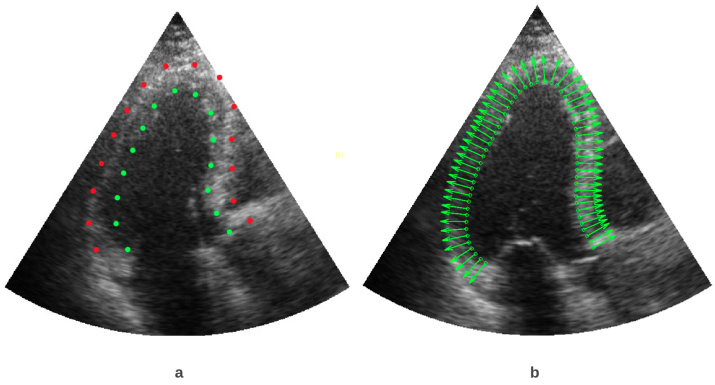

Figure 5.3: (a) Manual annotation of the endocardial (green) and epicardial (red) borders; (b) Normal vectors of left ventricle borders.

5.2.2.3 Pre-processing for myocardial deformation

From the endocardial and epicardial points, the same procedures as the ones described in chapter 4 were applied to compute myocardial meshes over the full sequences (block

A.2). These sequential meshes were used to generate coherent motion of the tissue scatterers surrounding the left ventricle cavity, as illustrated in Figure 5.4. This coherence allows the introduction of synthetic clutter noise on the simulated IQ signals, which reinforces the realism of our simulation.

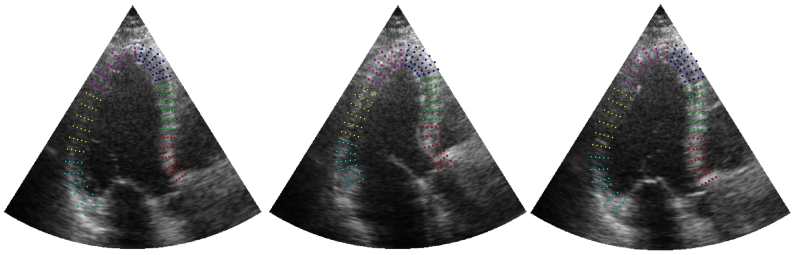

Figure 5.4: Sequential myocardium mesh at 3 key instants in the cardiac cycle (first end of diastole, end of systole, and second end of diastole).

5.2.2.4 Pre-processing for iVFM reference

The following steps are required to apply the iVFM method described in section 3.1.3 on the clinical color Doppler acquisitions:

1. Computation of the boundary conditions:
   The sequences of left ventricle meshes were first used to compute the left ventricle borders and the corresponding normal velocities. The temporal frequencies of the different acquisitions were then used to deduce the corresponding velocities.

2. De-aliasing procedure:

   Before applying the iVFM technique to estimate a 2D vector field from the color Doppler images, it was necessary to remove any aliasing present in the images. This was done by using the de-aliasing and denoising method proposed in [6]. An illustration of this task is given in Figure 5.5.

   This method is based on three main steps:

   a. Segmentation of the color Doppler image by a region growing and merging technique: At first, the image was divided into small regions where the Doppler information is considered as entirely aliased or not-aliased. These connected regions were then evaluated by a predicate (*i.e.*, Hoeffding's probability inequality which assesses statistical properties) to decide whether they should be merged. These procedures were performed iteratively until convergence.
   b. De-aliasing for the corresponding regions: By considering that the blood flow velocity is locally smooth, the adjacent Doppler neighbor regions were compared to determine the aliasing profile and correct it.
   c. Smoothing of the color Doppler image: A robust regularized smoothing technique based on the discrete cosine transform [78] was applied to remove the outliers and the remaining noise in the blood region.

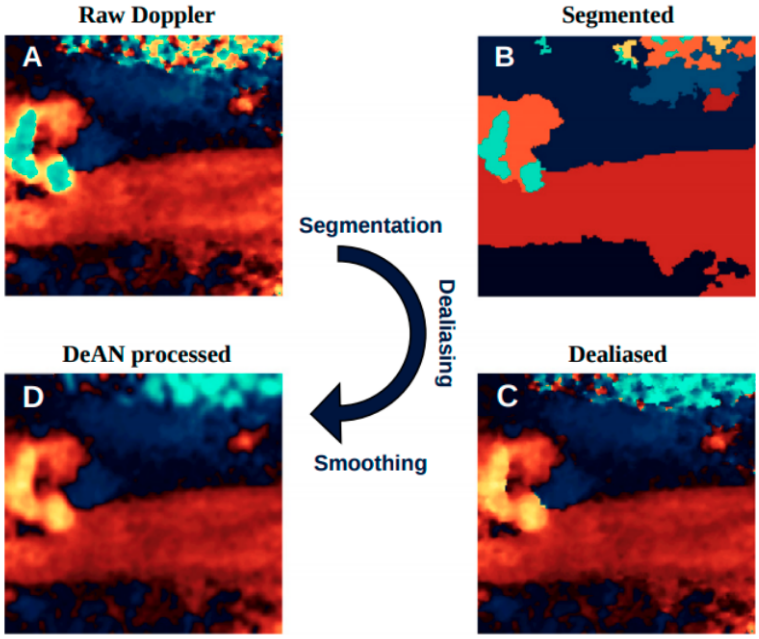

Figure 5.5: Workflow of the de-aliasing technique used to correct the color Doppler images. The three steps of the de-alasing processing : segmentation (from block A to block B), dealiasing (from B to C), and smoothing (from C to D) This figure is adapted from [6].

An illustration of the application of the de-aliasing technique on an image of a patient in our dataset is provided in Figure 5.6.

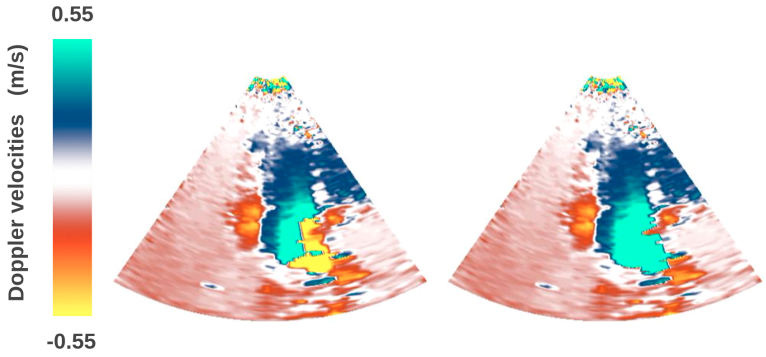

Figure 5.6: Illustration of the de-aliasing procedure used to correct the color Doppler images before applying the iVFM method. The aliasing region appearing in yellow on the left was correctly processed thanks to the de-aliasing technique proposed in [6].

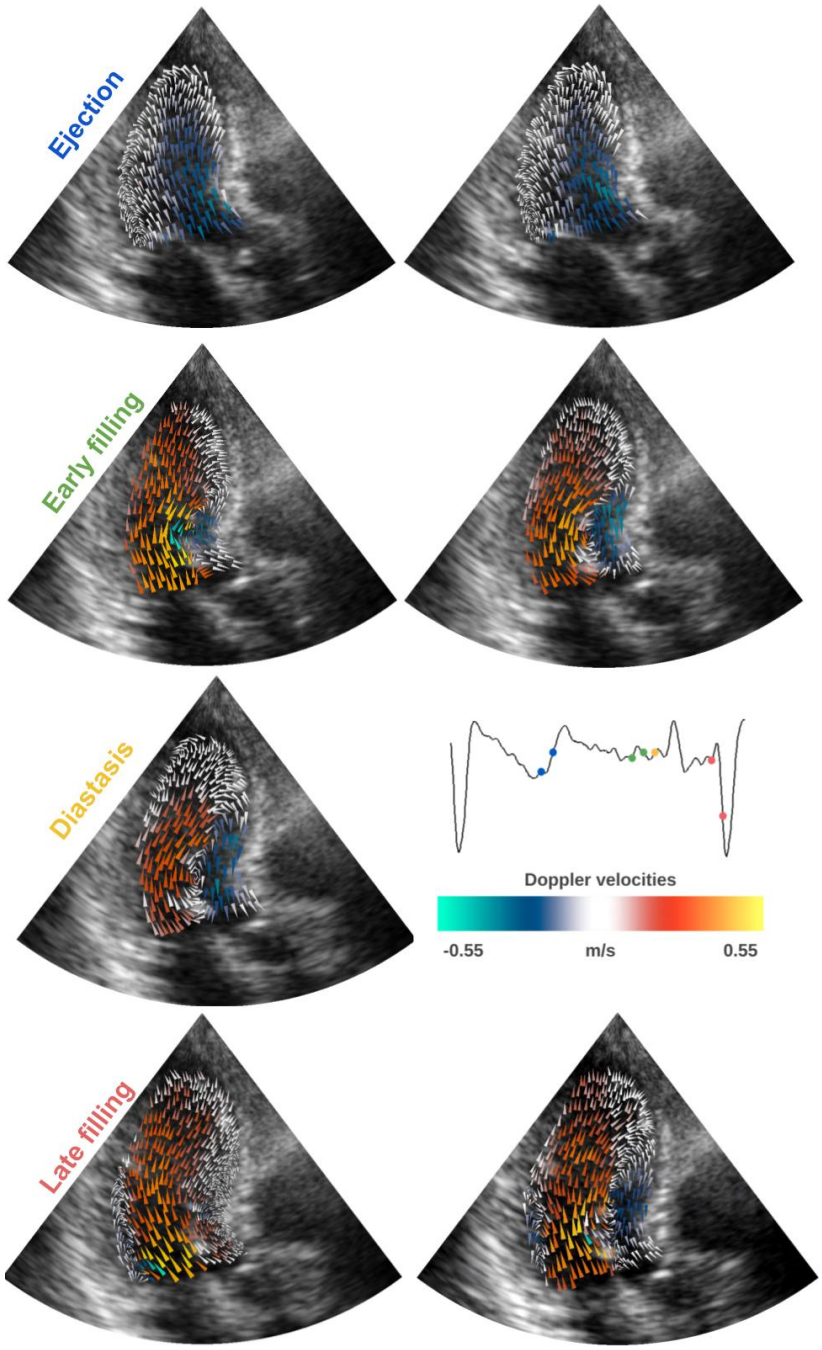

Figure 5.7: iVFM 2D Doppler velocities computed from a template sequence. The figures correspond to the key instants displayed on the ECG.

5.2.2.5 Ground truth motion – iVFM intraventricular flow reference

Figure 5.7 gives an illustration of the intraventricular blood flow computed by the iVFM algorithm at key instants displayed on the ECG. The color of the arrows represents the

original color Doppler fields from which the iVFM fields were calculated. Images in the first row correspond to the instants after the end of diastole when the left ventricle starts to contract and causes ejection. Due to the pressure change from ejection, the mitral valve opens, and the blood starts to fill in the left ventricle (second row). Before the atria contracts, the vortex formed in the early filling is still visible, as shown in the third row. When atrial contracts, the inflow is observed in the fourth row. Since these 2D velocity vectors are computed directly from each template sequence, there is no need to perform any spatio-temporal registration as with our previous solution. To illustrate the effectiveness of our personalization strategy in generating a wide variety of left ventricular shapes and blood flows, we present in Figures 5.8 through 5.10 the iVFM outputs computed from three other template sequences in our dataset. The presentation of these figures is inspired by [5].

5.2.3 Duplex simulation

The same strategy as the one presented in the previous chapter was used to simulate realistic duplex sequences. In particular, we use the SIMUS simulator to generate synthetic B-mode and Doppler cardiac images from a set of scatterers defined by their positions and reflection coefficients. Blood scatterers moved according the iVFM motion field while the myocardial scatterers moved with respect to the sequence of myocardial meshes. The probe settings used in the simulation are the same as the ones used for the real B-mode sequence, i.e., 2.5 MHz 64-element cardiac phased array emitted at PRF of 7000 Hz. Under the assumption that a heart rate of 60 beats per minute, a focused-beam configuration will give sixteen 11-cm deep B-mode frames interleaved with the color Doppler images obtained by a packet size of 8.

5.3 Experiments

We simulated two different scenarios using the 20 patients of our dataset, generating a dataset consisting of 640 synthetic B-mode and color Doppler images with the corresponding reference motion field.

5.3.1 Scenario #1: color Doppler "snapshot"

We first simulated the same "snapshot" scenario as the one described in section 4.3.1. In this scenario, there is no myocardium motion which causes clutter noise, and the flow is assumed stationary without acceleration during the transmission. The estimated Doppler velocities should match the radial velocity components of the iVFM-based reference flow. Figure 5.11 illustrates a simulation obtained from a clinical template acquisition. Each row corresponds to a specific time in the cardiac phase (*i.e.*, ejection, early filling, diastasis, and late filling). The first column displays the radial component of the iVFM reference flow, while the second column shows the B-mode and Color Doppler images generated from the simulation pipeline with scenario #1. From these results, one can appreciate the reliability of the simulated sequence compared to the corresponding Doppler reference. Most of the reference flow patterns were simulated and estimated

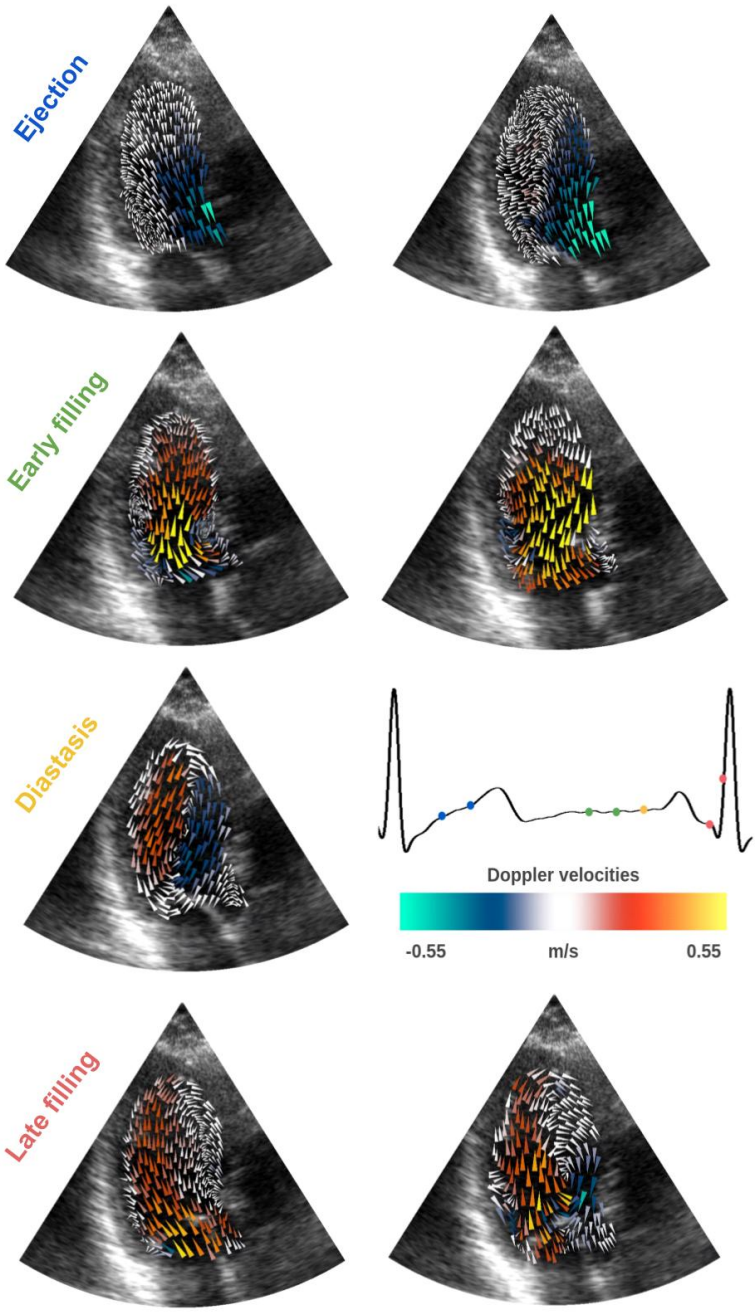

Figure 5.8: iVFM 2D Doppler velocities at the key instants shown on the ECG for virtual patient 1.

accurately. The small differences are in large part explained by smoothing effects introduced by the Doppler estimator. The simulated color Doppler images can also contain aliasing artifacts when the velocities to be measured exceed the Nyquist limit (1.1 m/s in our case).

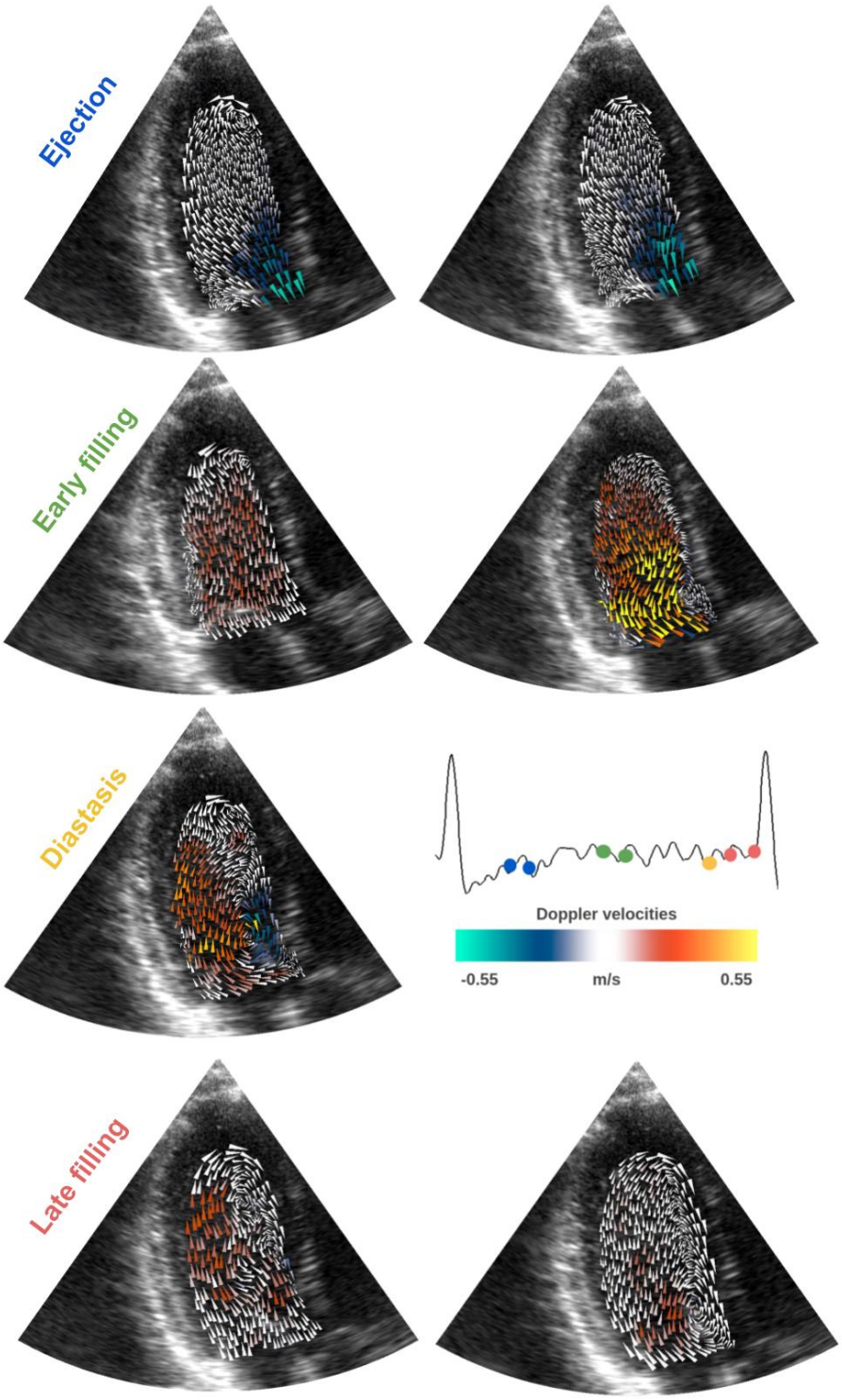

Figure 5.9: iVFM 2D Doppler velocities at the key instants shown on the ECG for virtual patient 2.

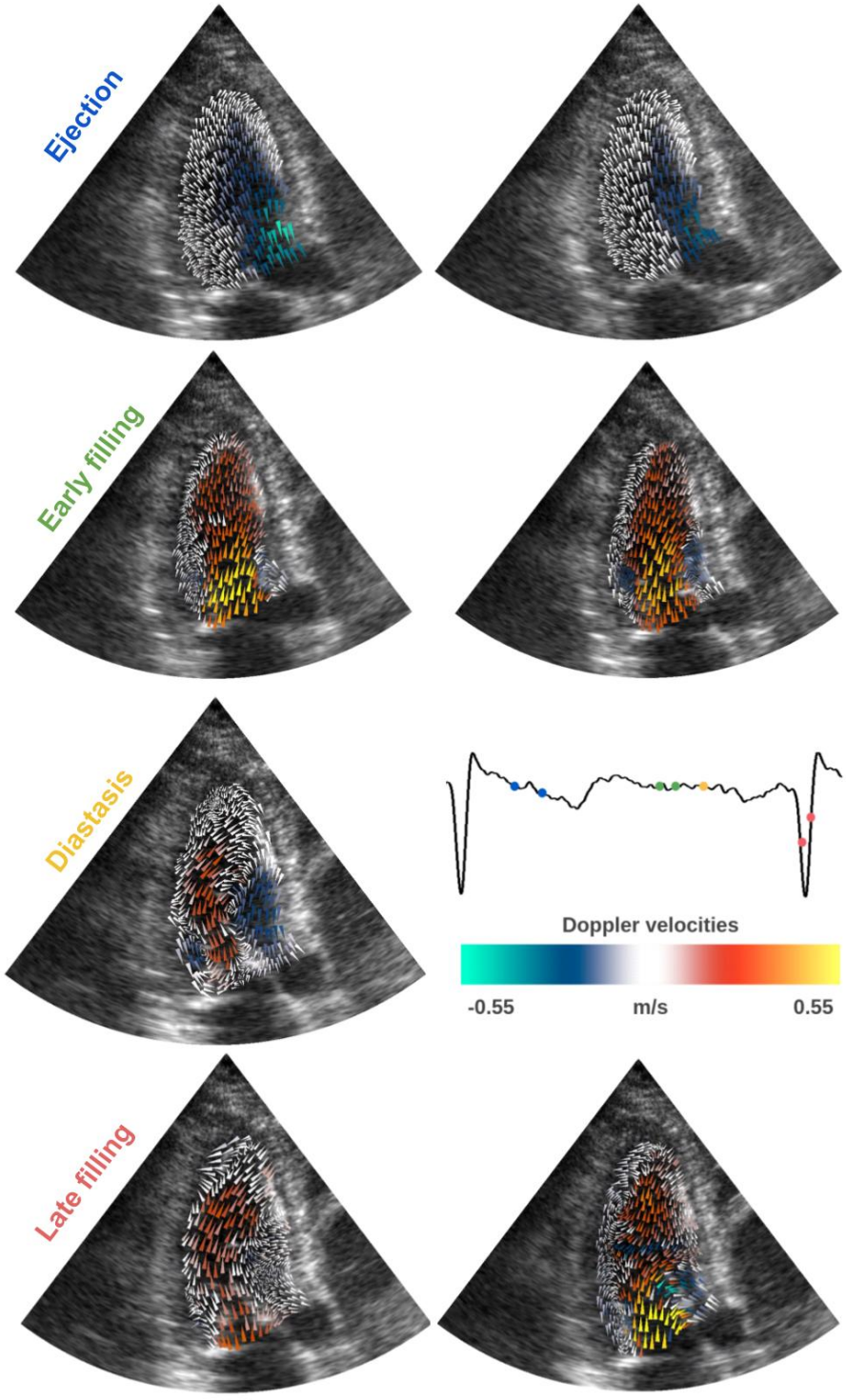

Figure 5.10: iVFM 2D Doppler velocities at the key instants shown on the ECG for virtual patient 3.

5.3.2 Scenario #2: additional synthetic clutter noise

Unlike the previous scenario, the scatterers belonging to the myocardium move coherently between each ultrasound firing, leading to more realistic situations. In this scenario, the signals returned by the myocardial tissue with high-amplitude and slow-motion interfere with the signals of blood flow, creating clutter noise. To this end, a polynomial clutter-filter [73] is applied on the synthetic I/Q signals after beamforming. The third column in Figure 5.11 shows the B-mode and Color Doppler images estimated from this scenario. The influence of the surrounding myocardial tissue is obvious during the filling phase, which is consistent with what can be obtained in the real acquisitions.

5.4 Discussions

1. Personalization procedure adapted to the simulation of large-scale dataset

   In the previous version of our simulation pipeline, we used a CFD model to compute a reference blood flow for each simulated sequence. The corresponding personalization procedure was based on a spatio-temporal registration which modified both the amplitudes and directions of the velocity field of the original CFD model. The mechanical properties of the flow were therefore not totally conserved. Moreover, there currently exists only one such CFD model simulated from a healthy volunteer, strongly limiting the variability of the blood vector fields registered on the different template sequences. To solve this major issue, we proposed a different scheme to simplify the personalization procedure of our pipeline while reinforcing the variability of the generated reference flows.

   Our approach is based on the computation of reference blood flow directly from the color Doppler images of the template sequences. The interest of this method is to compute realistic blood flow while preserving fluid dynamic properties. The effectiveness of our approach was illustrated through the simulation of a dataset composed of 20 virtual patients. The results we obtained confirmed the ability of our approach to generate blood vector fields with great variability while preserving a coherence of blood flow properties during the complete cardiac cycle.

2. Current limitations

   Figures 5.8 to 5.10 show the variety of intraventricular flows that we were able to generate. The good quality of the generated blood fields may come from the chosen clinical sequences. Indeed, all the patients involved in our dataset were chosen from their good quality, both in terms of B-mode visual aspects and color Doppler information. The application of the iVFM procedure on medium or poor image quality remains uncertain to obtain satisfying results.

3. Potential improvements

   The computation of the 2D vector field from the iVFM method required the same pre-processing steps, which currently involve manual tasks. We plan in the near

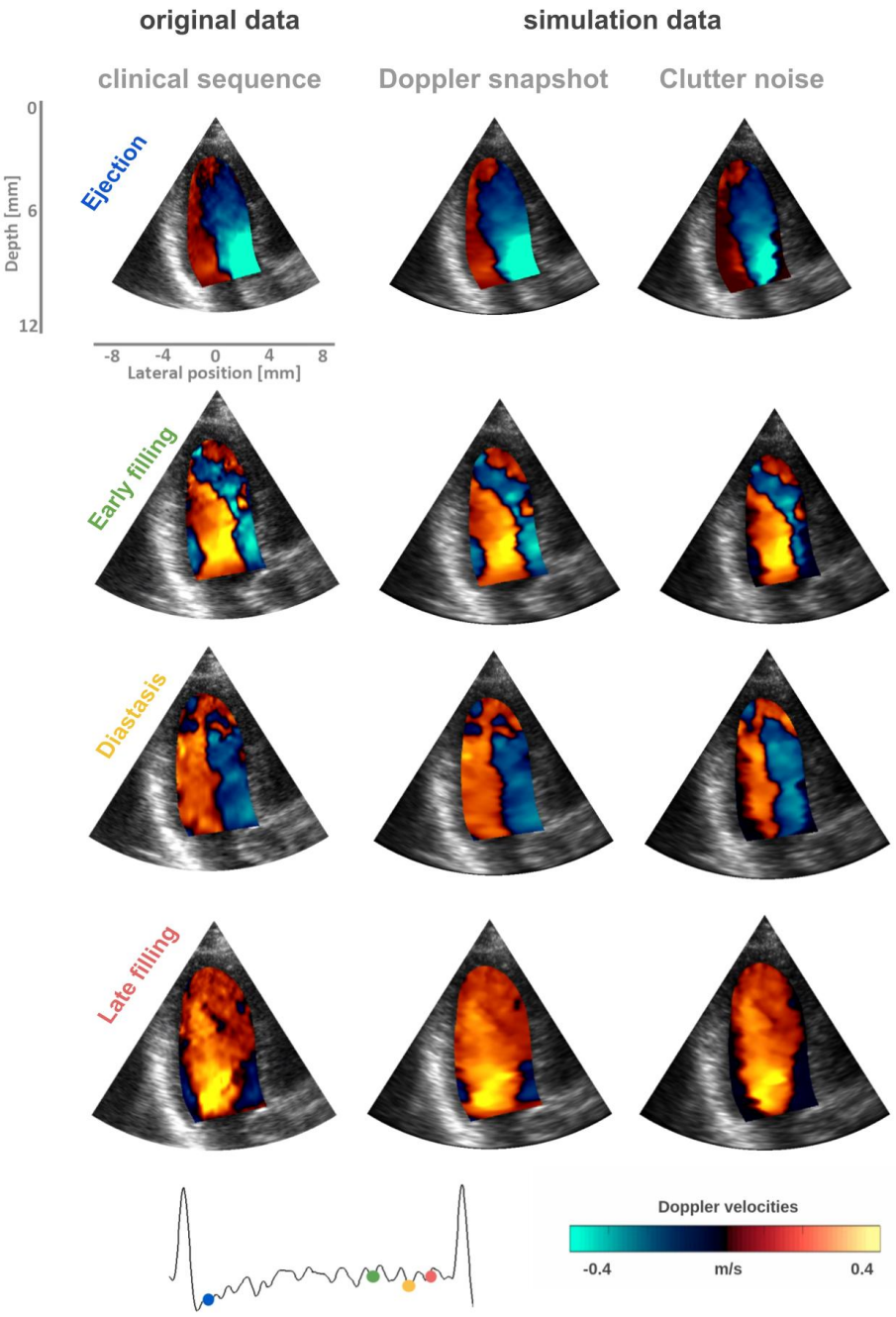

Figure 5.11: Illustration of the Duplex simulation pipeline of the color Doppler "snapshot" scenario and the clutter noise scenario. First column: Doppler velocity reference; Second column: Doppler velocity estimated from the simulated I/Q signals in the "snapshot" scenario; Third column: Doppler velocity estimated from the simulated I/Q signals in the clutter noise scenario.

future to make these steps fully automatic, with the help of deep learning methods, to reinforce the scalability of our simulation pipeline to simulate a large number of patients.

In the current version of the iVFM method, we use reconstructed 2D vector fields. To integrate out-of-plane motions into our simulation, we plan to work on a new version of the iVFM algorithm, which will be able to reconstruct 3D blood vector flows from tri-plane duplex ultrasound sequences [79].

5.5 Conclusion

The critical aspect for generating a large-scale dataset concerns the personalization procedure, *i.e.*, the adaptation of the model to a given patient. This is the current limitation of existing ultrasound simulation pipelines in echocardiography. To address this issue, we replaced the CFD model involved in our previous simulation framework with the velocity field obtained by the iVFM techniques computed from the color Doppler images of the template sequence. This method imposes fluid dynamics constraints, leading to realistic blood flow motion. The main weakness of our new strategy is that it requires some pre-processing steps, which can be time-consuming. We thus plan in the near future to automate these tasks (*i.e.*, automatic segmentation of the myocardium over the whole sequence and automatic de-aliasing of color Doppler images) to be able to apply a simulation pipeline on a large dataset. Meanwhile, we have simulated a dataset of 20 virtual patients to illustrate the feasibility of our approach. Results show the capacity of our pipeline to generate a wide range of reference blood flows with the corresponding realistic duplex sequences.

Chapter 6

Conclusion

Contents

6.1 Conclusions

Color Doppler imaging is a popular clinical modality for intraventricular flow visualization over a large area. This technique is subject to typical artifacts such as aliasing and clutter which make its interpretability more complex. In parallel, several approaches have shown the possibility of computing quantitative 2D flows from color Doppler images to provide useful information for diagnosing complex cardiac pathologies. Robustness of quantitative measurements from color Doppler images is therefore a current issue of great importance and deep learning approaches seem to be the solution of choice to solve this problem. The key aspect of these methods is the access to datasets with reference intraventricular flows. In this context, we proposed the following contributions:

1. We developed a novel simulation pipeline for the generation of realistic synthetic ultrasound duplex sequences, combining a state-of-the-art CFD model and a physical ultrasound simulator. Thanks to the genericity of our pipeline, different scenarios were simulated by playing with dynamic features such as the blood flow acceleration and the explicit motion of the surrounding tissues. We showed that our simulation pipeline can generate the classic aliasing and clutter artifacts from tissue motion;

2. A personalization procedure has been integrated into the simulation pipeline to improve the velocity of the different reference blood flow present in the dataset. To this aim, we replaced the CFD model with a strategy involving the iVFM method. In particular, this approach allows the computation of reference blood flow directly from patient data while maintaining fundamental fluids dynamics properties.

3. We built and provided the first synthetic dataset of ultrasound duplex sequences with the corresponding intraventricular reference vector fields. This dataset involved different scenarios that can be used to benchmark the quality of Doppler estimation techniques.

6.2 Potential improvements

Although we have already generated a synthetic dataset for 20 virtual patients with different scenarios, there are several opportunities for improvement:

1. The actual reference blood flow computed from the iVFM method is 2D, leading to a simplified simulated situation in terms of fluid dynamics. It would therefore be interesting to extend this method to the computation of 3D blood flows from dedicated ultrasound acquisitions. Moreover, the recent new version of SIMUS now integrates elevation focusing (which was not the case during most of my PhD). It is thus possible and very interesting to extend our simulation pipeline to take into account out-of-plane motions. Indeed, such a phenomenon is responsible for the increase of the variance of the Doppler estimate, and its integration will be of great value to our pipeline.

2. The actual version of our pipeline needs some manual operations like myocardial segmentation over the complete cardiac cycle and the localization of aliasing regions. It would be interesting to make these tasks fully automatic to reinforce the scalability of our simulation pipeline. Indeed, it would be very interesting to simulate in a fully automatic way duplex sequences from real recordings, without any human intervention. This will allow the creation of large-scale synthetic datasets that mimic hundreds/thousands of patients.

6.3 Clinical perspectives

The generation of a large-scale datasets for the training of deep learning methods will potentially bring the following innovations in clinical applications:

1. The improvement of blood flow visualization in clinical routine through the automatic removal of aliasing and clutter noise.

2. The direct estimation of the 2D blood velocity field from the I/Q signals. This will allow an easier interpretation of blood flow dynamics in the clinical routine. In addition, this can be used to characterize intraventricular flow properties such as the vortex that forms in the left heart and investigate the filling capacity of the heart.

Chapter 7

RÉSUMÉ en Français (French Summary)

Contents

Le travail présenté dans ce manuscrit concerne les simulations réalistes de séquences ultrasonores permettant la visualisation simultanée d'images anatomiques (B-Mode) et fonctionnelles (Doppler couleur). De telles séquences sont appelées séquences duplex. Ce premier chapitre est consacré à la reprise en français des aspects clés discutés dans le manuscrit complet rédigé en anglais. Les points suivants sont présentés :

1. Un résumé de ma thèse ;
2. Une section présentant le contexte et les objectifs de ma thèse ;
3. Un résumé de ma première contribution concernant la génération de séquences échocardiographiques duplex synthétiques réalistes ;
4. Un résumé de ma deuxième contribution sur la personnalisation de ma méthode pour la génération de bases de données synthétiques à grande échelle ;
5. La conclusion de ma thèse avec les perspectives associées.

7.1 Résumé

L'imagerie médicale joue un rôle primordial pour l'étude et le diagnostic des maladies cardiaques. Dans ce contexte, les mesures issues du flux intraventriculaire permettent d'estimer des indices cliniques pertinents pour établir un diagnostic. L'imagerie Doppler couleur est une modalité de choix pour la visualisation du flux intraventriculaire pour une zone étendue de l'image. Cependant, cette modalité permet uniquement la visualisation de la projection du flux le long de la direction de tirs ultrasonores et est sujet à des sources d'erreurs dont les principales sont l'aliasing (dû à des vitesses élevées du sang vis-à-vis du système d'acquisition) et le bruit de clutter (dû à de nombreuses sources dont les mouvements des tissues entourant la cavité ventriculaire). La réduction de ces artéfacts ainsi qu'une visualisation plus précise constituent donc des perspectives importantes en vue d'une meilleure analyse du flux intraventriculaire. Dans ce contexte, l'apprentissages profond (deep learning en anglais) constitue une voie prometteuse pour résoudre ces problèmes. En effet, cette technique a récemment été appliqué avec succès en imagerie ultrasonore pour des problèmes tels que la classification ou la segmentation. Les méthodes par apprentissage profond nécessitent la mise en place de bases de données annotées (c'est-à-dire avec des références) incluant plusieurs centaines voire milliers d'échantillons en imagerie médicale. Ceci constitue actuellement un frein pour l'application de telles techniques en imagerie de flux. Dans ce contexte, mes travaux de thèse consistent au développement d'un cadre méthodologique pour la simulation de séquences échocardiographiques duplex réalistes avec un champ de référence du flux intraventriculaire associée. La génération d'artéfacts synthétiques d'aliasing et de clutter est également un objectif de ma thèse. Cela permettra de générer des bases de données d'une grande variabilité permettant aux algorithmes d'apprentissage d'améliorer la qualité des séquences duplex. Nous avons en particulier simulé différents scénarios en jouant sur : *i)* l'accélération du flux, *ii)* le bruit de clutter dû au mouvement du muscle myocardique, *iii)* le type de transmission d'ondes ultrasonores.

A la fin de ma thèse, j'ai généré la première base de données de séquences échocardiographiques duplex réalistes pour 20 patients virtuels. Cette base de données est publique

et peut être utilisée pour l'évaluation de la qualité des techniques d'estimation Doppler. Dans un futur proche, il est prévu que la solution que j'ai développée soit rendu totalement automatique afin qu'elle puisse être utilisée pour la simulation de bases de données à grande échelle (>1000 patients) en vue d'alimenter des algorithmes d'apprentissage profond.

7.2 Introduction

Cette section présente d'abord le contexte autour de ma thèse, puis introduit la méthodologie proposée.

7.2.1 Contexte

7.2.1.1 Contexte clinique

Les maladies cardiovasculaires sont la principale cause de décès dans le monde, avec une mortalité de 17,9 millions de personnes par an [7]. L'estimation et l'analyse du flux intraventriculaire apportent des informations précieuses sur les propriétés fonctionnelles du cœur et constituent une aide précieuse quant à l'établissement d'un diagnostic. Dans ce contexte, l'imagerie Doppler couleur est une modalité de choix en routine clinique pour la visualisation du flux sanguin dans l'ensemble de la cavité ventriculaire. Malheureusement, cette imagerie n'est pas suffisamment précise pour effectuer des mesures quantitatives et d'autres techniques telles que le Doppler pulsé ou le Doppler continu sont préférées. Cependant, l'ensemble de ces techniques reposent sur l'estimation d'une projection 1D de la vitesse réelle le long des directions des tirs ultrasonores, ce qui limite la pertinence des informations extraites.

7.2.1.2 Contexte méthodologique

Plusieurs méthodes ont été proposées pour estimer le mouvement du flux intraventriculaire 2D ou 3D en utilisant des acquisitions échographiques [9, 10, 80]. La plupart de ces méthodes nécessite l'intervention d'un expert (*e.x.* segmentation des cavités cardiaques) ou une supervision d'un expert (*e.x.* qualité de suppression de l'aliasing ou du bruit de clutter), ce qui limite leur applicabilité en routines cliniques.

Récemment, les méthodes par apprentissage profond ont révolutionnées plusieurs applications en imagerie échocardiographiques, parmi lesquels nous pouvons citer la classification (*e.x.* reconnaissance automatique de vues [13]) et la segmentation (*e.x.* extraction automatique de la paroi du ventricule gauche pour l'estimation de la fraction d'éjection [14]). Les méthodes d'apprentissage profond de type supervisée sont les techniques qui produisent les meilleurs résultats à l'heure actuelle. Ces méthodes sont basées sur l'exploitation d'une base de données référencées, c'est à dire avec des annotations de référence généralement produites par un expert. Pour le moment, très peu de méthodes d'apprentissage supervisé ont été appliqué à l'amélioration de l'estimation du flux intraventriculaire. L'une des raisons est probablement la difficulté d'accéder à des bases de données dont les flux intraventriculaires sont connus et qui peuvent être utilisées en tant que référence pour les algorithmes d'apprentissage.

Dans ce contexte, les outils de simulations de séquences d'images échocardiographiques réalistes peuvent jouer un rôle clé. En effet, de tels outils permettraient de générer des bases de données de référence à grande échelle et donc d'étudier le potentiel des méthodes par apprentissage pour résoudre les différents problèmes énoncés ci-dessus. En particulier, la capacité des pipelines de simulations à reproduire des artéfacts tels que l'aliasing ou le bruit de clutter sera clé pour rendre les solutions par apprentissage robustes vis à vis des méthodes de l'état de l'art.

7.2.2 Objectifs et innovations ciblées

Les objectifs et innovations principaux de ma thèse sont les suivants :

1. Développement d'un pipeline de simulation de séquences échocardiographiques duplex pour la génération d'une base de données synthétique avec des flux intraventriculaires de référence. La base de données devra être réaliste à la fois quant à la texture des images B-mode générées et vis à vis des vitesses du flux intraventriculaire simulées. La base de données sera également rendue publique afin de permettre à la communauté d'évaluer des algorithmes d'estimation des vitesses Doppler.

2. Intégration d'artéfacts synthétiques réalistes tels que le bruit de clutter ou l'aliasing. Ceci permettra de rendre les simulations encore plus réalistes et pertinentes pour des algorithmes d'apprentissage.

3. Personnalisation du pipeline de simulation. Dans le but de générer une base de données à grande échelle, il est nécessaire de personnaliser le pipeline de simulation que j'ai développé, c'est à dire d'adapter la chaine de traitement à des séquences échocardiographiques réelles. Pour ce faire, il est nécessaire de générer des champs de vitesses du flux intraventriculaire de référence adaptés pour chaque patient traité.

7.2.3 Organisation de la thèse

Mon manuscrit de thèse est organisé de la façon suivante :

1. Présentation

    - Chapitre 7: Résumé de la thèse en français comme demandé par l'école doctorale EEA. Ce résumé aborde les points importants de ma thèse, en mettant l'accent sur mes principales contributions.
    - Chapitre 1 : Introduction du contexte de la thèse et des principales innovations ciblées.

2. Contexte

    - Chapitre 2 : Description dédiée du contexte de ma thèse. Les aspects suivants sont développés: la physiologie du cœur, les modalités utilisées en routine clinique et les principes physiques de l'échographie.
    - Chapitre 3 : Revue des méthodes de l'état de l'art en estimation du flux intraventriculaire ainsi que des méthodes de simulations de séquences d'images échocardiographiques.

3. Contributions

    - Chapitre 4 : Description détaillée du pipeline de simulation de séquences échocardiographiques duplex développé. Je décris les différents scénarios que j'ai simulé et je présente les résultats que j'ai obtenus.

- Chapitre 5 : Extension du pipeline pour simuler des bases de données à grande échelle. Je présente la méthode de personnalisation que j'ai mis en place afin de pouvoir appliquer directement ma méthode à des données patients acquises en routine clinique.

4. Conclusions

   - Chapitre 6 : Conclusion de ma thèse. Je présente les principales innovations développées au cours de ma thèse ainsi que les perspectives associées.

7.3 Contribution 1 : Développement d'un pipeline de simulation de séquences échocardiographiques duplex

7.3.1 Motivations

L'objectif de ma première contribution est de développer un pipeline de simulation de séquences échocardiographiques duplex réalistes dans le but de générer des bases de données à grande échelle.

7.3.2 Méthodologie

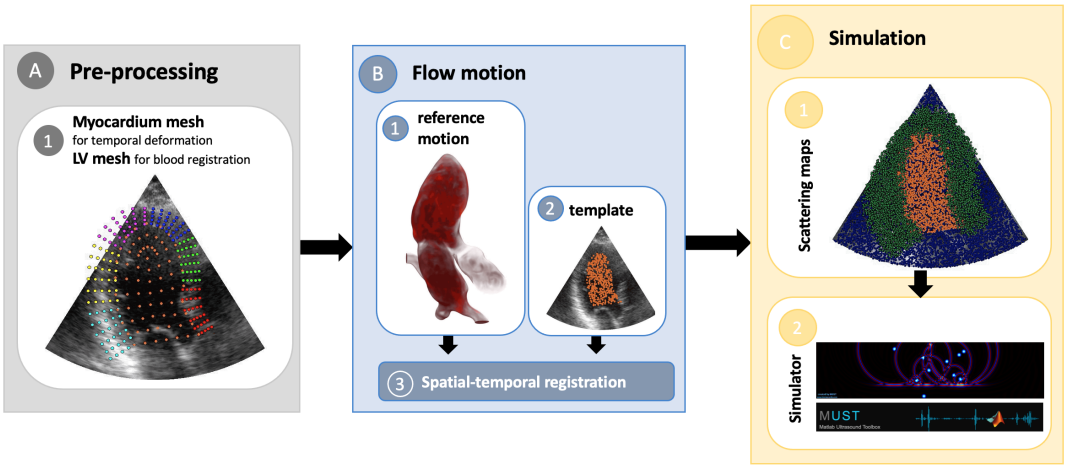

Figure 7.1: Pipeline proposé pour la simulation de séquences échocardiographiques duplex réalistes. (A) Une séquence réelle acquise en routine clinique sert de modèle pour synthétiser des textures ultrasonores, définir des anatomies réalistes et estimer le mouvement du myocarde ; (B) Un modèle CFD contrôle le mouvement synthétique du flux sanguin ; (C) Un environnement de simulation échographique fusionnant les informations issues de la séquence réelle et du modèle CFD permet de reproduire le processus de formation de l'image. Dans la séquence simulée, le flux sanguin est entièrement contrôlé par le modèle CFD et l'aspect visuel est très similaire à celui de l'acquisition réelle.

Figure 7.1 présente le diagramme général de la méthode que j'ai développé. Une acquisition réelle en vue apicale trois chambres est tout d'abord utilisée afin de simuler des textures ultrasonores réalistes. Dans un deuxième temps, la même séquence réelle est segmentée afin d'extraire deux régions d'intérêt (ROI) : le ventricule gauche et le myocarde. A partir des masques de segmentation associés, des séquences de maillages de ces 2 ROIs sont générées de façon automatique (bloc A). Un flux intraventriculaire issu d'un modèle de dynamique de fluide (CFD) est alors recalé sur la séquence réelle à partir des maillages du ventricule gauche associés. Cette étape permet de générer un mouvement de référence du flux intraventriculaire sur la séquence réelle traitée (bloc B). Ce

mouvement est alors utilisé afin de déplacer des diffuseurs ponctuels représentant le sang à l'intérieur du ventricule gauche d'une image simulée à une autre. La séquence de maillages du myocarde est utilisée afin de déplacer des diffuseurs représentant le myocarde. Cela permet à la fois de simuler des images B-mode de texture et de mouvements réalistes et d'introduire un bruit de clutter synthétique lors de l'estimation des vitesses Doppler. Un simulateur ultrasonore en libre accès (SIMUS) est finalement utilisé afin de générer des signaux ultrasonores synthétiques à partir de cartes de diffuseurs (bloc C). Ces signaux sont ensuite post-traités à l'aide d'algorithmes standards de formation de voies et d'estimation des vitesses Doppler afin de générer des séquences échocardiographiques Duplex réalistes.

7.3.3 Résultats

Le pipeline développé est suffisamment général pour pouvoir simuler les différents types de scénarios présentés ci-dessous:

- Scenario #1: images Doppler couleur «instantanées»
  Ce scénario suppose que l'on puisse obtenir une image Doppler couleur instantanée *1)* en l'absence de mouvement du myocarde et *2)* en supposant que le flux est stationnaire (aucune accélération temporelle) pendant les différentes émissions ultrasonores. Cela permet d'éviter l'introduction d'un bruit de clutter dû au mouvement des tissus ayant de forte intensité et limite la présence d'un biais causé par l'accélération du sang lors de l'estimation des vitesses Doppler. Dans ce scénario, les vitesses Doppler estimées doivent donc correspondre aux composantes de vitesse radiale du flux de référence basé sur le modèle de CFD.

- Scénario #2 : Écoulement non-stationnaire
  Dans ce scénario, le mouvement du sang n'est plus considéré comme stationnaire : les diffuseurs du sang sont déplacés suivant un mouvement de référence qui change entre deux émissions ultrasonores successives. Ce scénario prend donc en compte l'accélération du flux, ce qui produit des effets sur la qualité des estimations des vitesses Doppler.

- Scénario #3 : bruit de clutter additionnel
  Contrairement aux autres scénarios, le troisième scénario vise à simuler des situations au plus proche de celles rencontrées en routine clinique. Tous les diffuseurs du sang et des tissus environnant se déplacent entre deux émissions ultrasonores successives. Dans ce contexte, l'information portée par les mouvements lents des tissus est mélangée à celle du flux sanguin, produisant un bruit de paroi nommé bruit de clutter. Les signaux ultrasonores synthétiques ainsi générés doivent être prétraités par un filtre de clutter avant de pouvoir être utilisés pour l'estimation de vitesses Doppler. Pour ce faire, nous avons observé que la simple suppression de la composante continue des signaux bruts permettait d'effectuer une estimation précise des vitesses, ce qui correspond à un simple filtre polynomial d'ordre 0.

- Scénario #4 : différentes stratégies d'émission d'ondes ultrasonores
  Le but de ce scénario est d'étudier l'influence des modes d'émission des ondes ultrasonores sur la qualité des vitesses estimées. Chaque séquence a été simulé dans

les conditions décrites dans le scénario 1. De plus, les ondes émises pour la reconstruction des images B-mode sont des ondes focalisées alors que les ondes utilisées pour estimer les vitesses Doppler sont soit des ondes focalisées, soit des ondes divergentes.

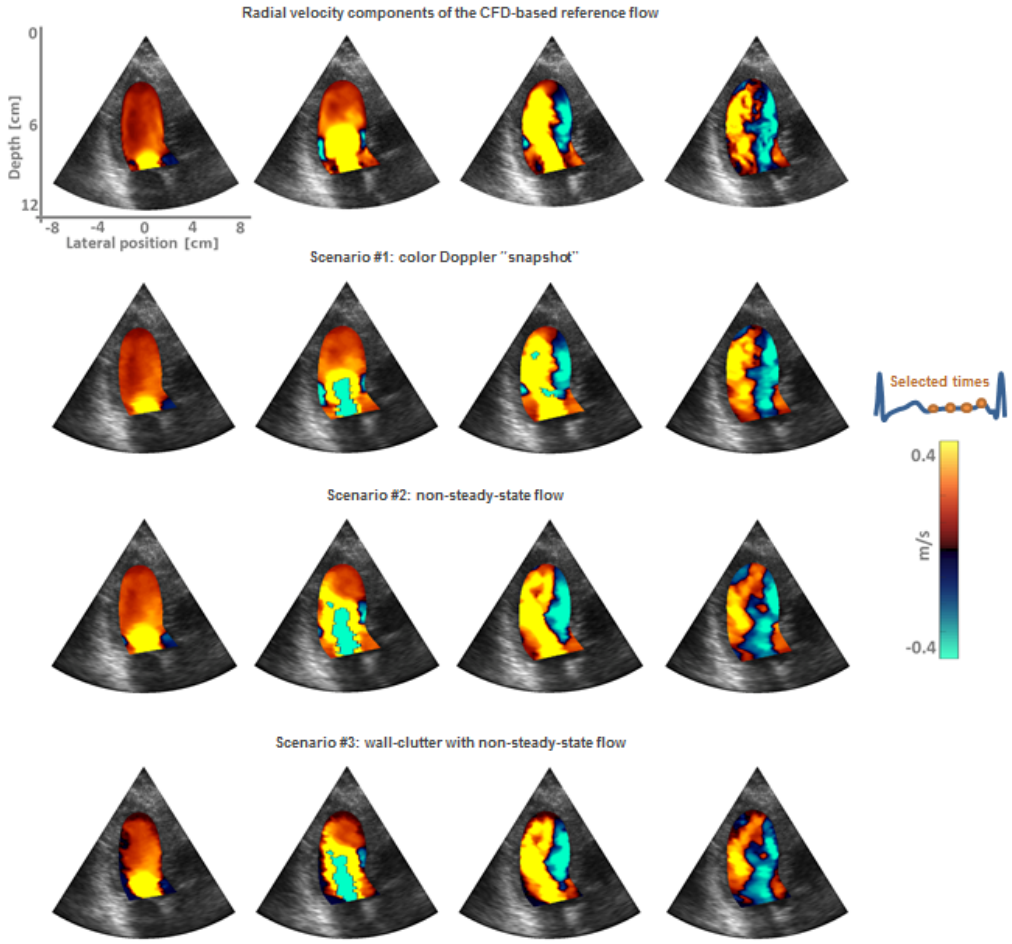

Figure 7.2: Illustration de la capacité de notre pipeline de simulation Doppler à générer les scénarios suivants : 1) une situation "instantanée" de Doppler couleur supposant un écoulement stationnaire et l'absence de mouvement du myocarde (deuxième ligne) ; 2) un écoulement non-stationnaire où les diffuseurs de sang sont déplacés entre deux émissions ultrasonores successives (troisième ligne) ; 3) Clutter dû au mouvement des parois avec un écoulement non-stationnaire où les diffuseurs du sang et des tissus sont déplacés entre deux émissions ultrasonores successifs (quatrième ligne).

La figure 7.2 présentent des exemples d'images simulées à partir des différents scénarios présentés ci-dessus.

7.3.4 Conclusion

Vis à vis de la littérature, les principales nouveautés introduites dans ce travail sont les suivantes :

- Nous avons développé le premier pipeline de simulation de séquences échocardiographiques duplex réalistes ;
- Nous avons intégré un modèle de CFD au sein de notre pipeline afin de générer un champ de vitesses du flux sanguin de référence ;
- Nous avons développé une stratégie permettant la simulation de bruit de clutter dû aux mouvements des tissus environnant ;
- Nous avons évalué la validité de notre pipeline au travers de différents scénarios permettant de simuler une grande diversité de situations, allant de cas simples à des cas plus réalistes.

7.4 Contribution 2 : Personnalisation du pipeline de simulation pour la génération de bases de données conséquentes

7.4.1 Motivations

Dans la section précédente, un modèle CFD du flux intraventriculaire issu de la littérature [68] a été intégré au sein du pipeline de simulation afin de générer un champ de vitesses de référence. Ce modèle contient des mouvements d'écoulement 3D complexes dans l'ensemble de la cavité. Malheureusement, il existe qu'un seul modèle de ce type simulé à partir d'un volontaire sain. Utiliser cet unique modèle pour simuler un grand nombre de patients virtuels ne permettra donc pas de générer une grande variété de mouvements, ce qui limite sont intérêt. Pour résoudre ce problème, nous proposons dans cette section de remplacer le modèle CFD par un algorithme d'estimation de flux intraventriculaire nommé iVFM. Ce modèle exploite une contrainte d'incompressibilité et permet de dériver un flux 2D sur l'ensemble de la cavité du ventricule gauche à partir d'une image Doppler couleur standard. Grâce à cet algorithme, nous rendons notre pipeline de simulation facilement personnalisable, c'est à dire adaptable à n'importe quelle séquence réelle afin de simuler son jumeau numérique. Cette modification est donc une étape clé pour la génération d'une base de données à grande échelle et riche en information de texture et de mouvements.

7.4.2 Méthodologie

Les étapes clés du pipeline restent les mêmes que celles décrites dans la section précédente. La principale différence concerne le calcul du mouvement de référence, ce qui entraine des modifications dans les étapes de pré-traitement et de recalage. En effet, les pré-traitements suivants sont nécessaires afin de pouvoir appliquer l'algorithme iVFM à partir d'images Doppler couleurs : *1)* segmentation de la paroi du ventricule gauche: *2)* calcul des vitesses de la paroi endocardique: *3)* suppression des artéfacts d'aliasing à l'intérieur de la cavité ventriculaire. Une fois ces étapes réalisées, la méthode iVFM permet d'estimer un champ de vitesse 2D dans l'ensemble de la cavité pour chaque séquence réelle traitée, ce qui permet de supprimer l'étape de recalage spatio-temporelle nécessaire dans la version précédente du pipeline. Ainsi, les diffuseurs présents dans la cavité ventriculaire sont déplacés via le champ de mouvement estimé par la méthode iVFM, alors que les diffuseurs présents dans le myocarde sont déplacés via la séquence de maillages myocardiques. Cette stratégie permet une personnalisation efficace de notre pipeline à partir des séquences réelles traitées. Ainsi, à partir d'une base de données réelles constituées de séquences échocardiographiques duplex, notre pipeline permet de simuler leurs jumeaux numériques de façon efficace, en garantissant des propriétés d'incompressibilité des flux de références générées ainsi qu'une adaptation aux conditions aux bords (positions et vitesses de la paroi ventriculaire).

La figure 7.3 illustre le flux sanguin intraventriculaire calculé à partir de l'algorithme iVFM aux instants clés affichés sur l'ECG. La couleur des flèches représente les informations Doppler couleur originales à partir desquels les champs iVFM ont été calculés. Les images de la première ligne correspondent aux instants qui suivent la fin de la diastole, lorsque le ventricule gauche commence à se contracter et provoque l'éjection du sang. En

raison du changement de pression dû à l'éjection, la valve mitrale s'ouvre et le sang commence à se remplir dans le ventricule gauche (deuxième ligne). Avant que l'oreillette ne se contracte, le vortex formé au début du remplissage est encore visible, comme le montre la troisième ligne. Lorsque l'oreillette se contracte, le remplissage est observé dans la quatrième ligne.

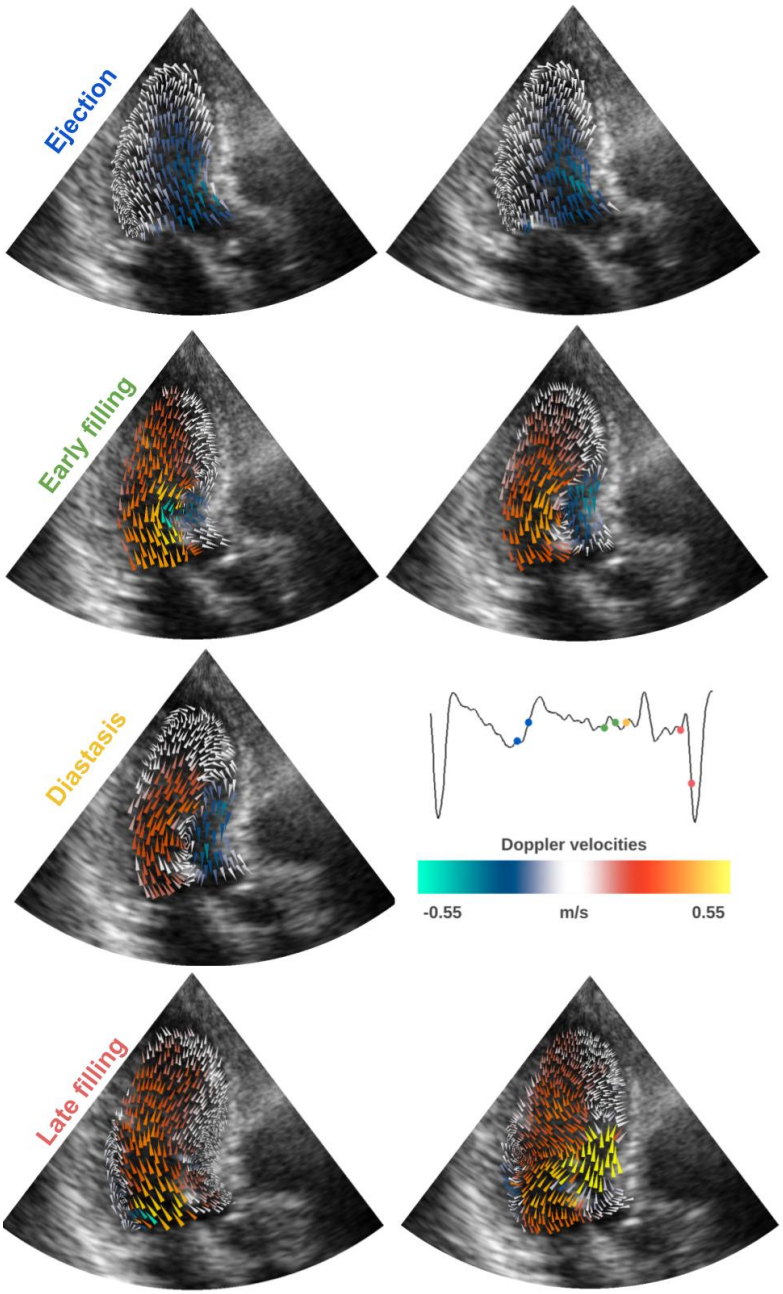

Figure 7.3: Flux intraventriculaire 2D estimé par la méthode iVFM à partir d'une séquence clinique réelle d'images Doppler.

7.4.3 Résultats

La nouvelle version de notre pipeline reste générique et permet toujours de simuler une grande diversité de scénarios tout en garantissant une grande variété des flux générés. Afin d'illustrer ces propriétés, nous avons générer une base de données comportant deux scénarios.

- Scenario #1: Images Doppler couleur «instantanées»
  Ce scénario correspond au scénario 1 de la section précédente. L'intérêt de ce scénario est de simuler des séquences échocardiographiques duplex de telle sorte que les vitesses Doppler estimées doivent correspondre aux composantes de vitesses radiales du flux de référence. Ainsi, ce scénario permet de vérifier la validité de la chaine de traitement mise en place.

- Scénario #2 : Bruit de clutter
  Contrairement au scénario précédent, nous avons rajouté un mouvement cohérent des diffuseurs appartenant au myocarde afin de rajouter un bruit de clutter comme dans le scénario 3 de la section précédente

7.4.4 Conclusion

L'un des aspects clés lors de la simulation d'une base de données à grande échelle concerne la capacité de personnalisation du pipeline utilisé, c'est à dire sa capacité d'adapter le flux de référence généré à différents patients. C'est une limite importante des pipelines actuelles de simulation de séquences d'images échocardiographiques. Pour résoudre ce problème, nous avons remplacé la stratégie de recalage d'un modèle CFD issu de l'état de l'art par l'estimation d'un flux de référence directement à partir de séquences réelles grâce à la méthode iVFM. L'intérêt de cette méthode est de garantir des propriétés d'incompressibilité du flux estimé. La principale faiblesse de notre nouvelle stratégie est qu'elle nécessite l'intervention d'experts pour différentes étapes de pré-traitements qui peuvent prendre du temps, comme la segmentation du ventricule gauche et du myocarde sur l'ensemble du cycle cardiaque. Nous envisageons donc dans un futur proche d'automatiser l'ensemble de ces tâches afin de pouvoir appliquer notre pipeline de simulation pour la génération de bases de données à grande échelle. En attendant, nous avons simulé une première base de données constituée de 20 patients numériques afin d'illustrer la faisabilité de notre approche. Les résultats obtenus confirment la capacité de notre pipeline de générer une grande diversité de flux intraventriculaires et de simuler les séquences échocardiographiques duplex associées.

7.5 Conclusion

Cette dernière section présente un résumé des contributions que j'ai réalisées au cours de ma thèse. J'aborde également des perspectives d'amélioration de mes travaux.

7.5.1 Contributions clés

Ma thèse a permis d'aboutir à trois contributions majeurs pour la communauté :

1. Nous avons développé un nouveau formalisme de simulation pour la génération de séquences échocardiographiques duplex réalistes. La solution retenue se base sur la combinaison d'un modèle CFD issue de la littérature afin de générer un flux analytique de référence et d'un simulateur physique des ultrasons. L'utilisation d'un simulateur physique permet de générer de façon intrinsèque des artéfacts d'aliasing. L'intégration explicite des mouvements des tissus environnants permet la génération de bruit de clutter. Grâce à la généricité du pipeline développé, différents scénarios ont été simulés en jouant sur l'accélération du flux sanguin ou la prise en compte des mouvements des tissus environnants ;

2. Une procédure de personnalisation a été intégrée dans notre pipeline de simulation afin d'améliorer la variabilité des flux intraventriculaires de référence de la base de données générée. Pour ce faire, nous avons remplacé le modèle CFD par un stratégie intégrant la méthode iVFM. Cette approche permet le calcul d'un flux de référence directement à partir des séquences réelles tout en conservant des propriétés fondamentales de dynamique des fluides (dans notre cas, la contrainte d'incompressibilité) ;

3. Nous avons construit et mis en accès libre la première base de données synthétiques de séquences échocardiographiques duplex avec un flux intraventriculaire de référence. Cette base de données est constituée de 20 patients et comprend différents scénarios qui peuvent être utilisés pour l'évaluation de la qualité des techniques d'estimation de vitesses Doppler.

7.5.2 Améliorations potentielles

Bien que nous ayons généré une première base de données de 20 patients virtuels, il existe plusieurs sources d'amélioration possible de notre pipeline afin de pouvoir simuler des bases de données à grande échelle :

1. Le flux intraventriculaire de référence généré par la méthode iVFM est actuellement 2D, ce qui conduit à une situation simplifiée en termes de dynamique de fluides. Il serait donc intéressant d'étendre cette méthode pour le calcul de flux en 3D à partir d'acquisitions échocardiographiques dédiées (une étude actuelle est en cours à partir de sondes triplans). De plus, la dernière version du logiciel SIMUS intègre désormais la notion de focalisation en élévation (ce qui n'était pas le cas pendant la majeure partie de mon doctorat). Il est donc possible et très intéressant d'étendre notre pipeline de simulation pour prendre en compte les mouvements hors plan. En effet, ce phénomène est responsable d'une augmentation de la variance d'estimation des

vitesses Doppler et son intégration rendra encore plus pertinentes les simulations réalisées ;

2. La version actuelle du pipeline nécessite l'intervention d'expert pour différents pré-traitements tels que la segmentation du ventricule gauche sur l'ensemble du cycle cardiaque à partir des images B-mode ou la suppression de l'aliasing sur les images Doppler couleur. Il apparait donc important de rendre ces différentes tâches entièrement automatiques afin de renforcer le côté évolutif de notre pipeline de simulation. En effet, il serait extrêmement intéressant de simuler de manière totalement automatique des séquences échocardiographiques duplex à partir de séquences réelles sans aucune intervention d'humain. Cela permettra de construire des bases de données synthétiques à grande échelle de jumeaux numériques de plusieurs centaines voire milliers de patients.

7.5.3 Perspectives cliniques

Le but visé de ma thèse est la constitution de bases de données à grande échelle présentant une forte richesse de mouvements du flux sanguin et de textures ultrasonores afin d'alimenter des méthodes par apprentissage profond. Les cibles d'innovations cliniques sont les suivantes :

1. Estimation robuste des images Doppler couleur sans artéfact d'aliasing ni de bruit de clutter pour une meilleure visualisation du flux intraventriculaire;

2. Estimation du champ de mouvement 2D du flux intraventriculaire directe à partir des signaux bruts ultrasonores. Cela permettra à terme une interprétation plus simple de la dynamique du flux sanguin au cours du cycle cardiaque. L'extraction robuste de mouvements 2D pourra être également utilisé afin de caractériser des propriétés de l'écoulement intraventriculaire, tel que la formation de vortex dans le ventricule gauche lors de la phase de remplissage.

Bibliography

[1] Wapcaplet, "Diagram of the human heart," jun 2006, [Online.] Availeble: https://commons.wikimedia.org/wiki/File:Diagram_of_the_human_heart_(cropped).svg.

[2] Wikipedia, "Wiggers diagram of a cardiac cycle," Jul 2016, [Online]. Available:https://en.wikipedia.org/wiki/Wiggers_diagram.

[3] C. J. Gallagher and G. Paparcuri, "Artifacts and pitfalls," [Online.] Available: https://thoracickey.com/artifacts-and-pitfalls/.

[4] D. GARCIA, "motion estimation," September 2021, [Online]. Available: https://www.biomecardio.com/files/IUS_course_motion_estimation_DG21.pdf.

[5] F. Vixège, A. Berod, Y. Sun, S. Mendez, O. Bernard, N. Ducros, P.-Y. Courand, F. Nicoud, and D. Garcia, "Physics-constrained intraventricular vector flow mapping by color doppler," *Physics in Medicine Biology*, 2021.

[6] S. Muth, S. Dort, I. A. Sebag, M.-J. Blais, and D. Garcia, "Unsupervised dealiasing and denoising of color-doppler data," *Medical Image Analysis*, vol. 15, pp. 577–588, 8 2011. [Online]. Available: https://linkinghub.elsevier.com/retrieve/pii/S1361841511000454

[7] WHO, "cardiovascular diseases," World Health Organization, [Online]. Available: https://www.who.int/health-topics/cardiovascular-diseases.

[8] P. N. Burns, "The physical principles of doppler and spectral analysis," *Journal of Clinical Ultrasound*, vol. 15, pp. 567–590, 11 1987. [Online]. Available: https://onlinelibrary.wiley.com/doi/10.1002/jcu.1870150903

[9] D. Garcia, J. C. del Álamo, D. Tanné, R. Yotti, C. Cortina, Bertrand, J. C. Antoranz, E. Pérez-David, R. Rieu, F. Fernández-Avilés, and J. Bermejo, "Two-dimensional intraventricular flow mapping by digital processing conventional color-doppler echocardiography images," *IEEE Transactions on Medical Imaging*, vol. 29, pp. 1701–1713, 10 2010. [Online]. Available: http://ieeexplore.ieee.org/document/5487393/

[10] K. C. Assi, E. Gay, C. Chnafa, S. Mendez, F. Nicoud, J. F. Abascal, P. Lantelme, F. Tournoux, and D. Garcia, "Intraventricular vector flow mapping - a doppler-based regularized problem with automatic model selection," *Physics in Medicine and Biology*, vol. 62, pp. 7131–7147, 2017.

[11] A. Gomez, K. Pushparajah, J. M. Simpson, D. Giese, T. Schaeffter, and G. Penney, "A sensitivity analysis on 3d velocity reconstruction from multiple registered echo doppler views," *Medical Image Analysis*, vol. 17, pp. 616–631, 8 2013. [Online]. Available: https://linkinghub.elsevier.com/retrieve/pii/S1361841513000467

[12] A. Gómez, A. de Vecchi, K. Pushparajah, J. Simpson, D. Giese, T. Schaeffter, and G. Penney, "3d intraventricular flow mapping from colour doppler images and wall motion," pp. 476–483, 2013. [Online]. Available: http://link.springer.com/10.1007/978-3-642-40763-5_59

[13] A. Madani, R. Arnaout, M. Mofrad, and R. Arnaout, "Fast and accurate view classification of echocardiograms using deep learning," *npj Digital Medicine*, vol. 1, p. 6, 12 2018. [Online]. Available: http://www.nature.com/articles/s41746-017-0013-1

[14] S. Leclerc, E. Smistad, J. Pedrosa, A. Ostvik, F. Cervenansky, F. Espinosa, T. Espeland, E. A. R. Berg, P. M. Jodoin, T. Grenier, C. Lartizien, J. Dhooge, L. Lovstakken, and O. Bernard, "Deep learning for segmentation using an open large-scale dataset in 2d echocardiography," *IEEE transactions on medical imaging*, vol. 38, pp. 2198–2210, 2019.

[15] B. H. D. Gerard J Tortora, *Introduction to the human body.*, 2017.

[16] P. P. Sengupta, G. Pedrizzetti, P. J. Kilner, A. Kheradvar, T. Ebbers, G. Tonti, A. G. Fraser, and J. Narula, "Emerging trends in cv flow visualization," *JACC: Cardiovascular Imaging*, vol. 5, pp. 305–316, 3 2012. [Online]. Available: https://linkinghub.elsevier.com/retrieve/pii/S1936878X12000125

[17] D. R. Muñoz, M. Markl, J. L. M. Mur, A. Barker, C. Fernández-Golfín, P. Lancellotti, and J. L. Z. Gómez, "Intracardiac flow visualization: Current status and future directions," *European Heart Journal Cardiovascular Imaging*, vol. 14, pp. 1029–1038, 2013.

[18] J. M. B. Jerrold T Bushberg, *The essential physics of medical imaging*, 2011, vol. 10.

[19] K. K. Shung, "Diagnostic ultrasound: Past, present, and future," *Journal of Medical and Biological Engineering*, vol. 31, 2011.

[20] J. G. Abbott and F. L. Thurstone, "Acoustic speckle: Theory and experimental analysis," *Ultrasonic Imaging*, vol. 1, pp. 303–324, 10 1979. [Online]. Available: http://journals.sagepub.com/doi/10.1177/016173467900100402

[21] A. Ng and J. Swanevelder, "Resolution in ultrasound imaging," *Continuing Education in Anaesthesia Critical Care Pain*, vol. 11, pp. 186–192, 10 2011. [Online]. Available: https://linkinghub.elsevier.com/retrieve/pii/S1743181617302068

[22] L. W. Schmerr, "Fundamentals of ultrasonic phased arrays," *Solid Mechanics and its Applications*, vol. 215, 2015.

[23] M. Halliwell, "Doppler ultrasound: Physics, instrumentation and signal processing (second edition)," *Physiological Measurement*, vol. 21, pp. 425–426, 6 2000. [Online]. Available: https://iopscience.iop.org/article/10.1088/0967-3334/21/3/702

[24] L. W. Schmmer, "Fundamentals of ultrasonic phased arrays," *Modern Physics Letters B*, vol. 22, 2008.

[25] J. Au, R. Hughson, and A. Yu, "Riding the plane wave: Considerations for in vivo study designs employing high frame rate ultrasound," *Applied Sciences*, vol. 8, p. 286, 2 2018. [Online]. Available: http://www.mdpi.com/2076-3417/8/2/286

[26] M. Cikes, L. Tong, G. R. Sutherland, and J. D'hooge, "Ultrafast cardiac ultrasound imaging," *JACC: Cardiovascular Imaging*, vol. 7, pp. 812–823, 8 2014. [Online]. Available: https://linkinghub.elsevier.com/retrieve/pii/S1936878X14004410

[27] L. Demi, "Practical guide to ultrasound beam forming: Beam pattern and image reconstruction analysis," *Applied Sciences*, vol. 8, p. 1544, 9 2018. [Online]. Available: http://www.mdpi.com/2076-3417/8/9/1544

[28] H. Hasegawa and H. Kanai, "High-frame-rate echocardiography using diverging transmit beams and parallel receive beamforming," *Journal of Medical Ultrasonics*, vol. 38, pp. 129–140, 7 2011. [Online]. Available: http://link.springer.com/10.1007/s10396-011-0304-0

[29] J. Porée, D. Posada, A. Hodzic, F. Tournoux, G. Cloutier, and D. Garcia, "High-frame-rate echocardiography using coherent compounding with doppler-based motion-compensation," *IEEE Transactions on Medical Imaging*, vol. 35, no. 7, pp. 1647–1657, 2016.

[30] G. Montaldo, M. Tanter, J. Bercoff, N. Benech, and M. Fink, "Coherent plane-wave compounding for very high frame rate ultrasonography and transient elastography," *IEEE Transactions on Ultrasonics, Ferroelectrics, and Frequency Control*, vol. 56, 2009.

[31] Z. Rami and S. Alomari, "Plane wave imaging beamforming techniques for medical ultrasound imaging," 2017.

[32] J. Kirkhorn, "Introduction to iq-demodulation of rf-data," *Ifbt, Ntnu*, 1999.

[33] Öz Yilmaz, *Seismic Data Analysis*. Society of Exploration Geophysicists, 1 2001, vol. 10. [Online]. Available: https://library.seg.org/doi/book/10.1190/1.9781560801580

[34] K. Mayer, R. Marklein, K. Langenberg, and T. Kreutter, "Three-dimensional imaging system based on fourier transform synthetic aperture focusing technique," *Ultrasonics*, vol. 28, pp. 241–255, 7 1990. [Online]. Available: https://linkinghub.elsevier.com/retrieve/pii/0041624X90900912

[35] A. C. Luchies and B. C. Byram, "Deep neural networks for ultrasound beamforming," *IEEE Transactions on Medical Imaging*, vol. 37, pp. 2010–2021, 9 2018. [Online]. Available: https://ieeexplore.ieee.org/document/8302520/

[36] J. Bercoff, G. Montaldo, T. Loupas, D. Savery, F. Mézière, M. Fink, and M. Tanter, "Ultrafast compound doppler imaging: providing full blood flow characterization,"

IEEE Transactions on Ultrasonics, Ferroelectrics and Frequency Control, vol. 58, pp. 134–147, 1 2011. [Online]. Available: http://ieeexplore.ieee.org/document/5688407/

[37] S. Bjaerum, H. Torp, and K. Kristoffersen, "Clutter filter design for ultrasound color flow imaging," *IEEE Transactions on Ultrasonics, Ferroelectrics and Frequency Control*, vol. 49, pp. 204–216, 2 2002. [Online]. Available: http://ieeexplore.ieee.org/document/985705/

[38] J. Willemetz, "Bias and variance in the estimate of the doppler frequency induced by a wall motion filter," *Ultrasonic Imaging*, vol. 11, pp. 215–225, 7 1989. [Online]. Available: https://linkinghub.elsevier.com/retrieve/pii/0161734689900758

[39] A. P. Hoeks, J. J. V. de Vorst, P. J. Brands, and R. S. Reneman, "An efficient algorithm to remove low frequency doppler signals in digital doppler systems," *Ultrasonic Imaging*, vol. 13, 1991.

[40] H. Torp, "Clutter rejection filters in color flow imaging: a theoretical approach," *IEEE Transactions on Ultrasonics, Ferroelectrics and Frequency Control*, vol. 44, pp. 417–424, 3 1997. [Online]. Available: http://ieeexplore.ieee.org/document/585126/

[41] C. Kasai, K. Namekawa, A. Koyano, and R. Omoto, "Real-time two-dimensional blood flow imaging using an autocorrelation technique," *IEEE Transactions on Sonics and Ultrasonics*, vol. 32, pp. 458–464, 5 1985. [Online]. Available: http://ieeexplore.ieee.org/document/1539691/

[42] T. Loupas, J. Powers, and R. Gill, "An axial velocity estimator for ultrasound blood flow imaging, based on a full evaluation of the doppler equation by means of a two-dimensional autocorrelation approach," *IEEE Transactions on Ultrasonics, Ferroelectrics and Frequency Control*, vol. 42, pp. 672–688, 7 1995. [Online]. Available: http://ieeexplore.ieee.org/document/393110/

[43] T. Kukulski, J. U. Voigt, U. M. Wilkenshoff, J. M. Strotmann, B. Wranne, L. Hatle, and G. R. Sutherland, "A comparison of regional myocardial velocity information derived by pulsed and color doppler techniques: An in vitro and in vivo study," *Echocardiography*, vol. 17, pp. 639–651, 10 2000. [Online]. Available: http://doi.wiley.com/10.1046/j.1540-8175.2000.00639.x

[44] D. Garcia, "Simus: an open-source simulator for ultrasound imaging. part i: theory & examples," *arXiv preprint. arXiv:2102.02738*, 2021.

[45] C. Amanda, V. François, and G. Damien, "Simus: an open-source simulator for ultrasound imaging. part ii: comparison with three popular simulators," *arXiv preprint. arXiv:2103.05521*, 2021.

[46] J. A. Jensen, "Field: A program for simulating ultrasound systems," *Medical and Biological Engineering and Computing*, vol. 34, 1996.

[47] J. Jensen and N. Svendsen, "Calculation of pressure fields from arbitrarily shaped, apodized, and excited ultrasound transducers," *IEEE Transactions on Ultrasonics, Ferroelectrics and Frequency Control*, vol. 39, pp. 262–267, 3 1992. [Online]. Available: http://ieeexplore.ieee.org/document/139123/

[48] B. E. Treeby and B. T. Cox, "k-wave: Matlab toolbox for the simulation and reconstruction of photoacoustic wave fields," *Journal of Biomedical Optics*, vol. 15, p. 021314, 2010. [Online]. Available: http://www.k-wave.org/papers/2010-Treeby-JBO.pdf

[49] B. E. Treeby, J. Jaros, A. P. Rendell, and B. T. Cox, "Modeling nonlinear ultrasound propagation in heterogeneous media with power law absorption using a k-space pseudospectral method," *The Journal of the Acoustical Society of America*, vol. 131, pp. 4324–4336, 6 2012. [Online]. Available: http://asa.scitation.org/doi/10.1121/1.4712021

[50] M. Alessandrini, M. D. Craene, O. Bernard, S. Giffard-Roisin, P. Allain, I. Waechter-Stehle, J. Weese, E. Saloux, H. Delingette, M. Sermesant, and J. D'hooge, "A pipeline for the generation of realistic 3d synthetic echocardiographic sequences: Methodology and open-access database," *IEEE Transactions on Medical Imaging*, vol. 34, pp. 1436–1451, 7 2015. [Online]. Available: https://ieeexplore.ieee.org/document/7024160/

[51] M. Alessandrini, B. Chakraborty, B. Heyde, O. Bernard, M. De Craene, M. Sermesant, and J. D'Hooge, "Realistic vendor-specific synthetic ultrasound data for quality assurance of 2-d speckle tracking echocardiography: Simulation pipeline and open access database," *IEEE Transactions on Ultrasonics, Ferroelectrics, and Frequency Control*, vol. 65, no. 3, pp. 411–422, 2018.

[52] H. Gao, P. Claus, G. H. van Lenthe, S. Jaecques, S. Boonen, G. V. der Perre, W. Lauriks, and J. D'hooge, "A convolution-based methodology to simulate cardiac ultrasound data sets: Integration of realistic beam profiles," pp. 2520–2523, 2009. [Online]. Available: http://link.springer.com/10.1007/978-3-540-89208-3_604

[53] P. Pibarot, D. Garcia, and J. G. Dumesnil, "Energy loss index in aortic stenosis," *Circulation*, vol. 127, no. 10, pp. 1101–1104, 2013.

[54] M. A. Pozniak, J. A. Zagzebski, and K. A. Scanlan, "Spectral and color doppler artifacts." *RadioGraphics*, vol. 12, no. 1, pp. 35–44, 1992.

[55] L. Terslev, A. P. Diamantopoulos, U. M. Døhn, W. A. Schmidt, and S. Torp-Pedersen, "Settings and artefacts relevant for doppler ultrasound in large vessel vasculitis," *Arthritis Research & Therapy*, vol. 19, no. 1, p. 167, Jul 2017.

[56] A. Shahin, M. Ménard, and M. Eboueya, "Cooperation of fuzzy segmentation operators for correction aliasing phenomenon in 3d color doppler imaging," *Artificial Intelligence in Medicine*, vol. 19, no. 2, pp. 121 – 154, 2000, medical Imaging.

[57] A. C. Yu and L. Lovstakken, "Eigen-based clutter filter design for ultrasound color flow imaging: A review," *IEEE Transactions on Ultrasonics, Ferroelectrics, and Frequency Control*, vol. 57, 2010.

[58] S. Fadnes, S. Bjærum, H. Torp, and L. Lovstakken, "Clutter filtering influence on blood velocity estimation using speckle tracking," *IEEE Transactions on Ultrasonics, Ferroelectrics, and Frequency Control*, vol. 62, no. 12, pp. 2079–2091, 2015.

[59] H. Nahas, J. S. Au, T. Ishii, B. Y. S. Yiu, A. J. Y. Chee, and A. C. H. Yu, "A deep learning approach to resolve aliasing artifacts in ultrasound color flow imaging," *IEEE Transactions on Ultrasonics, Ferroelectrics, and Frequency Control*, vol. 67, no. 12, pp. 2615–2628, 2020.

[60] O. Ronneberger, P. Fischer, and T. Brox, "U-net: Convolutional networks for biomedical image segmentation," vol. 9351, 2015.

[61] E. Evain, K. Faraz, T. Grenier, D. Garcia, M. De Craene, and O. Bernard, "A pilot study on convolutional neural networks for motion estimation from ultrasound images," *IEEE Transactions on Ultrasonics, Ferroelectrics, and Frequency Control*, vol. 67, no. 12, pp. 2565–2573, 2020.

[62] A. Prakosa, M. Sermesant, H. Delingette, S. Marchesseau, E. Saloux, P. Allain, N. Villain, and N. Ayache, "Generation of synthetic but visually realistic time series of cardiac images combining a biophysical model and clinical images," *IEEE Transactions on Medical Imaging*, vol. 32, no. 1, pp. 99–109, 2013.

[63] M. De Craene, S. Marchesseau, B. Heyde, H. Gao, M. Alessandrini, O. Bernard, G. Piella, A. R. Porras, L. Tautz, A. Hennemuth, A. Prakosa, H. Liebgott, O. Somphone, P. Allain, S. Makram Ebeid, H. Delingette, M. Sermesant, J. D'hooge, and E. Saloux, "3d strain assessment in ultrasound (straus): A synthetic comparison of five tracking methodologies," *IEEE Transactions on Medical Imaging*, vol. 32, no. 9, pp. 1632–1646, 2013.

[64] Y. Zhou, S. Giffard-Roisin, M. De Craene, S. Camarasu-Pop, J. D'Hooge, M. Alessandrini, D. Friboulet, M. Sermesant, and O. Bernard, "A framework for the generation of realistic synthetic cardiac ultrasound and magnetic resonance imaging sequences from the same virtual patients," *IEEE Transactions on Medical Imaging*, vol. 37, no. 3, pp. 741–754, 2018.

[65] M. Alessandrini, B. Chakraborty, B. Heyde, O. Bernard, M. De Craene, M. Sermesant, and J. D'Hooge, "Realistic vendor-specific synthetic ultrasound data for quality assurance of 2-d speckle tracking echocardiography: Simulation pipeline and open access database," *IEEE Transactions on Ultrasonics, Ferroelectrics, and Frequency Control*, vol. 65, no. 3, pp. 411–422, 2018.

[66] S. Marchesseau, H. Delingette, M. Sermesant, and N. Ayache, "Fast parameter calibration of a cardiac electromechanical model from medical images based on the unscented transform," *Biomechanics and Modeling in Mechanobiology*, vol. 12, no. 4, pp. 815–831, 2013.

[67] J. A. Jensen, "Field: A program for simulating ultrasound systems," in *10TH NORDICBALTIC CONFERENCE ON BIOMEDICAL IMAGING, VOL. 4, SUPPLEMENT 1, PART 1:351–353*, 1996, pp. 351–353.

[68] C. Chnafa, S. Mendez, and F. Nicoud, "Image-based large-eddy simulation in a realistic left heart," *Computers and Fluids*, vol. 94, pp. 173–187, 2014. [Online]. Available: https://hal.archives-ouvertes.fr/hal-00943609

[69] C. Chnafa, S. Mendez, R. Moreno, and F. Nicoud, *Using Image-based CFD to Investigate the Intracardiac Turbulence*. Cham: Springer International Publishing, 2015, pp. 97–117.

[70] C. Chnafa, S. Mendez, and F. Nicoud, "Image-based simulations show important flow fluctuations in a normal left ventricle: What could be the implications?" *Annals of Biomedical Engineering*, vol. 44, pp. 3346–3358, 11 2016. [Online]. Available: http://link.springer.com/10.1007/s10439-016-1614-6

[71] S. Shahriari and D. Garcia, "Meshfree simulations of ultrasound vector flow imaging using smoothed particle hydrodynamics," *Physics in Medicine Biology*, vol. 63, p. 205011, 10 2018. [Online]. Available: https://iopscience.iop.org/article/10.1088/1361-6560/aae3c3

[72] V. Perrot, M. Polichetti, F. Varray, and D. Garcia, "So you think you can das? a viewpoint on delay-and-sum beamforming," 7 2020. [Online]. Available: https://arxiv.org/abs/2007.11960

[73] C. Madiena, J. Faurie, J. Porée, and D. Garcia, "Color and vector flow imaging in parallel ultrasound with sub-nyquist sampling," *IEEE Transactions on Ultrasonics, Ferroelectrics, and Frequency Control*, vol. 65, no. 5, pp. 795–802, 2018.

[74] J. Faurie, M. Baudet, K. C. Assi, D. Auger, G. Gilbert, F. Tournoux, and D. Garcia, "Intracardiac vortex dynamics by high-frame-rate doppler vortography—*In Vivo* comparison with vector flow mapping and 4-d flow mri," *IEEE Transactions on Ultrasonics, Ferroelectrics, and Frequency Control*, vol. 64, no. 2, pp. 424–432, 2017.

[75] J. Faurie, M. Baudet, J. Porée, G. Cloutier, F. Tournoux, and D. Garcia, "Coupling myocardium and vortex dynamics in diverging-wave echocardiography," *IEEE Transactions on Ultrasonics, Ferroelectrics, and Frequency Control*, vol. 66, no. 3, pp. 425–432, 2019.

[76] A. Østvik, I. M. Salte, E. Smistad, T. M. Nguyen, D. Melichova, H. Brunvand, K. Haugaa, T. Edvardsen, B. Grenne, and L. Lovstakken, "Myocardial function imaging in echocardiography using deep learning," *IEEE Transactions on Medical Imaging*, vol. 40, no. 5, pp. 1340–1351, 2021.

[77] A. Nilsson, "Artefacts in sonography and doppler," *European Radiology*, vol. 11, no. 8, pp. 1308–1315, Aug. 2001.

[78] D. Garcia, "Robust smoothing of gridded data in one and higher dimensions with missing values," *Computational Statistics Data Analysis*, vol. 54, pp. 1167–1178, 4 2010. [Online]. Available: https://linkinghub.elsevier.com/retrieve/pii/S0167947309003491

[79] F. Vixège, P.-Y. Courand, F. Nicoud, and D. Garcia, "Full-volume three-component intraventricular vector flow mapping using triplane doppler echo," *arXiv preprint*, 2022.

[80] S. Dort, S. Muth, A. Swillens, P. Segers, G. Cloutier, and D. Garcia, "Vector flow mapping using plane wave ultrasound imaging." IEEE, 10 2012, pp. 330–333. [Online]. Available: http://ieeexplore.ieee.org/document/6562473/

FOLIO ADMINISTRATIF

THESE DE L'UNIVERSITE DE LYON OPEREE AU SEIN DE L'INSA LYON

NOM : SUN

DATE de SOUTENANCE : 24/01/2022

Prénoms : Yunyun

TITRE : Patient-based color Doppler echocardiographic simulation
Simulation d'images échocardiographiques Doppler couleur à partir de patients

NATURE : Doctorat

Numéro d'ordre : 2022LYSEI003

Ecole doctorale : EDA 160 : Electronique, Electrotechnique, Automatique (EEA)

Spécialité : Traitement du Signal et de l'Image

RESUME :

MOTS-CLÉS : Échocardiographie, simulation ultrason, flux intraventriculaire,Doppler couleur,pipeline de simulation, base de données, apprentissage supervisé, science ouverte.

Laboratoire (s) de recherche : CREATIS

Directeur de thèse: Olivier BERNARD et Damien GARCIA

Président de jury :

Composition du jury : Bernard Olivier, Bosch.G Johan, Franceschini Emilie, Friboulet Denis, Garcia Damien, Thiran Jean-Philippe